Sensitivity of Shear and Longitudinal Wave Velocities to Compression and Shear Stress Paths in Cohesive Soils

A thesis submitted by

George T. McAneny

in partial fulfillment of the requirements for the degree of

Master of Science

in

Civil and Environmental Engineering

Tufts University

August 2022

© 2022, George T. McAneny

Adviser: John Germaine

Sensitivity of Shear and Longitudinal Velocity to Compression and Shear Stress Paths in Cohesive Soils

by

George T. McAneny

Submitted to the Department of Civil and Environmental Engineering in partial fulfillment of the requirements for the degree of Master of Science in Civil and Environmental Engineering

I. Abstract

Clays, whether deposited on the seafloor or resedimented in the lab, generally exhibit a type of anisotropy called transverse isotropy (TI) due to layering and grain/void orientation from compaction. Sediments also experience an array of stress states due to varying geologic conditions. It is important to systematically measure how velocity anisotropy evolves with stress path to improve subsurface geophysical models, understand dynamic stress-strain relationships, and perform informed geotechnical site characterizations. This research experimentally measured velocity anisotropy in intact vs resedimented Boston Blue Clay (BBC), as well as stress path velocity dependence, vertical velocities during undrained shear, and velocity anisotropy from σ'_m of 1 to 10 MPa of resedimented Gulf of Mexico Eugene Island Clay (RGoM-EI). Results for intact versus resedimented BBC agree, and all clays exhibited low horizontal vs vertical velocity anisotropy and inclined compressional wave anisotropy (Thomsen parameters ε, γ, and $\delta \leq 0.3$). Shear stress ($\sigma_1 - \sigma_3$) was found to affect wave velocity immensely, and results suggest that stress path compression-derived equivalent velocity curves resemble Modified Cam Clay (MCC) iso-porosity ellipses. Undrained shear-derived iso-velocity curves agree with those from normal consolidation as well, implying that porosity/density controls vertical P-wave velocity (V_p) in normally consolidated clays.

This thesis also improves upon shear and longitudinal (V_s and V_p) wave velocity measurement technologies developed at Tufts Advanced Geotechnical Laboratory and MIT. Prior technology exhibited signal noise issues that affected horizontal wave velocity interpretation. Additionally, apparatus compressibility was not considered in the previous studies, leading to offset velocity measurements. The signal issue in the horizontal wave arrivals was found to be caused by improper grounding, originating from a shared ground pin of both receiving and sending actuators. Apparatus compressibility was then measured, and for a uniaxial test at 10 MPa axial effective stress (σ'_a), the velocity offset was found to be 13.7 m/s. Since the P-wave velocity range of interest is greater than 1500 m/s in sea water, this deviation produces a 2.5% error in vertical P-wave velocity (V_{pV}). This implies that all prior V_{pV} were overestimated by up to 2.5 percent, though this error is now corrected for in post-processing.

II. Acknowledgements

First and foremost, I would like to thank my advisor, Dr. John Germaine, for his kind and generous support throughout my research. He has always been there to offer encouragement when I needed it, advice when things didn't go as planned, and trusted in abilities I didn't know I possessed. His way of thinking about the world is a gift, and I feel extremely blessed to have gotten to learn from him during these past two years.

I also am forever indebted to the incredible Tufts faculty and staff who helped me along this journey. I'd like to thank Dr. Laurie Baise for taking the time to talk to me and introducing me to Dr. Germaine, Dr. Lucy Jen for introducing me to soil mechanics and geotechnical issues to keep an eye out for, Dr. Luis Dorfmann for kindly taking time outside of class to help me catch up on the theory behind FEM, Dr. Rob White for trusting me to use his AWG, Dr. Richard Plumb for kindly taking the time to teach me about geophysics, and Dr. Juan Pestana for making earthquake engineering approachable. I would also like to thank Mr. Scott MacCorkle for masterfully crafting my designs into reality, and for kindly answering my many questions in the machine shop. You all have expanded my view of the world, and I cannot thank you enough for this.

I would like to thank my friends and colleagues as well. C. Emre Uyeturk, for his wisdom, patience walking me through concepts in and out of class, and for making the lab a place to look forward to. Padraig Doran for finding glaring issues I had missed and helping me improve my practical understanding of geotechnical engineering. Mark Zablocki for helping me at odd hours of the evening/morning despite his schedule. And I would like to thank Mark's father, Ed Zablocki, for generously taking the time to teach me electrical engineering and help me improve and troubleshoot my piezo driver circuit and signal processing.

Finally, I would like to thank my family and our dog, Jess, for their endless love and support throughout my life and my time at Tufts. Without them I could not have done this.

III. Contents

IV. List of Tables

V. List of Figures

VI. Symbols

ADC	Analog-to-Digital Converter
BBC	Boston Blue Clay
BE	Bender Element
CRS	Constant Rate of Strain
KSC	Kgf/cm^2
LVDT	Linear Voltage Displacement Transducer
MPa	Megapascals
OED	Oedometer
PC	Personal Computer
PVA	Pressure Volume Actuator
RBBC	Resedimented Boston Blue Clay
RGoM-EI	Resedimented Gulf of Mexico Eugene Island Clay
TI	Transverse Isotropic
TX	Triaxial
C_c	Compression Index
C_{ij}	Compliance in plane i-j
CAUC	Anisotropically Consolidated Undrained Shear Compression Test
CIUC	Isotropically Consolidated Undrained Shear Compression Test
CK_0UC	K0-Consolidated Undrained Shear Compression Test
E	Young's Modulus
e	Void Ratio
G, G_{max}	Shear Modulus
IC	Integrated Circuit
K	Lateral Stress Ratio
K_0	Coefficient of Lateral Earth Pressure at Rest
n	Porosity
NC	Normally Consolidated
OC	Overconsolidated

OCR	Overconsolidation Ratio
p'	Average Effective Stress $(\sigma'_1 + \sigma'_3)/2$
q	Shear Stress/Deviatoric Stress $(\sigma'_1 - \sigma'_3)/2$
S_u	Undrained Shear Strength
t	Time
u	Pore Pressure
V_{pH}	Horizontal P-Wave Velocity
V_{pV}	Vertical P-Wave Velocity
V_{sHH}	Horizontally Propagating Horizontally Polarized S-Wave Velocity
V_{sVH}	Vertically Propagating, Horizontally Polarized S-Wave Velocity
$V_{p(\theta)}/V_{pI}$	Inclined P-Wave Velocity
w_n	Natural Water Content
ε_a	Axial Strain
ε_r	Radial Strain
ε_{vol}	Volumetric Strain
ϕ	Group Velocity
θ	Phase Velocity
ϕ'	Effective Stress Friction Angle
γ	Shear Strain
γ_t	Total Unit Weight
γ_w	Unit Weight of Water
ν	Poisson's Ratio
ρ	Bulk Density
σ'_h, σ'_v	Horizontal, Vertical Effective Stress
σ'_p	Effective Preconsolidation Pressure
σ_1, σ_2, σ_3	Principal Stresses
σ'_m	Mean Effective Stress $(\sigma'_1 + 2\sigma'_3)/3$
τ	Shear Stress

1 Introduction

1.1 Problem Statement

Propagated elastic waves provide a glimpse into the small strain (less than 0.01% engineering strain) elastic deformation behavior of soils, which are useful for site characterization before construction and earthquake engineering [1]. Geotechnical engineers and geophysicists are also interested in the velocity properties of soils and rocks because they allow one to identify strata, faults, obstructions, and reservoirs without disturbing the subsurface [2]. To obtain these parameters in the field, shear and longitudinal waves are propagated through the subsurface either using an array of wave emitters and receivers, down-hole techniques, or using cross-hole methods at depth. They also can be measured using drill string tools during boring [3].

Although these methods provide valuable velocity data, depending on the geologic setting the in-situ stress state, stress history, and engineering properties may vary immensely. In the Gulf of Mexico for example, as one drills further into the subsurface, the material transitions from high porosity, low strength clay (< 1 MPa) to nearly lithified, low porosity, stiff clay, commonly referred to by geologists as mudrock. The historic precedent of treating soil and rock as separate materials has led to this transition zone between soil and rock being understudied, so it is important to research how velocity and engineering properties evolve with the state of stress in sedimentary basins. Soils experience compression induced grain orientation and layering from climate cycles as they are buried deeper as well, resulting in velocity anisotropy [4, 5]. Velocity anisotropy can affect the inversion of wave reflection data to strata, as wavefronts can assume non-elliptical shapes. Another compounding factor is that the velocities of shear and longitudinal waves through soils are sensitive to the level of shear stress and mean stress the soil experiences. As mean stress increases the soil density increases, and the velocity increases as well. Due to the directional dependence of stiffness from material anisotropy, even a small amount of shear stress can greatly increase the velocity through the soil. Thus, controlled

laboratory wave experiments on clay soils (or mudrock for the geologists) over a wide range of stress on different stress paths are important for field data interpretation and analysis and for improving velocity models.

1.2 Scope and Objectives

The primary goals of this research were to: 1) Explore how velocity anisotropy compares in high quality intact versus resedimented Boston Blue Clay (BBC and RBBC), 2) Measure how velocity anisotropy evolves with different loading stress paths in RGoM-EI clay, 3) Experimentally test the relationship between shear stress, mean effective stress, and axial P-wave velocity during consolidation and undrained shear in RGoM-EI clay, and 4) Improve the wave pulse driver circuit technology to boost signal amplitude and eliminate sources of noise.

Additionally, an investigation into apparatus deformations with a given axial load or cell pressure was performed, as this is a known source of error that hadn't been previously considered in prior velocity studies. By knowing the axial apparatus deformation for a given axial load and cell pressure, one can correct the difference and thus improve the accuracy of velocity measurements.

1.3 Organization

This thesis is sequentially organized to describe to the reader what relevant steps were taken toward achieving the previously outlined research goals. The document is divided into seven chapters which are briefly described below.

Chapter 2 provides a summary of the background on velocity measurements of soils, and how this technology has evolved over time. It covers what experiments have been conducted previously, as well as how anisotropy is measured and conceptualized. Then, the effects of stress path compression and shearing are discussed, going into detail of the highly nonlinear material properties of clays and the factors affecting

velocity. To wrap up, modeled iso-porosity and iso-velocity and their implications are discussed.

Chapter 3 covers the compression behavior of the clay soils tested, which are BBC, RBBC, and RGoM-EI. The mineralogical constituents, engineering properties, and index properties of each material and how they are processed are described. The methods of intact sample preparation, resedimentation, and trimming are discussed in detail as well.

Chapter 4 describes the laboratory equipment used to conduct this research. This section goes into detail about the medium stress triaxial testing device, the piezoelectric actuators used to send and receive P and S-waves, the transducers used to measure pressure, stress, and displacement, and the driver circuit used to power the wave actuators. It also covers the analytical methods used to interpret the test data.

There are many details that can end up being the determining factor of whether a triaxial test is successful. One such detail is remembering to retract the piston before starting a new test, as this can instantly crush your freshly prepared specimen. Properly established protocols to ensure successful testing during this research are discussed in Chapter 5. This section covers how triaxial tests were set up in the medium stress devices, how velocity signals were collected and analyzed, how velocity actuators were calibrated, how the apparatus compressibility was measured, and how data was analyzed to obtain the anisotropy parameters and experimentally derived iso-velocity contours from the DAQ data.

Chapter 6 reveals the results of the last two years of research. It covers the effects of apparatus compressibility on velocity, examines the compression curves from the different materials and stress paths, and looks at how the anisotropy and iso-velocity curves evolve with increasing mean effective stress. Comparisons to in-house data are also made.

Finally, the collection of data and results are summarized in Chapter 7. The implications and technical considerations are discussed, and next steps outlining areas of improvement as well as an introduction to further avenues to research are explored.

2 Background

2.1 Introduction

Wave-based methods of subsurface sensing emerged after World War 1, when scientists began exploring commercial applications for sonar and seismograph technology. The basis of the technology is that if the time difference between the moment a wave is sent out and the moment the wave arrives to a sensor is known, one can measure the distance between the reflecting surface and the transmitter. The method is contingent on educated assumptions made about the wave velocity through the media, however, making velocity testing critical to accurate subsurface mapping. Geotechnical engineers typically experiment on soil specimens at low stresses ($\sigma'_v < 1$ MPa), as stresses encountered in the subsurface during typical construction methods rarely exceed 1 MPa. Geophysicists, however, are more interested in stresses higher than 10 MPa, where porosities can be as low as $1 - 5$ %.

One of the earliest patents of wave-based subsurface remote sensing technology was procured by Reginald Fessenden in 1917, who used refracted seismic waves between mine shafts to locate ore bodies in the subsurface [6]. A few years later, the first field test that used seismic reflection methods for exploration geophysics was carried out by John Clarence Karcher, who used technology to find subsurface petroleum reservoirs in 1921 [2]. Geotechnical engineers then began adopting wave propagation-based technology to study granular, porous materials. In geotechnical engineering, wave velocities became of interest because they provide non-destructive, dynamic stress-strain characteristics of soils and foundations temporarily exposed to vibrations during the construction process and earthquakes. One of the most thorough studies performed at the time was by Iida in 1939. Iida used P and torsional S-waves[1] propagated axially in his research and found that wave velocities for both

[1] P-waves, synonymous with primary waves, compression waves, longitudinal waves, pressure waves, or sound waves, are waves requiring volumetric change in the direction of propagation in an elastic

P and S-waves were dependent on the specimen height, water content, and porosity [7]. Further study by Paterson in the 1950s postulated P-waves could independently travel through the soil media and pore space, while S-waves propagate through the soil skeleton [8]. One of the first studies in saturated clays was conducted by Frederick Lawrence Jr. at MIT, who observed a strong interrelation between shear wave velocity, mean effective stress, and void ratio [9]. Lawrence Jr. noted that by knowing two out of the three variables, one could derive the third variable.

Though the principles remain the same, the technology has evolved so that wave propagation equipment can easily be added to triaxial cells, oedometers, constant rate of strain consolidometers and other geotechnical testing devices. Modern lead zirconate titanite piezoelectric crystals are stronger than their quartz counterparts and have become commonplace in geophysical and geotechnical testing labs.

2.2 Velocity Testing

The elastic properties of non-linear, deformable soils are important in the geotechnical and geophysical professions. Soil stiffness behavior is measured using P and S-wave propagation techniques in the laboratory and in the field. Lab velocity measurements are commonly conducted with the resonant columns, ultrasonic transducers, piezoelectric transducers, and bender elements. These methods produce similar shear modulus (G_{max}) values; however the piezoelectric transducer methods (bender elements, ultrasonic transducers) are easiest to perform, leading to their high popularity [10]. In the laboratory, these devices are used to measure the velocity of P and S-waves through soil specimens. The waves sent through the specimen only deform the specimen by fractions of a percent ($\varepsilon < 0.0001\%$), thus measured properties are considered linear elastic. Piezoelectric transducers—like the shear plate and dilation plate used in this research—deform upon stimulation when electricity is

medium. Shear waves, commonly referred to as S-waves, describe a wave that excites particle movement perpendicular to the direction of motion.

applied and generate electricity when deformed. This makes them excellent for sending and receiving P and S-waves through soil specimens, with the one drawback being the potential lack of coupling between the soil and plates at lower stresses.

In this research, a stack of Noliac shear plate and dilation plate transducers was used to measure P and S-wave velocities. All velocities are measured using an oscilloscope, where the difference between the time of arrival and the time of crystal stimulation provides the time necessary to calculate the wave velocity in the specimen as shown in Figure 1. System delay time for each of the five wave measurements are corrected for as well. In the lab, wave travel distance is always known because initial specimen height is measured, and all subsequent deformation is measured throughout the test with a displacement transducer (LVDT).

$$Velocity = \frac{distance}{time} \tag{2.1}$$

Shear plates provide the shear wave velocity (V_s), which allows one to derive the small strain shear modulus (G) of the material when combined with the total soil mass density as follows:

$$G_{ij} = \rho \times V_{S,ij}^2 \tag{2.2}$$

Where 'i' denotes the propagation direction and 'j' is the polarization direction of the shear wave [11]. G is a fundamental stiffness which is the initial slope of the stress-strain curve of a soil.

Dilation plates send and receive P-waves, yielding one of the following moduli based on the boundary conditions of the soil specimen. The elastic, or Young's, modulus is obtained when an elastic rod is uniaxially loaded and can deform laterally. The constrained modulus is when an elastic rod cannot deform laterally but is loaded uniaxially [12]. In this research, since the P-wave emitted by the crystal propagates orthogonally to the surface of origin and without lateral movement, the constrained modulus (M) is the appropriate modulus [13]. The constrained modulus is calculated from V_p and the known mass density as follows:

$$M = \rho \times V_p^2 \tag{2.3}$$

Since the bulk modulus (ratio of infinitesimal pressure increase to the resulting relative decrease in volume, K) is more commonly used to describe material behavior, the shear modulus (G) obtained in equation 2.2 and constrained modulus (M) from equation 2.3 are combined to calculate it as follows:

$$K = M - \frac{4G}{3} \tag{2.4}$$

These elastic parameters, including the Poisson's ratio—the ratio of transverse deformation to axial deformation of an applied force, are interrelated as follows:

$$M = \frac{2G(1-\nu)}{1-2\nu} \tag{2.5}$$

$$G = \frac{E}{2(1+\nu)} \tag{2.6}$$

$$E = \frac{9KG}{3K+G} \tag{2.7}$$

$$\nu = \frac{d\epsilon_{trans}}{d\epsilon_{axial}} \tag{2.8}$$

Where E is the Young's modulus and nu (ν) is the Poisson's Ratio. Although these are useful relationships for isotropic materials, soils are rarely isotropic. Regardless, these equations are still widely used for soils despite these shortcomings, contributing to inaccurate seismic surveys and geophysical subsurface maps.

2.3 Velocity Anisotropy

Materials tested in this study are Transverse Isotropic (TI), meaning that the material is isotropic in the plane normal to the symmetry axis. An example of this type of anisotropy would be to imagine stacked plates of steel with marshmallow in between. If one stepped on the top of the stack it would feel soft because of the marshmallow, but if stood on sideways it would feel like steel [14, 15]. In sedimentary

basins, this type of anisotropy has two major sources: the first being layer-induced anisotropy and the second being grain/pore orientation-induced anisotropy (Figure 2). Layer-induced anisotropy stems from differences in layer mineralogy, grain contact orientation, and/or grain size due to natural fluctuations in sediment source material over time during deposition. These cyclical fluctuations may be seasonal, climatic, or diurnal. Grain/void orientation-induced anisotropy on the other hand is caused by preferential orientation of anisotropic and isotropic mineral grains during compression of the soil [4]. Since mineral grains are rarely spheroidal and often have a long axis or tabular/platy structure, the long axis becomes more parallel to the horizontal plane during compression. Cracks are another potential source of anisotropy but are not considered in this research as none of the tested materials exhibited cracks. Resedimented samples only exhibit orientation-induced anisotropy, while anisotropy of intact samples from the field is caused by both sources (Figure 3). The effect this material anisotropy has on velocity characteristics of soils is known as velocity anisotropy.

Velocity anisotropy has been recognized since the 1930's, when early exploration geophysicists like McCollum and Snell found that their seismic wave velocities varied depending on the direction of propagation [16]. Postma in 1955 examined the mathematics behind velocity anisotropy in stratified materials [17]. One of the first studies that measured simple vertical versus horizontal velocity anisotropy in marine clays was done by Laughton in 1957 [18]. Laughton studied P and S-wave velocities of core sediments, collected from the seafloor in the north-eastern Atlantic basin, during one dimensional compression up to 500 kg/cm^2. He then unloaded and removed the samples from the pressure chamber and measured the velocity along the vertical and horizontal axes. In a seminal article in the 1980s, Leon Thomsen reviewed nearly all literature available on velocity anisotropy of sedimentary rocks, developed the theory behind anisotropy, and formulated a simple set of equations to quantify anisotropy of different TI materials like shale, mudstone, and sands [4, 5]. Thomsen's three proposed anisotropy parameters are as follows:

$$\epsilon = \frac{C_{11} - C_{33}}{2C_{33}} \tag{2.9}$$

$$\gamma = \frac{C_{66} - C_{44}}{2C_{44}} \tag{2.10}$$

$$\delta = \frac{(C_{13} + C_{44})^2 - (C_{33} - C_{44})^2}{2C_{33}(C_{33} - C_{44})} \tag{2.11}$$

where ε and γ represent compressional and shear wave anisotropy respectively and δ represents the inclined compressional anisotropy most relevant to seismic exploration [4]. Equations 2.9 and 2.10 represent the difference between the horizontal and vertical wave velocities normalized by the vertical velocity. Equation 2.11 is more complicated, however, as it characterizes the distortion of the wavefront from a perfect ellipse. Figure 4 shows how a spreading wave looks with different values of delta. The top figure shows the rare case of elliptical anisotropy, where the δ and ε are equal. The bottom figure shows the more common case where δ deviates from ε, giving rise to less elliptical wavefront geometries. Where δ is negative, a normal moveout would underpredict the velocity. This inclined anisotropy has a significant impact on field reflection data, as nearly all seismic survey velocities travel through soil at an angle. During a typical seismic survey, a series of evenly spaced receivers trail behind a wave source towed by a boat (Figure 5). The furthest receiver will receive the wave reflection from a particular bedding plane last, and that wave will be most impacted by the δ parameter. A normal moveout is the correction applied to the arrival time data in the field as there is a delay in arrival time from source to receiver.

Since TI materials are by nature anisotropic, the isotropic elastic modulus equations do not apply, and a symmetrical stiffness matrix with five independent parameters (C_{11}, C_{33}, C_{44}, C_{66}, and C_{13}) is required to fully characterize the elastic behavior (Figure 6). Thomsen's method derives these five stiffness parameters from the mass density, phase angle, and five independent phase velocities—vertical P-wave velocity (V_{pV}), horizontal P-wave velocity (V_{pH}), vertically propagating horizontally polarized

S-wave velocity (V_{sVH}), horizontally propagating horizontally polarized S-wave (V_{sHH}), and the inclined P-wave velocity ($V_{p(\theta)}$) (Figure 7) [4, 19]. It is important to note that all C_{ij} are calculated using phase (wavefront) velocity and angle, which are different than the group (ray) velocity and angle (Figure 8) [4]. The group velocity is the velocity of propagation of particle disturbance or energy, while the phase velocity is that of the expanding wavefront [17]. For the vertical and horizontal waves, the group angle is equivalent to the phase angle, but for the inclined wave the phase velocity and angle needs to be calculated before deriving δ using the Thomsen equation in 2.11. This is done by using Byun's method to convert the group angle and velocity to phase [20]. The three following equations illustrate the relationship between group and phase angle:

$$v(\theta) = V(\phi)\cos(\phi - \theta) \tag{2.12}$$

$$\tan(\phi - \theta) = \frac{1}{v(\theta)}\frac{\left(dv(\theta)\right)}{d\theta} \tag{2.13}$$

$$V^2(\phi) = v^2(\theta) + \left(\frac{dv(\theta)}{d\theta}\right)^2 \tag{2.14}$$

where $V(\phi)$ denotes the group velocity along the ray angle ϕ from the axis of velocity symmetry and $v(\theta)$ is the phase velocity [20]. Once the phase velocity and angle are calculated from the group values, C_{13} can be calculated and thus so can δ using equation 2.11. In this study, the exact equations from Thomsen 1986 were used to calculate the anisotropy.

2.4 Stress Path and Shear Behavior in Clay

To better understand the behavior of wave velocities in soils, the mechanical behavior and physical properties of the material should be recognized. Clays, the soil type of choice in this research, are fine-grained soils where 50% or more grains pass through a 75 μm sieve as defined by Casagrande's Unified Soil Classification System (USCS)

[21]. Clays in this research context refer to the soil type rather than clay minerals themselves (montmorillonite, halloysite, illite, etc.), although soils classified as clays contain clay minerals. Clay minerals themselves are < 2 μm, quite a bit smaller than the 75 μm sieve.

Stresses in soils have been studied extensively by geotechnical engineers since the early 1920's when Karl Terzaghi first sought to understand the mechanisms controlling their compressibility. In 1936, Terzaghi formulated the principle of effective stress, which is shown as follows:

$$\sigma' = \sigma - u \tag{2.15}$$

where σ' is the effective stress, σ is the total stress, and u is the pore pressure—note this concept only applies if the soil is fully saturated and grain to grain contact surface area is small (point contacts) [22]. It should also be noted that the effective stress principle in its simple form above may not apply to certain granular materials at very high stresses (<200 MPa). The implications of this equation are that a normally consolidated soil 10 ft below the seafloor under kilometers of water exhibits virtually the same soil engineering properties as an identical soil 10 ft below the bottom of a puddle [23].

If we picture an element of clay soil on the seafloor in a tectonically quiescent sedimentary basin, the mechanical compaction process begins as material is deposited on top of the soil element and it is buried. The seafloor clay element starts off with a high void ratio, high pore aspect ratio, and low density. As it gets buried deeper, the effective stress increases and the material compacts and densifies. If sediments are evenly deposited on a horizontal seafloor this type of compression is assumed to be one-dimensional, meaning that the soil element follows a linear path downward as it gets compacted. This type of uniaxial, equivalent-stress, time-dependent compression is referred to as K_0 consolidation in geotechnical engineering. In this case, the lateral stress exerted by surrounding soil elements is such that all deformation is confined to a single dimension and compression induced anisotropy is

enhanced (Figure 9) [24]. For this condition, lateral stresses are assumed to be the same in all directions along the horizontal plane, leading to the following:

$$K_0 = \frac{\sigma_h'}{\sigma_v'} \tag{2.16}$$

Where K_0 is the lateral earth pressure at rest, σ'_h is the horizontal effective stress, and σ'_v is the vertical effective stress. This ratio was shown by Jâky in 1948 and Bishop in 1958 (for normally consolidated clays) to relate to the critical state friction angle of soil with the following equation:

$$K_0 = 1 - sin\phi' \tag{2.17}$$

where ϕ' is the critical state friction angle [25]. While we generally assume the K_0 condition for simplicity, this stress condition is not always representative of the in-situ stress state. Instead, numerous factors like loading, excavation, salt bodies, tectonic stresses, over-pressure, heterogeneity, and topography induce complex stress states and stress paths on soils in the subsurface (Figure 10) [26].

In some cases, like near a salt body, the stress path of the clay element would undergo would deviate from the uniaxial condition (Figure 11). This type of compression where soils are loaded with differing principle stresses is commonly referred to as anisotropic consolidation [27]. During anisotropic consolidation in a triaxial compression test (CAUC test), the specimen is strained axially as well as the radially during loading due to the imposed lateral stress ratio, K. In the laboratory, K can be specified and computer controlled, allowing for stress paths of any K value to be imposed on test specimens. In the case of shearing during a triaxial test, undrained shear represents a case that can occur in-situ when low permeability sediment is loaded rapidly. The imposed shear stress is supported by the soil structure, and pore pressure develops in response to volumetric change. This type of shear represents the worst-case scenario strength-wise for a normally consolidated soil, as an elevation of pore water pressure leads to a reduced effective stress and thus lower strength.

2.5 Iso-Porosity and Iso-Velocity

In basins like the Gulf of Mexico, elevated shear stresses are encountered near salt bodies due to salt's viscous behavior—where salt maintains a K = 1 and deforms accordingly. These higher shear stresses cause volumetric changes of the surrounding sediments, resulting in elevated pore pressures until the excess pore pressure drains over time. If pore pressure deviates from predicted values, borehole stability issues can arise, which can negatively impact safety, the environment, and cost of drilling. Many methods exist to mitigate these borehole stability issues, and one recent method developed by UT GeoFluids is a coupled geomechanical and velocity-based pore pressure prediction method [28-30]. This model begins with 3D high-resolution seismic surveys to capture the shape of large geological structures in the area of interest. Then, a static finite element model is constructed for the area, where material parameters like density and lateral stress ratio are chosen for the varying sediments. The sediments are generally modeled as a poro-elastoplastic material using Modified Cam Clay (MCC), calibrated to experimentally-derived input parameters [29].

The velocity – equivalent effective stress relationship is calibrated at a nearby well and forms the basis for the pore pressure predictions. Equivalent effective stress is defined as the mean effective stress on the hydrostatic line (X-axis of the MIT P' – q plot) corresponding to points along an ellipse where porosity is equivalent (iso-porosity curve) (Figure 12). The equation for equivalent effective stress is defined in MCC as follows:

$$\sigma_e' = \sigma_m' \left(\frac{M^2}{M^2 + \left(\frac{q}{\sigma_m'}\right)^2} \right)^{\frac{\kappa}{\lambda}-1} \tag{2.18}$$

where σ'_e is the equivalent effective stress, σ'_m is the mean effective stress, M is the slope of the critical state line (function of ϕ'), q is shear stress, and κ is the slope of the experimentally derived recompression line in void ratio – σ'_m space, and λ is the

slope of the normal consolidation line (also experimentally derived and in e - σ'_m space). Since density is a primary control of the velocity in NC soil, it is assumed that for a given porosity, independent of stress state, the velocity will be the same. It is important to note that this assumption has not been experimentally tested on NC soil until this research. Since velocity is theorized to be equivalent where porosity is equivalent, the iso-porosity curve should also be the iso-velocity curve. The equation for the iso-porosity line depends on an elliptical yield surface, so if the yield surface shape deviates from an ellipse, the pore pressure predicted using the equivalent effective stress could be incorrect. Thus, it is important to experimentally derive the iso-velocity/porosity curve using a series of CAUC stress path consolidation tests at different K values with velocity measurements to explore the relationship between velocity, porosity, and shear stress. It is also important to see if the undrained shear stress path follows the iso-porosity curve and that P-wave velocity does not change during shear. If the points along the stress path corresponding to a particular velocity form an ellipse, and the undrained shear stress paths mirror the shape of the ellipse, then the relationships forming the basis of the model can be verified. Even more importantly, the effects of shear stress on velocity can be better understood.

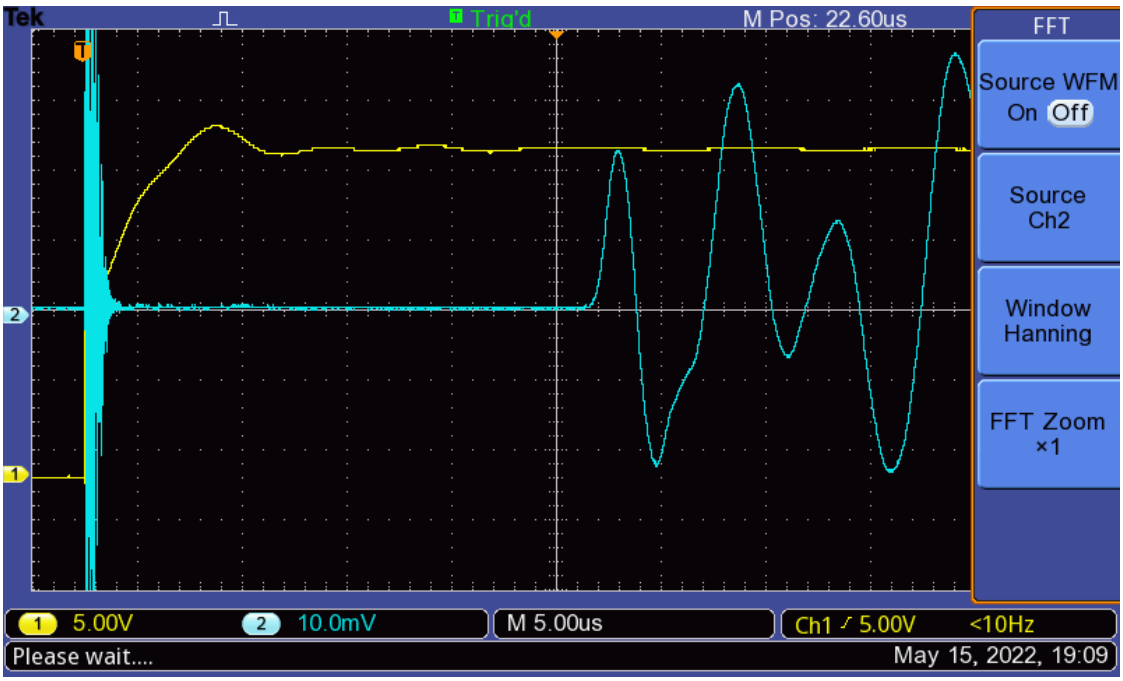

Figure 1. Example oscilloscope screen capture of V_{pV} showing input square wave (yellow) and received signal (blue).

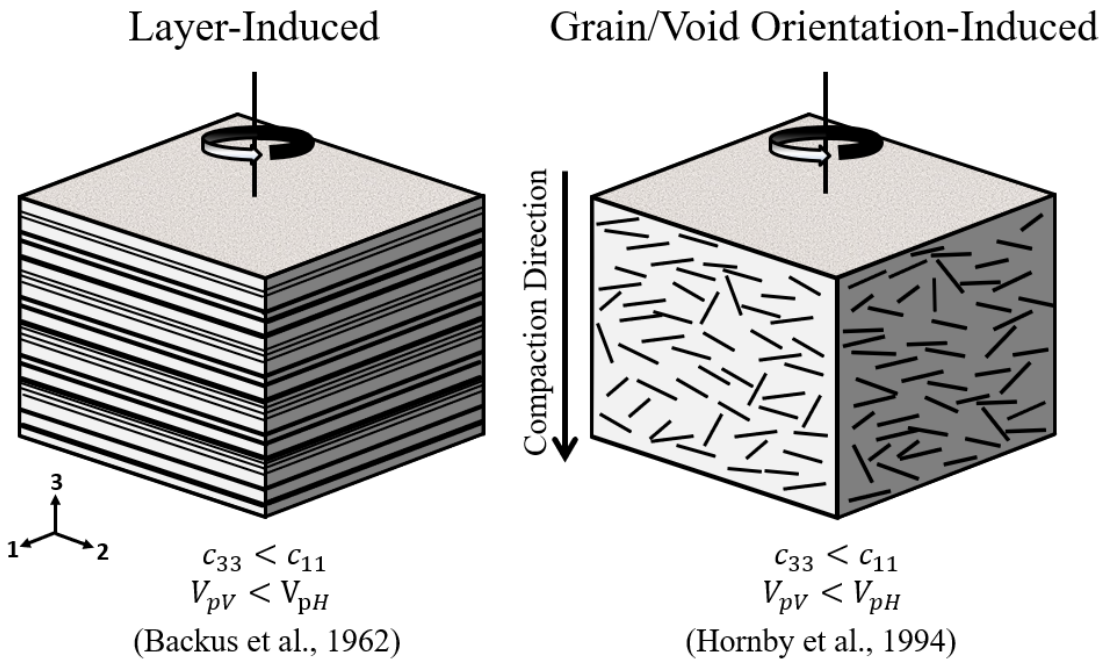

Figure 2. Graphical representation of the two main types of anisotropy focused on in this research

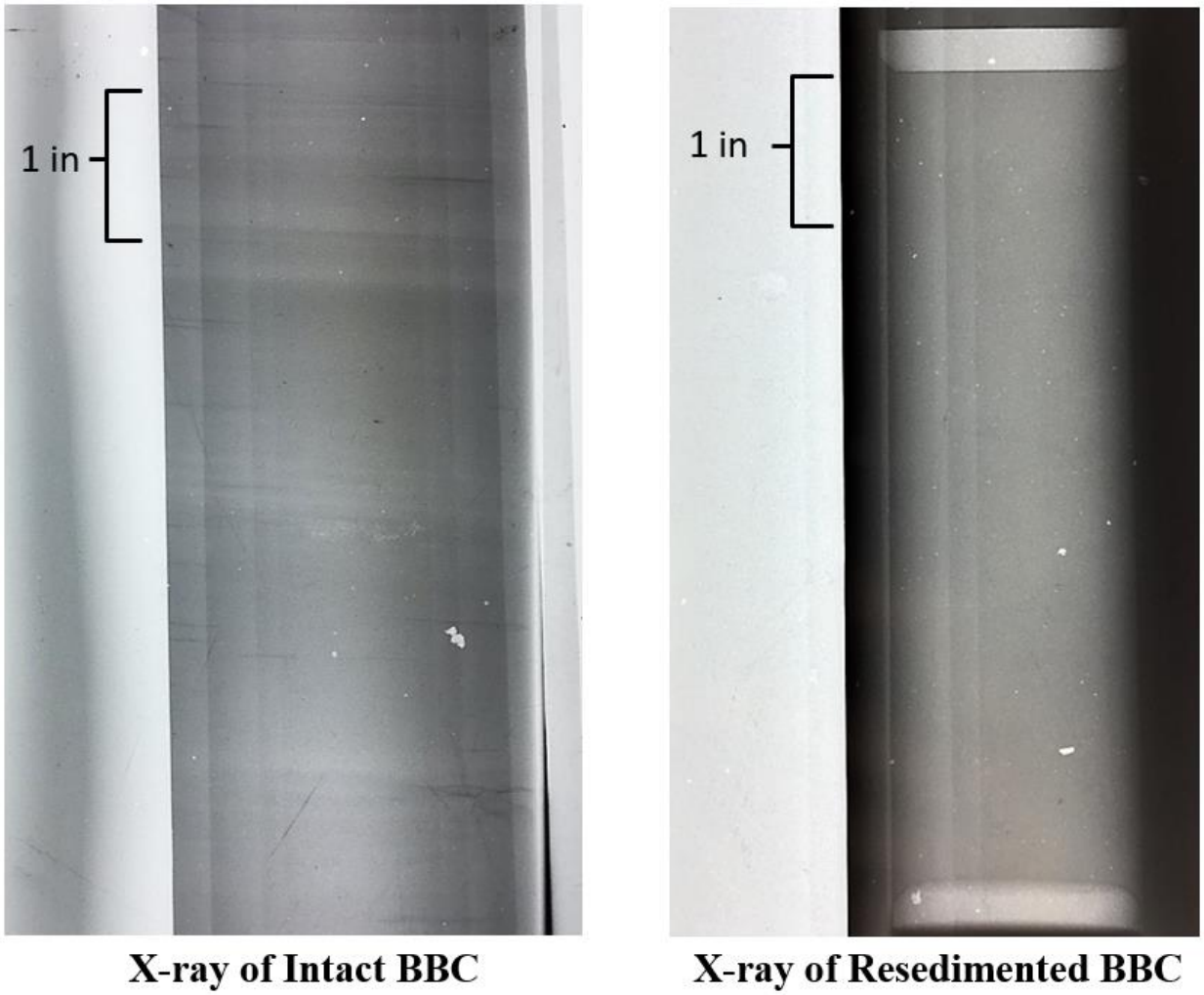

Figure 3. BBC from Cambridge, MA is shown on the left while RBBC is shown on the right. Distinct layering is visible in the intact material, while no layering can be seen in the resedimented.

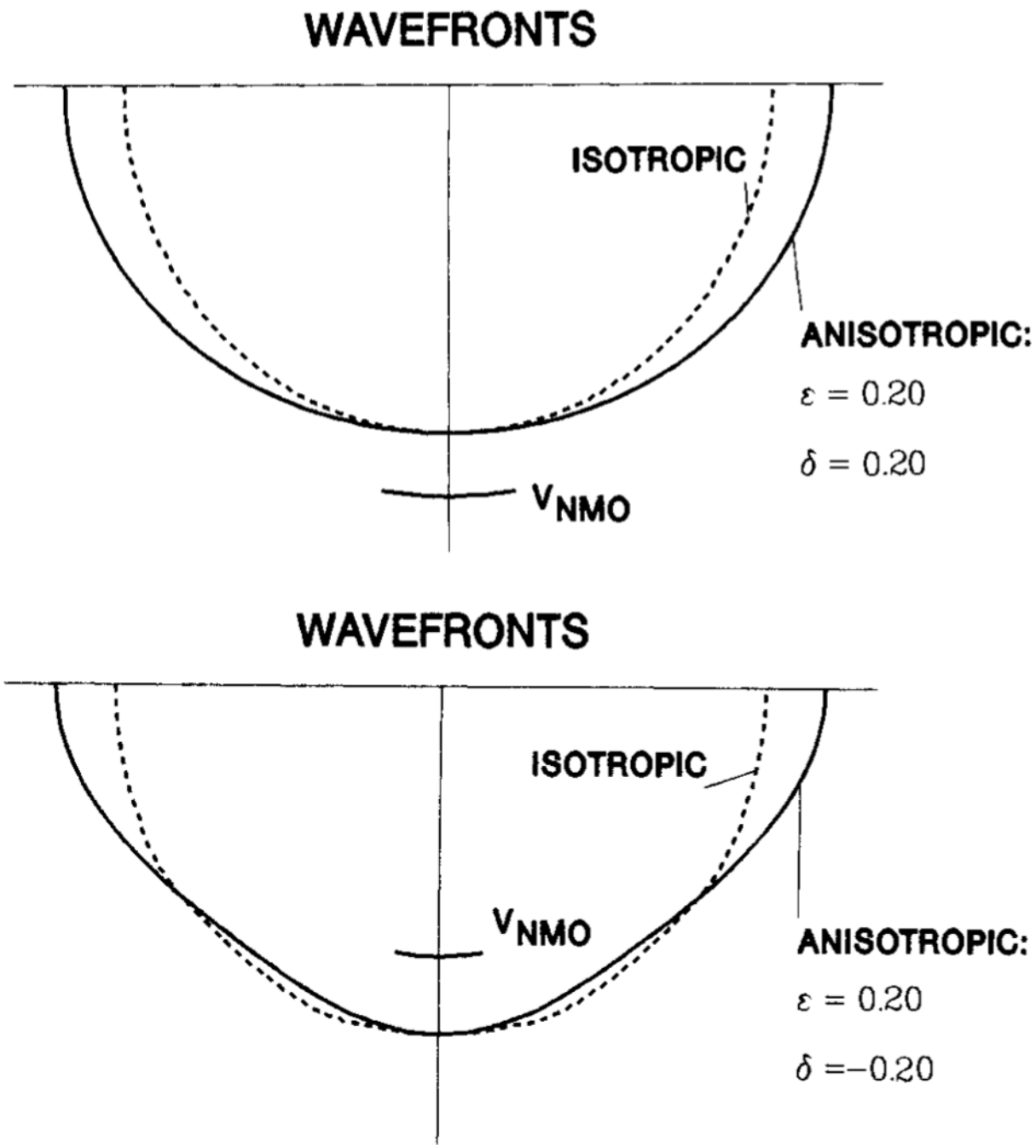

Figure 4. Wavefronts of anisotropic P-waves taken from Thomsen, 1986.

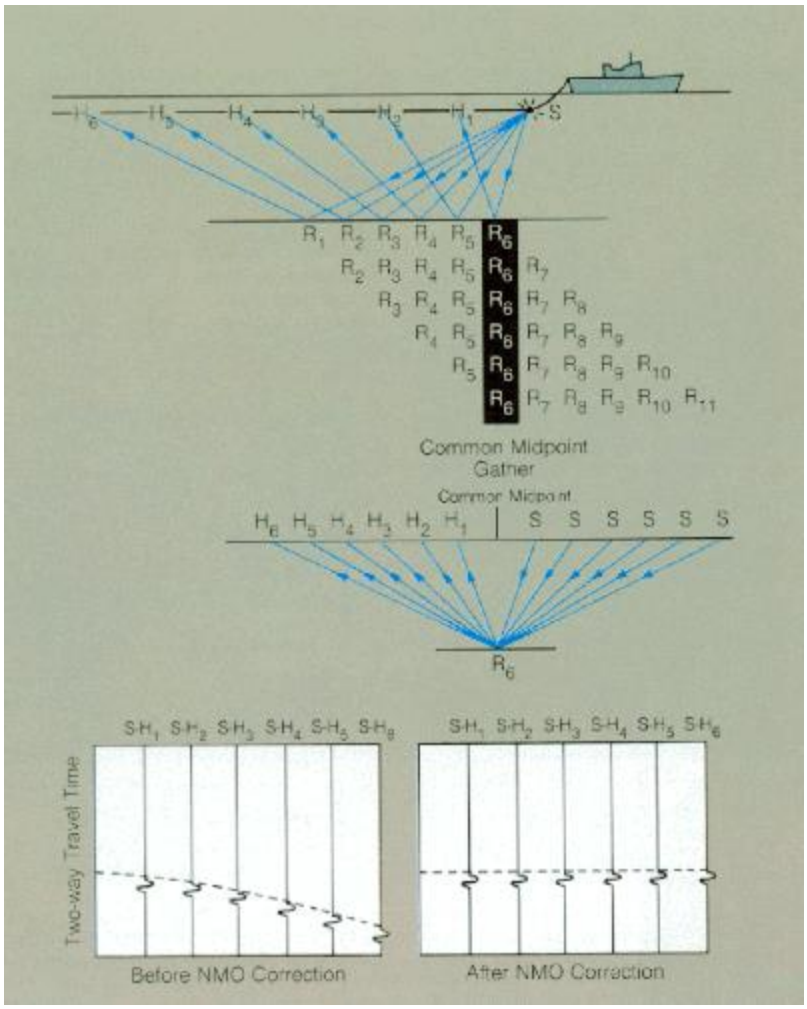

Figure 5. Illustration of normal moveout

$$\begin{bmatrix} C_{11} & C_{12} & C_{13} & 0 & 0 & 0 \\ C_{12} & C_{11} & C_{13} & 0 & 0 & 0 \\ C_{13} & C_{13} & C_{33} & 0 & 0 & 0 \\ 0 & 0 & 0 & C_{44} & 0 & 0 \\ 0 & 0 & 0 & 0 & C_{44} & 0 \\ 0 & 0 & 0 & 0 & 0 & C_{66} \end{bmatrix}$$

Figure 6. Compliance matrix with various C_{ij} parameters

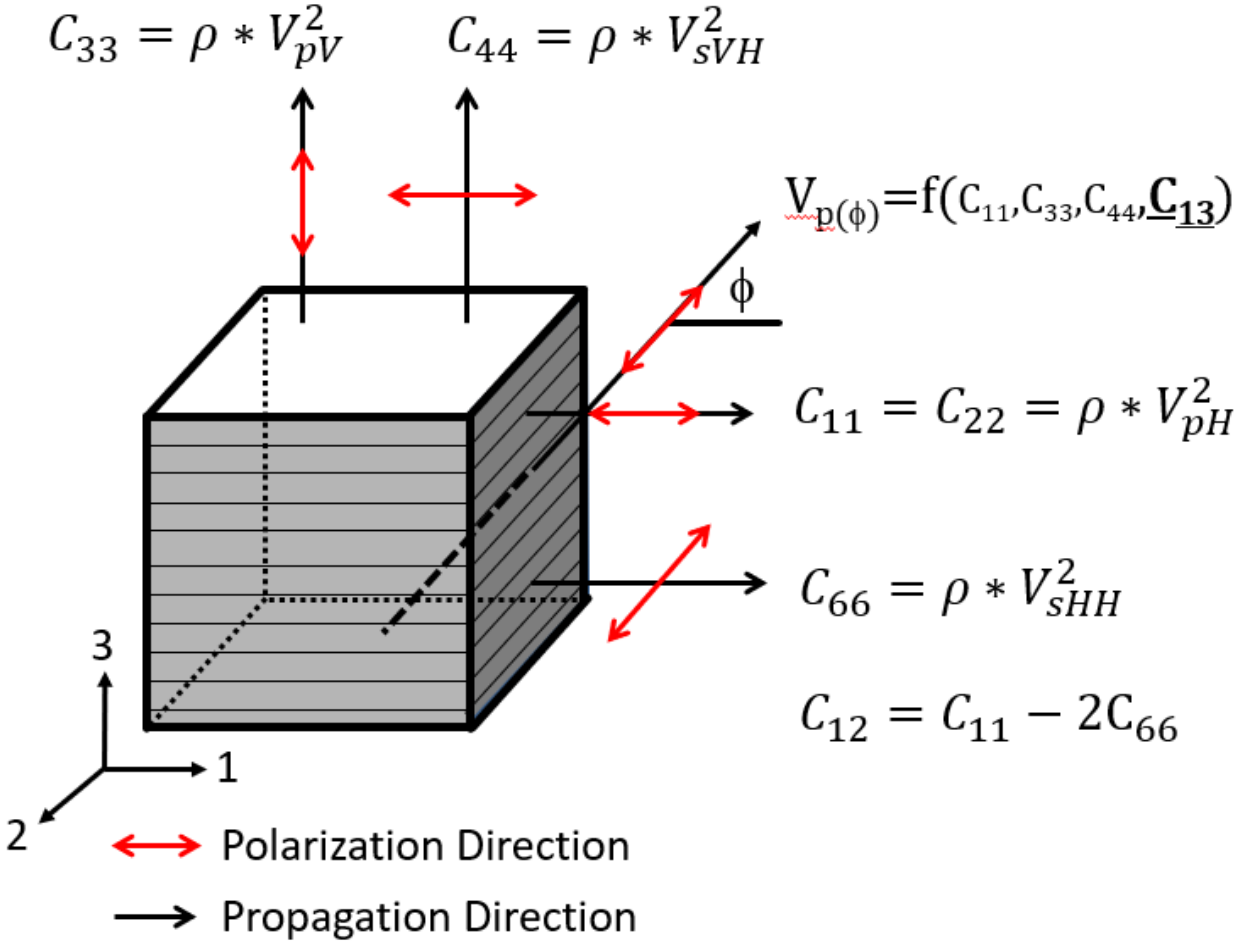

Figure 7. Graphical representation of the five independent velocities and the C_{ij} parameters derived from them.

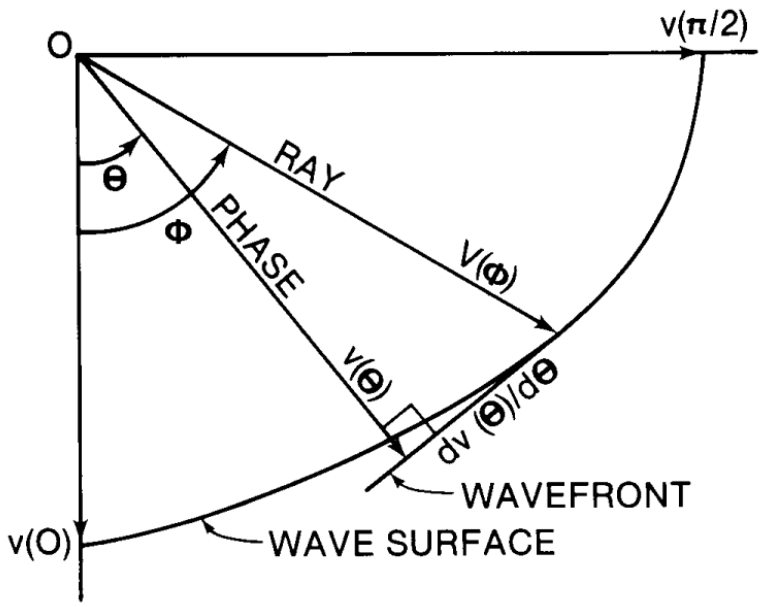

Figure 8. Illustration from Byun, 1984 showing the difference between group (ray) and phase velocity/angle.

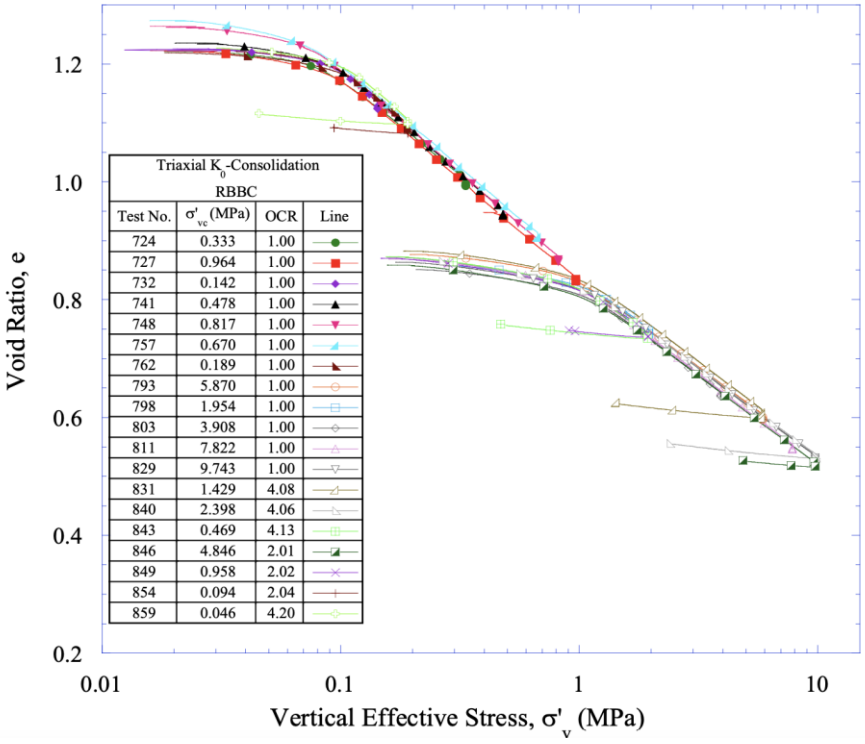

Figure 9. K_0 consolidation triaxial compression curve in e-logσ'_v of RBBC from Abdulhadi, 2009 [24].

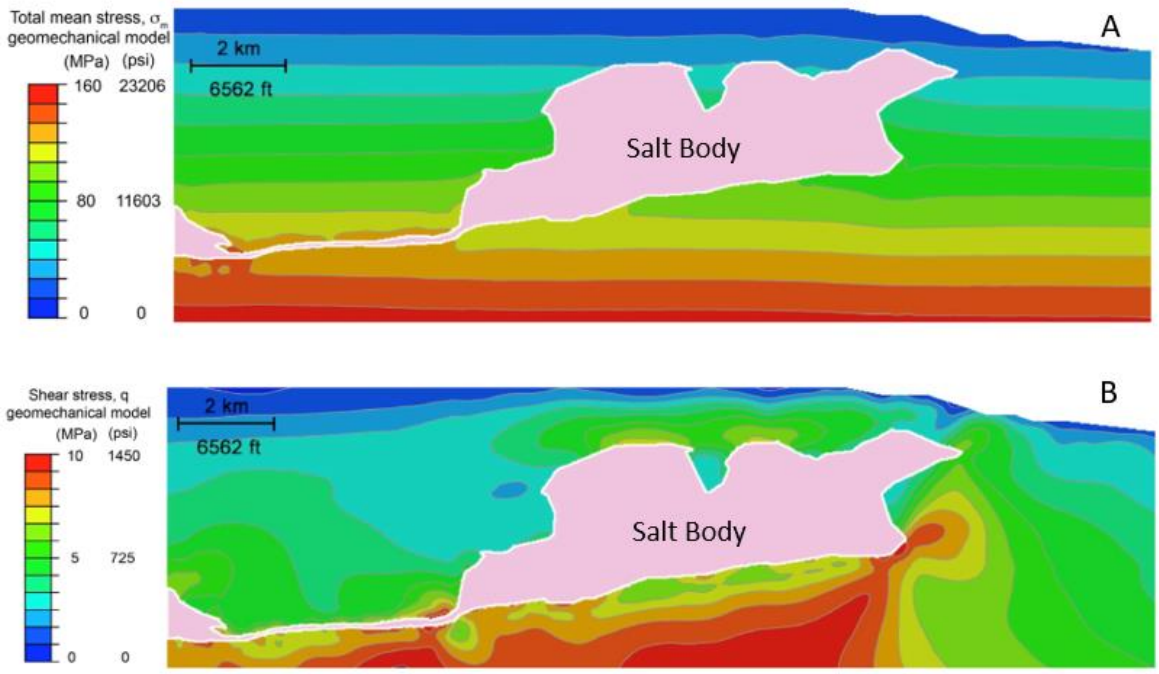

Figure 10. Cross section of subsurface near a salt body with A) mean total stress and B) shear stress shown in color.

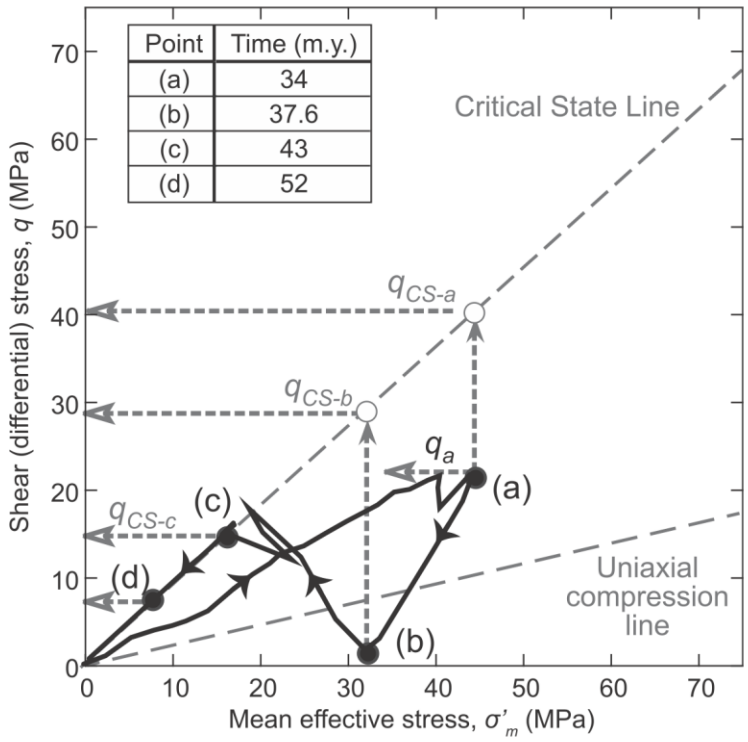

Figure 11. Stress path in mean effective stress – shear stress space of a modeled soil element at the top of a rising salt dome from Nikolinakou, 2017.

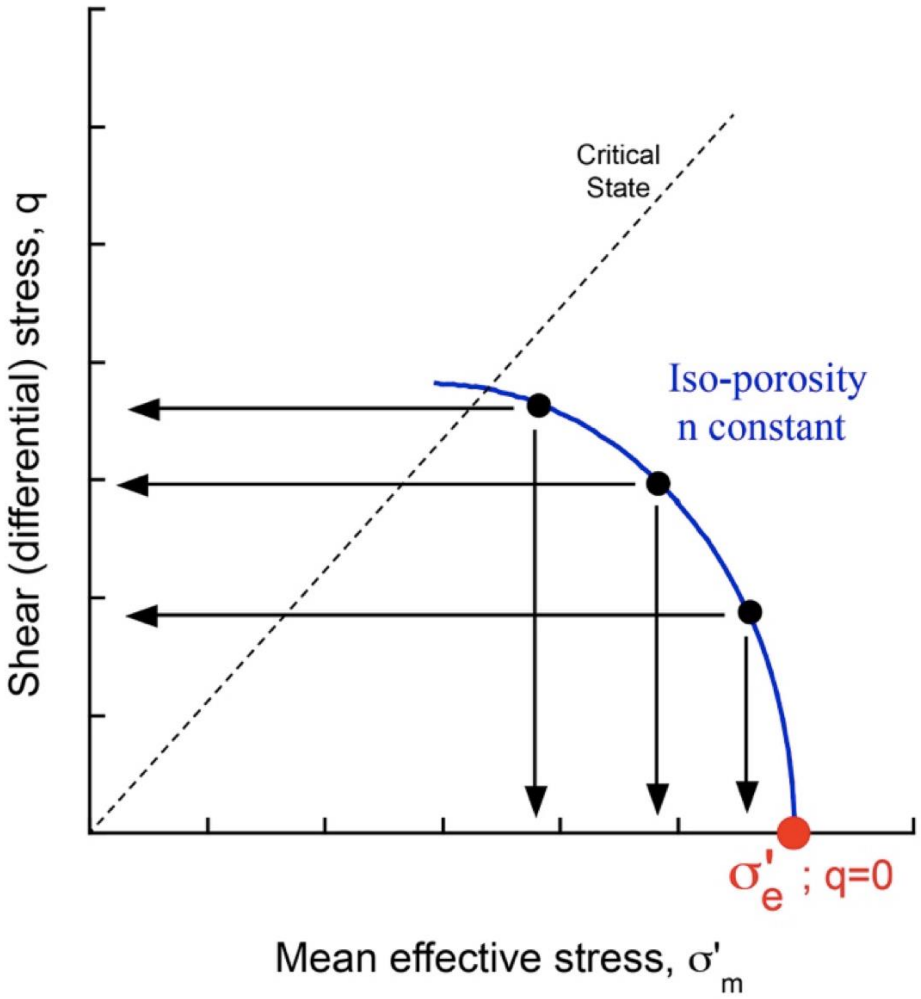

Figure 12. Idealized MCC iso-porosity curve (blue) in mean effective stress – shear stress space.

3 Materials and Specimen Preparation

3.1 Materials

Two main materials were tested in this study of velocity anisotropy and stress path velocity behavior. The first section of the research exploring velocity anisotropy of intact versus resedimented clay was performed on Boston Blue Clay, while the second part on the stress path dependence of velocity was on Resedimented Gulf of Mexico Eugene Island Clay. The portion of this research measuring the apparatus compressibility utilized a cylindrical hardened steel dummy specimen.

This chapter will discuss the origin, index properties, and differences between the various materials. Section 3.1.1 discusses Boston Blue Clay, 3.1.2 discusses Gulf of Mexico Eugene Island Clay, and 3.2 covers the intact specimen preparation procedure. This chapter concludes with an in-depth set of directions for conducting the resedimentation process and outlines the benefits and drawbacks of the method.

3.1.1 Boston Blue Clay

Boston Blue Clay (BBC) is a low plasticity, illitic, glacio-marine clay deposited during the retreat of the Laurentide Ice Sheet roughly 14,000 years ago in the greater Boston area [31]. Its in-situ soil properties like stress history, cementation, and thickness vary throughout the area, however much of Cambridge and Boston are underlain by a roughly 15 – 60 m thick layer of BBC [32]. The top few meters of the deposit in these areas are generally composed of a stiffer, oxidized, higher OCR rind, and the thicker middle portion is interbedded with silt and glacial till at the base of the unit. In this glacial period, the relative sea level was roughly 30 m above our modern mean sea level [31]. The presence of low levels of marine foraminifera in BBC indicates that although the material was deposited in a saline environment, there was a high amount of freshwater as well.

The behavior of BBC has been extensively studied due to its proximity to research universities like MIT, Tufts, and UMass Amherst and its spatial extent throughout the region. BBC is a favorable testing material due to its high fraction of silt-sized particles (47%) and relatively high permeability (k = 1.0E-15 m^2), which manifests in its low time to end of primary during incremental loading (Figure 13, Figure 14). This means that tests can be conducted at relatively high strain rates, so time consuming tests like the K_0 CRS test shown in Figure 15 can be performed relatively quickly.

BBC is a low plasticity clay, with the Unified Soil Classification System (USCS) designation of CL (Figure 16). Its Atterberg limits, specific gravity, clay fraction, and salt content are listed below in Table 2. Plastic limits were obtained using the rolling method on a glass plate and yielded a value of about 23.5%. The liquid limit was obtained using the Casagrande cup method and yielded a liquid limit of 46.5% [33]. From these values, a plasticity index of 22.7 was obtained, and a USCS classification of CL is derived [24]. The specific gravity was obtained using the procedure outlined in ASTM D854 using a calibrated iodine flask, where a G_s of 2.78 was obtained. Mineralogically, RBBC series IV is composed of mostly quartz and feldspar by weight percent, with the dominant clay-sized minerals being illite and illite-smectite (Table 1) [34]. The structure of the mineral assemblage is shown in Figure 17 at axial effective stress ranging from 0.1 MPa to 10 MPa.

Table 1. < 2 μm clay fraction mineralogy of RBBC and RGoM-EI Clay adapted from Adams, 2009.

Mudrock	Mineralogy Summary				Additional Data	
	Illite	Smectite	Other	Total	% Illite - Smectite	Expandability
	%	%	%	%	%	%
BBC	92	1	7	100	28	5
GoM-EI	30	65	5	100	87	70-80

The Series IV Resedimented Boston Blue Clay material was procured from backhoe excavation at a depth of 12 m under MIT's Koch Biology Building (#68) in Cambridge, MA in 1992. It is referred to Series IV because it is the fourth major sampling of

Boston Blue Clay conducted by researchers at MIT over time. The roughly 2500 kg of material collected was then softened with tap water and passed through a 2 mm sieve to remove gravel, organic detritus, and shells. Then, the soil was oven dried at 60 degrees Celsius and roller milled by Sturtevant Company so that 95% of material would pass a 0.152 mm sieve. Since not all material could fit in one batch, multiple batches were blended to ensure a randomized, uniform powder before storage in 40-gallon drums. The material in these drums is then distributed to 5-gallon buckets for ease of use in the laboratory, where it is stored until use in the resedimentation process.

Intact BBC, collected from various geotechnical projects around the Boston and Cambridge, MA area, is sampled using 3-inch diameter Shelby Tube with a fixed piston sampler to ensure a relatively undisturbed sample. Samples are then taken to the TAG Lab for X-ray imaging so the least disturbed, most uniform material can be selected for testing. The specimen preparation procedure is outlined below in more detail.

Table 2. Index properties of Resedimented Boston Blue Clay from Abdulhadi, 2009.

Year	Researcher	Batch	w_l (%)	w_p (%)	I_p (%)	G_s	Clay fraction (%)	Salt g/L
1994	Zriek	powder	46.4	22.5	23.9	2.78	60.1	
1994	Sinfield	powder	47.0	23.8	23.2	2.79		
		402	46.8	22.4	24.4			
		403	47.2	23.3	23.9			
1996	Cauble	powder				2.81		
		401	46.7	21.8	24.9			
		404	47.4	21.9	25.5			10.4
		405	45.2	22.1	23.1			10.0
		406	45.0	22.6	22.4		57.6	12.5
		407	44.6	23.0	21.6		57.8	13.1
		408	44.7	23.9	20.8		58.7	10.1
		409	45.4	24.0	21.4		56.8	13.0
		410	46.6	25.0	21.6			13.4
		411	46.7	24.5	22.2		56.9	10.2
		413	45.5	24.3	21.2			9.7
		414	46.3	24.3	22.0			12.0
		415	46.1	24.7	21.4			10.5
		416	46.7	24.0	22.7			12.9
		417	47.2	24.5	22.7			13.2
1998	Santagata	418						
		419	47.8	23.3	24.5			
1998	Force	420	45.2	22.6	22.6			
2009	Abdulhadi	powder	46.5	23.5	23.0	2.81	56.0	11.1

3.1.2 Gulf of Mexico Eugene Island Clay

Resedimented Gulf of Mexico Eugene Island Clay (RGoM-EI) is a high plasticity, smectite-rich clay (USCS designation CH) sourced from two boreholes off the coast of Louisiana from a location known as the Eugene Island Block (Figure 18, Figure 19). The core material, obtained in 1997, was sourced from roughly 2,330 – 2,455 m below the seafloor. This material had an in-situ porosity of 0.23 and a salinity of 80 g/L—several times that of RBBC. After the core material was extracted, it was air dried at room temperature then roller ground to a fine powder with 99% of material passing through a 0.152 mm sieve. Once ground, the material was blended to ensure homogeneity and stored at the University of Texas, Austin.

RGoM-EI has a liquid limit of 87% and a plasticity index of 63%. The soil has a clay fraction of 65% and reacts moderately to water (Figure 20). What makes this clay challenging to work with in the lab is its very low permeability (Figure 21). The permeability is about two orders of magnitude lower than that of RBBC, meaning that it takes about 100 times longer to reach the end of primary consolidation. This slows down the resedimentation process considerably and means that errors in effective stress due to excess pore pressure can arise if strain rates are too high. The silt-size grains are mineralogically composed of quartz, feldspar, and dolomite, with the clay-size fraction mineralogy being predominantly smectite (65%) and illite (30%). It has a concave up log linear K_0 normal compression curve as opposed to the more linear curve of RBBC (Figure 22).

3.2 Intact Specimen Preparation

Once intact samples are brought back to the lab and radiographed to assess their quality, they are ready for cutting and specimen preparation. A good quality section of sample is shown in Figure 23, where the horizontal layers were not deformed by the tube advancing into the clay during sampling. This section was selected for triaxial testing in this research. After selecting the area and taking note of the cut

section in the sample log (and putting on glasses for safety), a slow-speed, horizontal metal cutting bandsaw is used to cut out the desired 4-inch-long section of pipe. Leaving about a half-inch of extra length on each end ensures that disturbance from sawing and metal shavings do not affect the specimen. Immediately after cutting, all cut edges are de-burred on the inside of the tube and filed down on the outside to avoid injury during handling. After filing, a roughly 3 mm section of clay from both filed ends is removed with a metal spatula as it is generally contaminated with metal shavings from the cutting process. Once the remaining tube is cleaned and smoothed, it is resealed with a core cap and electrical tape for storage.

Next, the sample needs to be extruded from the sample tube section. While some commercial labs simply extrude specimens at this point, doing so can result in significant sample disturbance due to the bond that forms between the soil and the sides of the tube over time [35]. To minimize the disturbance during extrusion, one needs to free the specimen from the tube walls using a fixed clamp, hollow 1 mm diameter tube, piano wire, and plyers. First, the clamp should be used to fix the piano wire at one end so it does not move. The hollow 1 mm tube should have one pinched end and be longer than the sample, as one needs to slip the piano wire through the sample with the hollow tube. Push the pinched end into the sample right at the boundary between the inside of the steel pipe and the soil. At this point, slip the piano wire into the hollow tube. Once the pinched end pokes through the other side, it can be pulled all the way through, leaving the piano wire poking out enough to grab with the plyers (Figure 24). After rotating the wire along the inner edge of the tube one or two revolutions, the sample should now easily come out of the tube during extrusion, causing minimal damage (Figure 25). At this point the tube is disposed of, as mass, density, and water content measurements will be conducted on the specimen after trimming to a known geometry.

The next step is to trim the specimen to the desired shape for testing, which is done using a wire saw, long razor blade, and series of miter boxes. A wetted paper towel should be kept nearby throughout this process to keep the wire saw and razor blade

clean to prevent smearing on the cut surfaces. The specimen requires a rough trimming after it comes out of the steel pipe, as the 3-inch diameter sample needs to be trimmed down to a 1.4-inch diameter specimen. Using the wire saw, cut one slice perpendicular to the long axis of the clay cylinder about 1 cm from the end to reveal a flat, fresh edge. The sample is placed with this edge down on a cutout of wax paper so that it does not stick to the miter box during the trimming process. Once the flat edge is face down, the rotating bottom pedestal from the triaxial specimen trimming box is placed on top of the sample as a guide so that too much material does not get removed (Figure 25). Using the same vertical blade guide as for the first cut, use the wire saw to make several cuts to remove most of the excess clay material (Figure 26). Once the sample is lean enough, place it in the triaxial specimen miter box to be trimmed to a right cylinder (Figure 27, Figure 28).

From here, the trimming process is identical for resedimented samples. For one revolution, make cuts every 5 degrees using the wire saw placed up against the vertical guides to create a cylinder. These cuts are not perfectly flush with the guides due to the wire deforming, so about two more revolutions with cuts every 5 degrees using the long razor blade are necessary. At this point, a typical circular cylinder triaxial test specimen would be ready after removing the extra material from the ends of the specimen. For this research, however, two further cuts are required, as shown by the red dotted lines in Figure 28. The author designed a custom miter box to make these cuts so that specimen geometry would be reproducible (Figure 29). The cuts are made similar to before—first with the wire saw and the second with the razor blade, producing the final specimen geometry (Figure 30). This geometry allows the side velocity actuators to be mounted, as they require a flat contact surface for optimal coupling.

3.3 Resedimentation

Resedimentation is the process used in the laboratory to systematically produce identical, reproducible samples from core or excavated material with any desired porosity, stress history, and pore fluid salinity. It enables these variables to be separated and subjected to systematic laboratory investigations, a process which is not possible with intact samples, as even within the same core or Shelby tube the intact specimen's engineering properties can vastly differ. Intact samples also incur sampling disturbance upon retrieval which can alter the stress history, degree of saturation, and fabric. Resedimented samples only get disturbed once during extrusion, and by choosing an appropriate OCR (in this case, OCR = 4) the sample will still be in an isotropic stress state, minimizing the level of disturbance due to anisotropic swelling. Resedimentation, however, cannot capture all characteristics of intact samples. Factors like layering, cementation, and fabric developed from the sediment deposition process are not easily reproducible. Another issue is that specimens may not be uniform due to frictional effects from the walls of the tube during consolidation. This means that a specimen taken from near the ends of the tube may not have the same soil engineering properties as one from the middle of the sample. Although these factors remain difficult to control, the compressibility behavior of resedimented samples is very similar to those from their intact counterparts (Figure 31, Figure 32) [36].

Resedimentation was initially adopted in the early 1960s by Bailey at MIT, and since then it has evolved based on research needs and as processes have been further streamlined [37]. Today, nearly all tests ran in TAG Labs are done on resedimented samples due to its obvious advantages. This study is no exception, where about 90 percent of material tested are resedimented. That said, we are always interested in making comparisons to intact samples.

The resedimentation workflow is relatively straightforward after practice, though somehow the clay slurry finds a way to get everywhere. The first step is to decide the material and amount of choice for testing, the powder's salt concentration, the water

content of the slurry, and the pore fluid salinity. These parameters decide the ratio of sea salt, distilled water, and clay powder necessary to produce a sample. This can be easily accomplished using Dr. Germaine's custom spreadsheet, the "Salt Mixing Guide." This spreadsheet allows one to account for factors like water temperature dependent density, sea salt effective density, density of salt water, and different salt types. Generally, for a 1 ft long, 1.7-inch inner diameter resedimentation tube, 250 g of dry clay powder is necessary. If resedimenting a 3-inch inner diameter samples of the same height, this value needs to be quadrupled. Before mixing the ingredients, the sea salt must be dissolved in water. Once that is done, and the appropriate dry mass of soil is poured into a mixing bowl, set the mixer to the lowest setting while carefully adding the salt water. At first the consistency will be clumpy, but after some time the clumps will disaggregate and form a smooth slurry. At this point, the speed of the mixer can be increased. In total, the mixing process should take roughly 20 – 25 minutes. Check the slurry consistency occasionally by running a spatula along the edges to check for clumps. If no clumps are present, cover the slurry in plastic wrap, label it, and let it sit for 24 hours to temper. Tempering allows the clay particles to fully hydrate.

Once tempered, the slurry is ready for another mixing before de-airing. De-airing is done by placing the bowl in a vacuum chamber and applying a vacuum until almost all bubbles disappear. Often the slurry will expand twofold during this process, so proceed with caution. Adding a fluid trap to the vacuum line is recommended. After the slurry is de-aired, it is ready to be funneled into a consolidometer.

At this point, a few items need to be prepared. The sides of the consolidometer should be lightly lubricated with silicone oil to make extrusion easier once consolidation is complete. Then, a water basin for the consolidometer to sit in needs to be filled with water of the same salinity as the pore fluid. Additionally, before pouring the slurry in, make sure that the porous stones and nylon mesh filter chosen to fit inside the consolidometer are the correct size so that clay does not pour out of the bottom when funneled in. The friction of the porous stone/mesh acting against the inside of the

consolidometer will be inconsequential compared to the force acting axially on the sample, so it is acceptable if the stone requires light pressure to slide in to the consolidometer. In other words, a choice is made whether one wants extrusion or minor frictional loss of stress. Once the slurry is in the tube, the basin is filled about an inch above the porous stone, and another well-fitted porous stone and mesh are placed on top of the soil column. At this point, the incremental loading process begins. On day one, the porous stone acts as the load increment, thus obtaining the dry mass of the porous stone is necessary. A load increment ratio of 1 (total load is doubled every loading) was used in this research. From experience, for RBBC in a 1.7-inch diameter, 12-inch tube, the tube can be loaded about every 24 hours. For RGoM-EI in the same tube, however, it takes a few days before the end of primary consolidation, thus the load is doubled every three days. The tube can dry out if not topped off with distilled water, so it is important to keep an eye on the water level in the tube and basin. The author puts a water level mark on the basin to maintain the fluid salinity. For this research, all resedimented samples were consolidated to an axial effective stress of 0.8 MPa. They were then unloaded to an OCR of 4 a few days before extrusion to allow for swelling to complete. This stress and OCR allowed for ease of handling while trimming and a reasonable amount of axial strain (10 – 20%) during consolidation. Once consolidation is complete, take the weights off the consolidometer, pour out the extra salt water from the tube, extrude, and trim the sample as explained above. A simplified version of this workflow is shown in Figure 33.

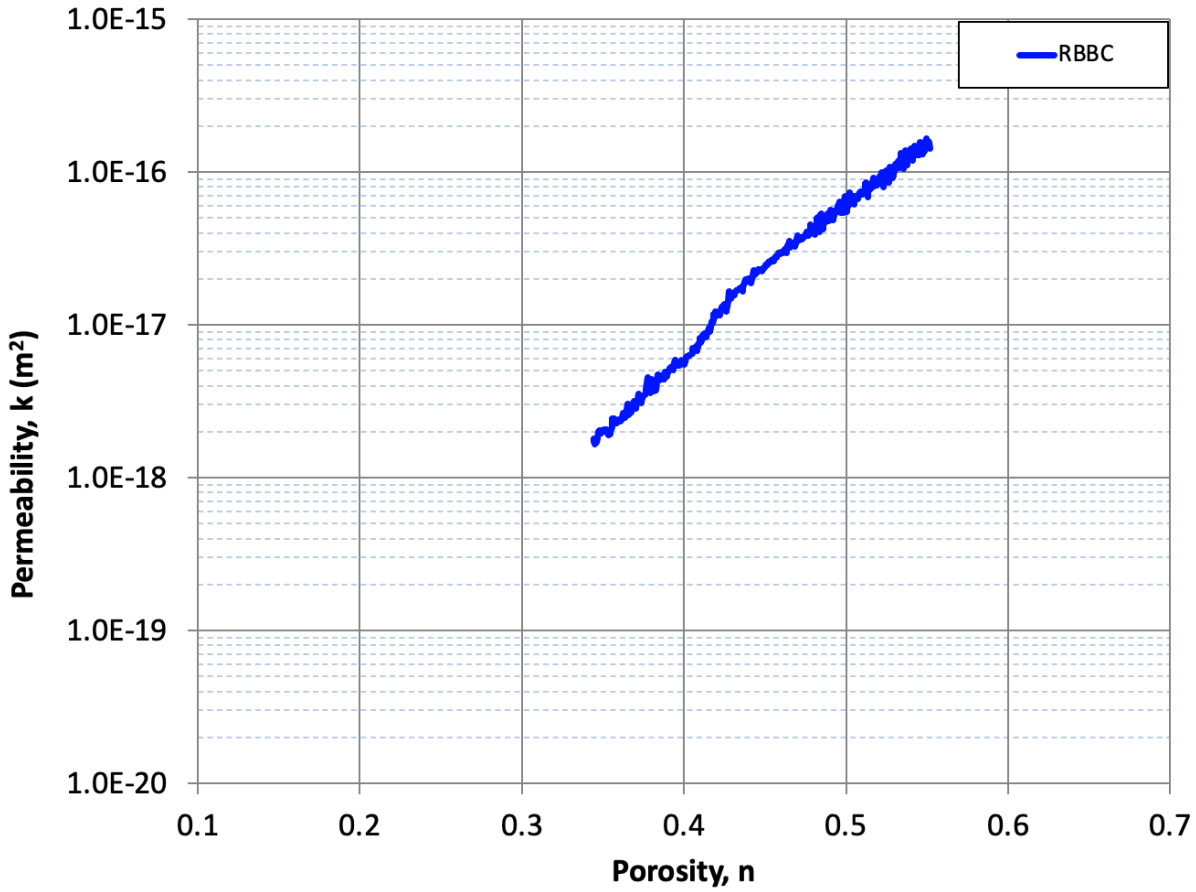

Figure 13. Permeability of RBBC derived from CRS test. Retrieved from UT GeoFluids Website 8 June 2022.

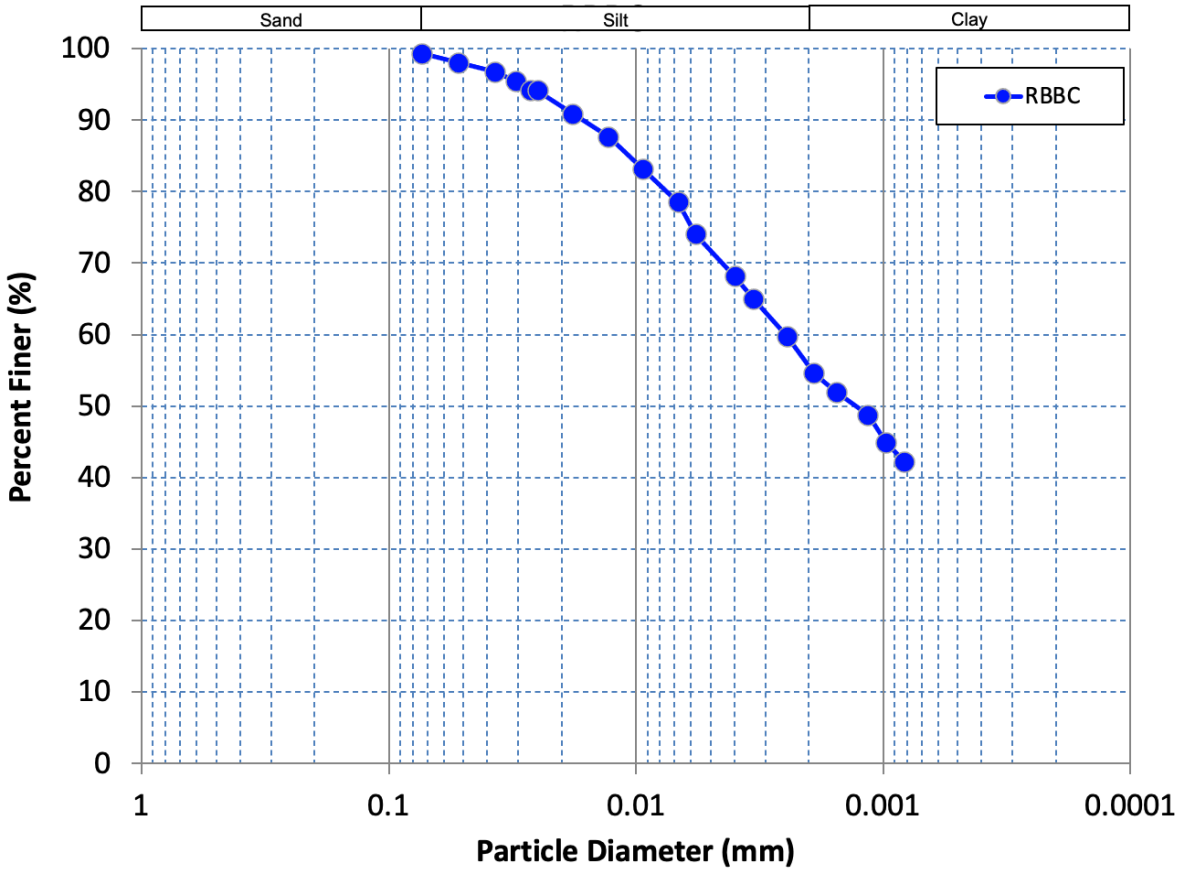

Figure 14. Grain size distribution of RBBC series IV. Retrieved from UT GeoFluids Site on 8 June 2022.

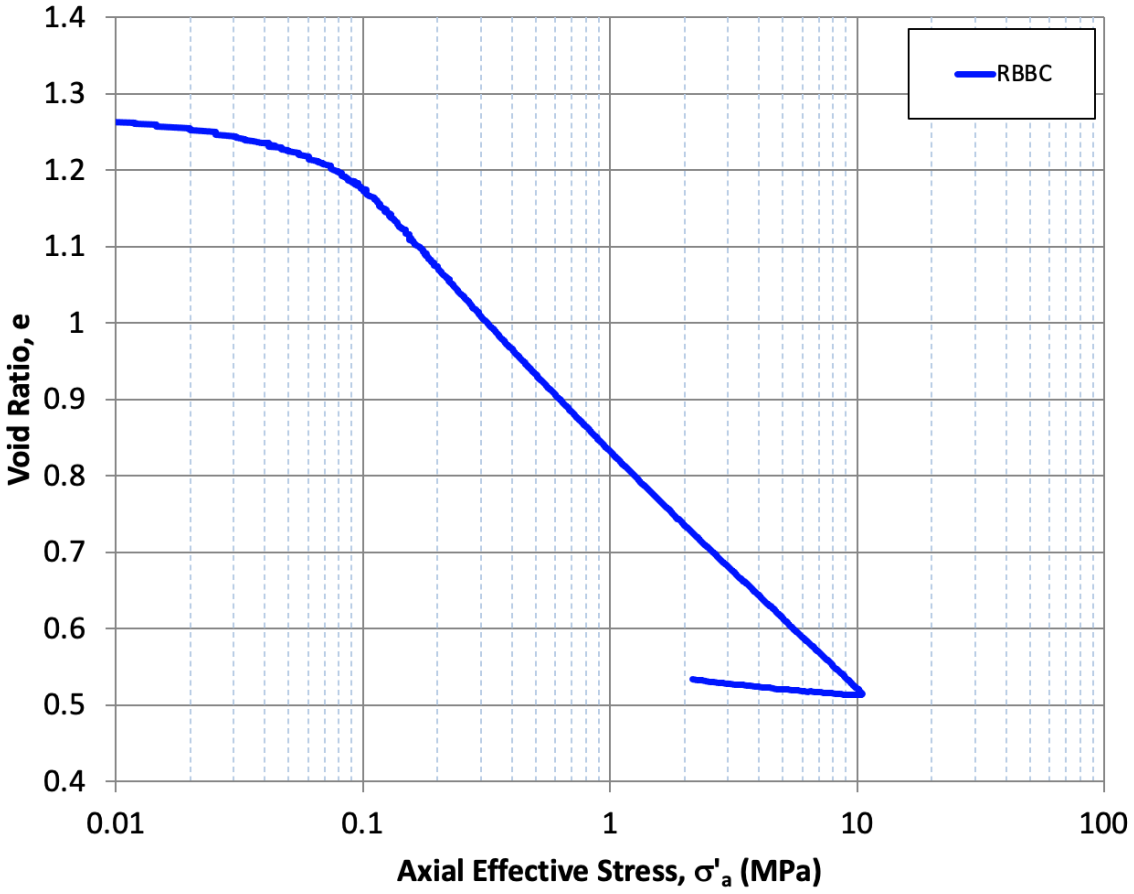

Figure 15. Compression curve of a CRS test of RBBC Series IV from 0.01 to 10 MPa axial effective stress. Retrieved from UT GeoFluids Site on 8 June 2022.

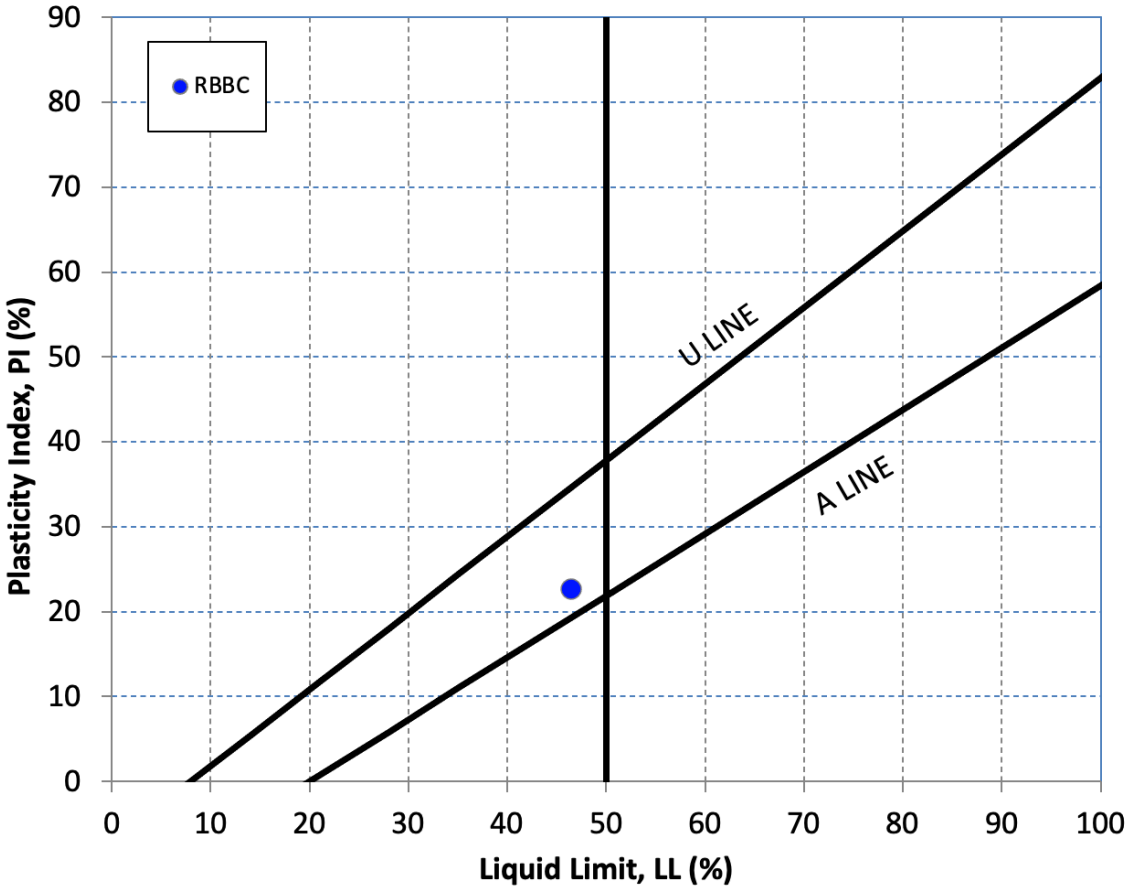

Figure 16. Atterberg limits obtained from multiple tests place RBBC in the CL region of the Casagrande plasticity chart. Retrieved from UT GeoFluids Site on 8 June 2022.

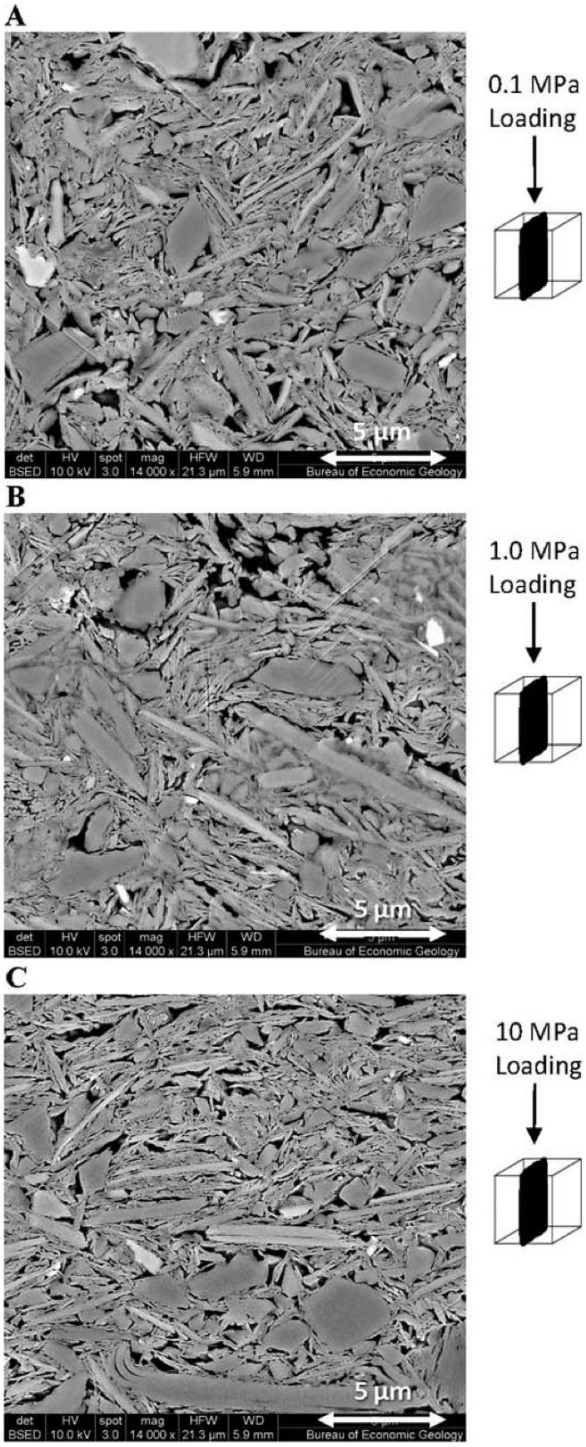

Figure 17. Backscattered Scanning Electron Microscope (BSEM) image of RBBC at A) 0.1 MPa, B) 1 MPa, and C) 10 MPa axial effective stress. Note the grain reorientation, where image analysis shows a 22 degree change in mean particle orientation from 0.1 vs 10 MPa. Image taken from Emmanuel and Day-Stirrat, 2012.

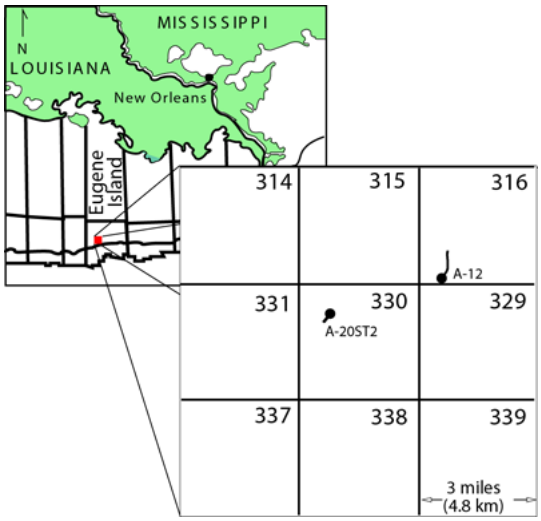

Figure 18. The Eugene Island site is located off the coast of Louisiana. Cores were obtained from the two dots on the grid. Retrieved from UT GeoFluids Site on 8 June 2022.

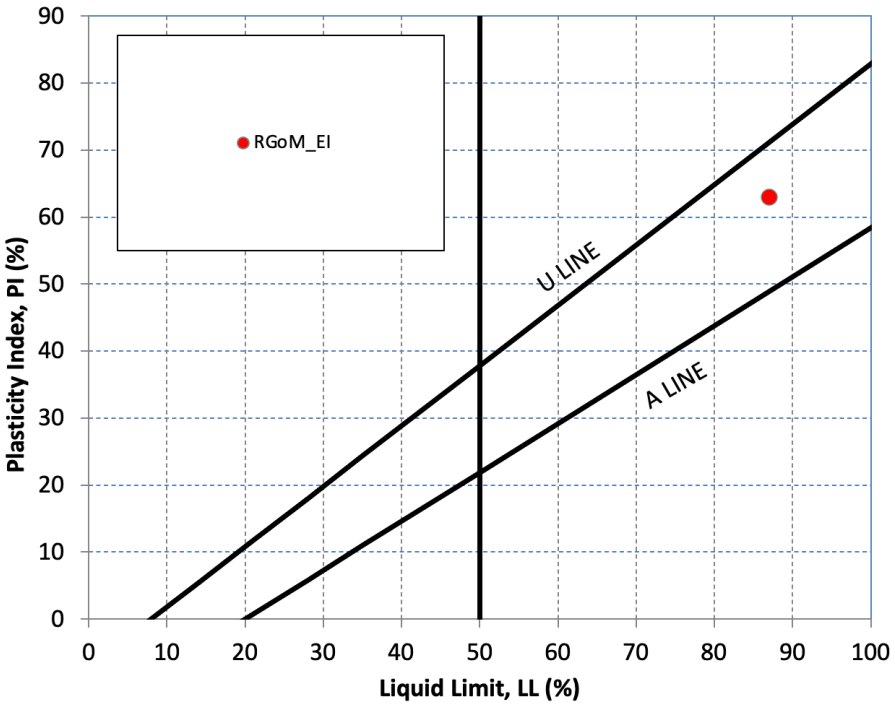

Figure 19. Casagrande plasticity chart of RGoM-EI shows it plotting in the high plasticity clay (CH) range. Retrieved from UT GeoFluids Site on 8 June 2022.

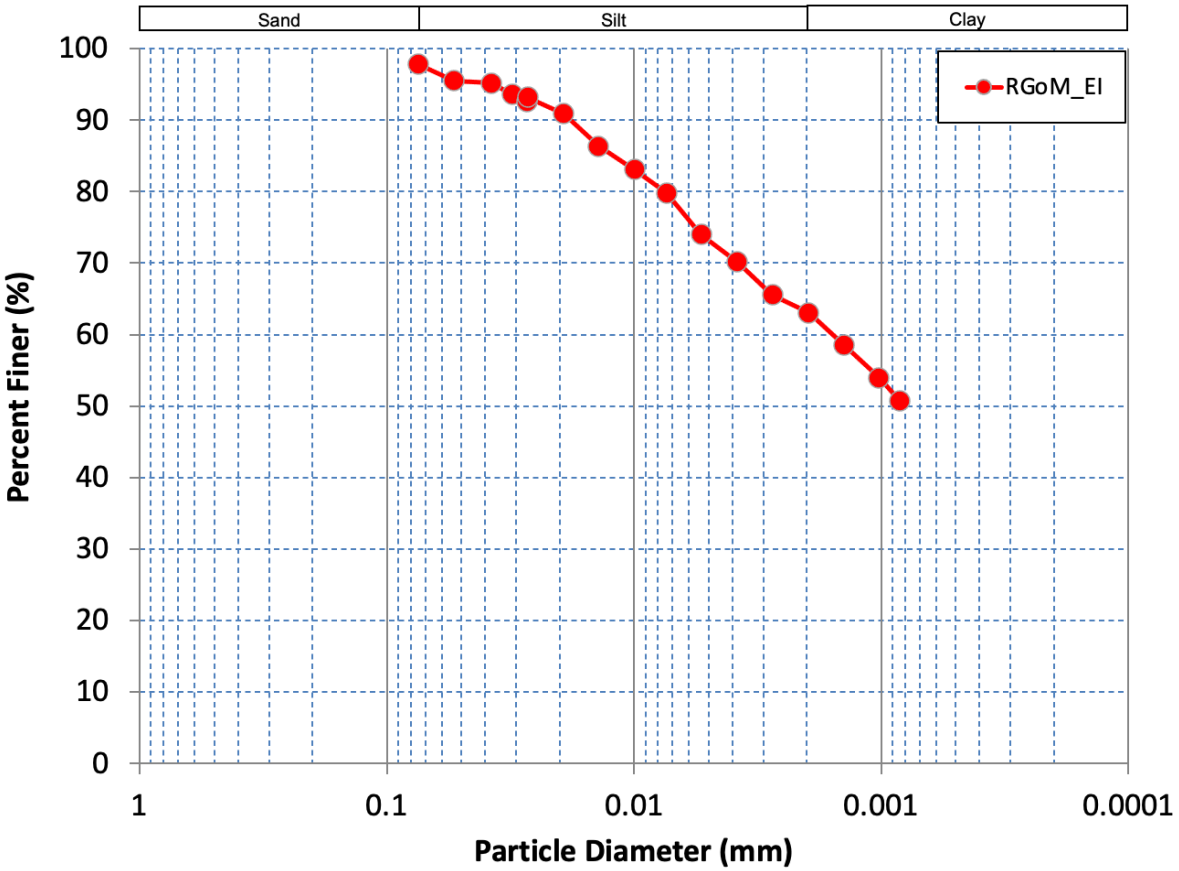

Figure 20. Grain size distribution of RGoM-EI clay. 97% of material passes the 75 µm sieve, and it has a clay fraction of approximately 65%. Retrieved from UT GeoFluids Site on 8 June 2022.

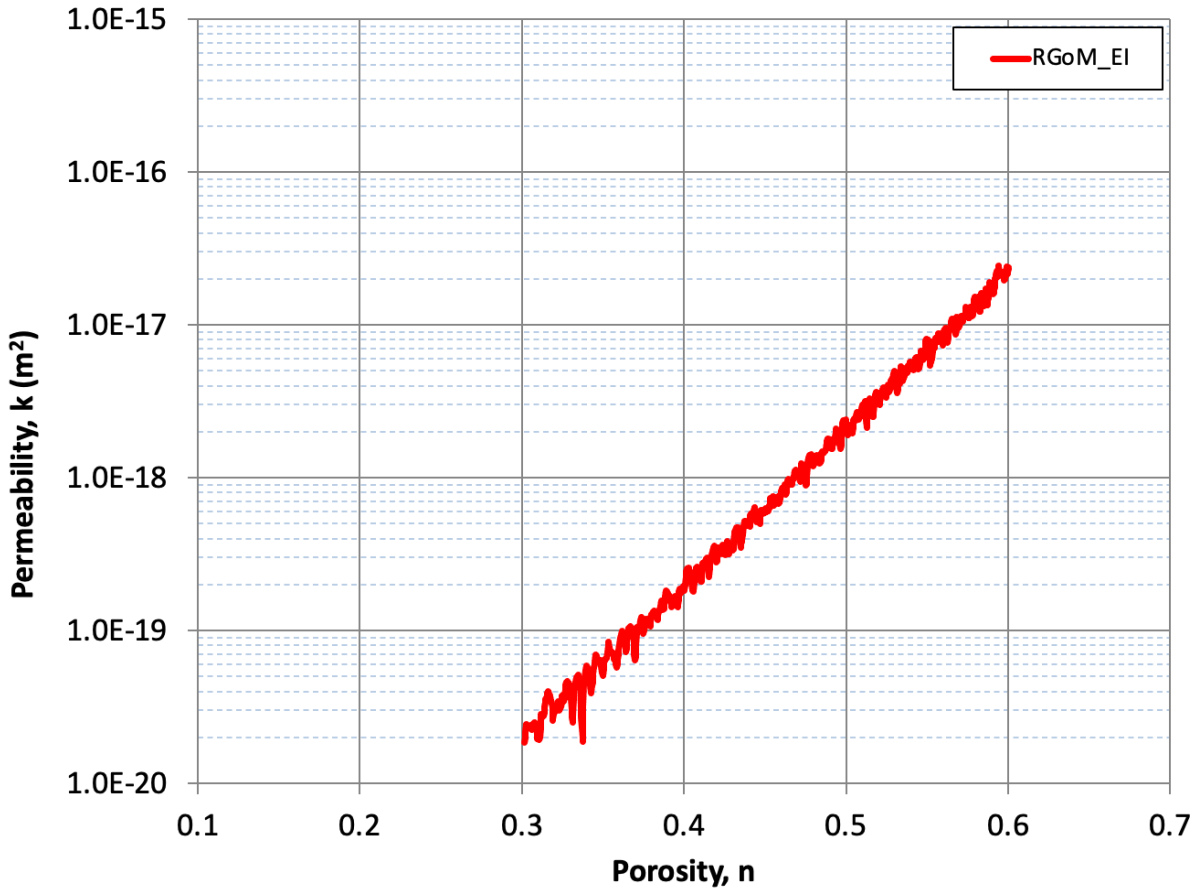

Figure 21. RGoM-EI exhibits permeabilities orders of magnitude lower than those in RBBC. Retrieved from UT GeoFluids Site on 8 June 2022.

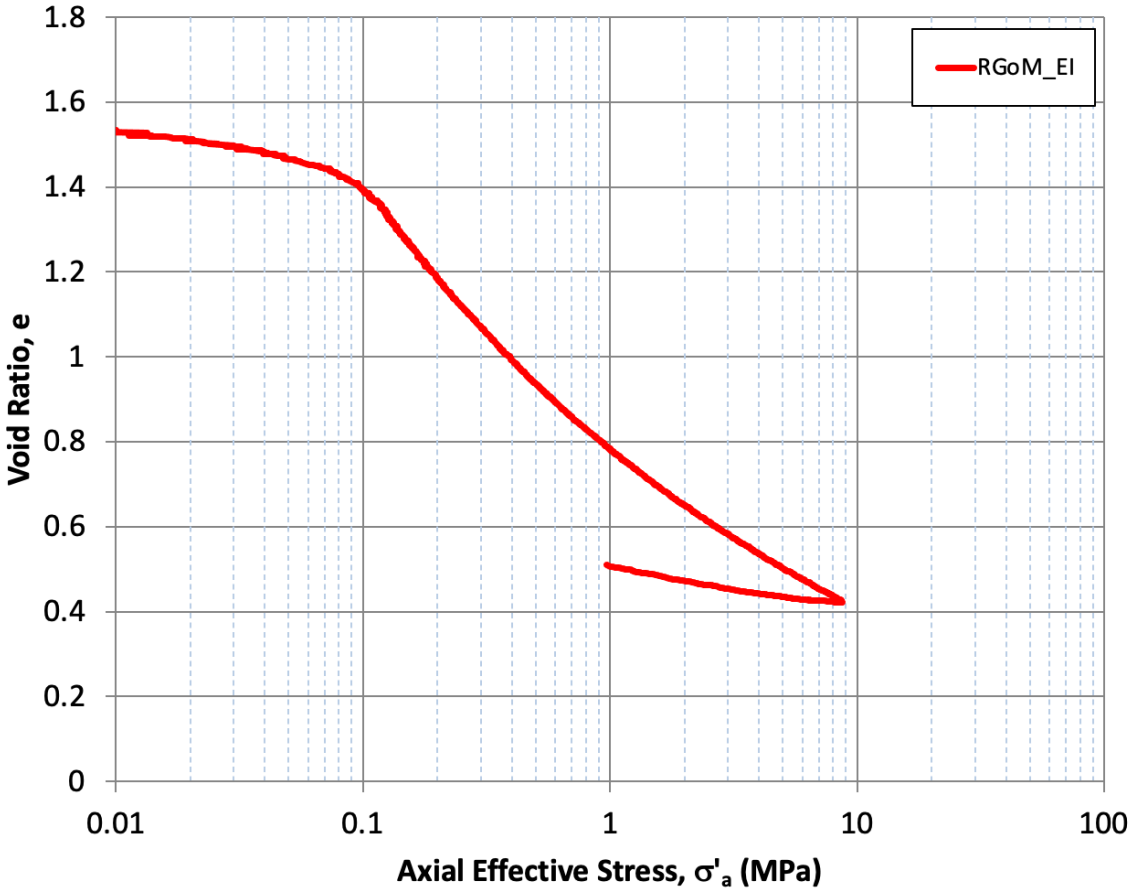

Figure 22. Compression curve of RGoM-EI Clay from a CRS test. It exhibits a concave upward shape in e – log σ'a space, making it challenging to choose an appropriate Cc value. Retrieved from UT GeoFluids Site on 8 June 2022.

Figure 23. X-ray image of intact Boston Blue Clay. Letters are spaced 1-inch apart and correspond to markings along the length of the steel tube. The sample quality of this section is superb, as the layers are completely horizontal and there are no rocks or cracks present. More damaged intact samples will show bent layers or large voids due to sampling. Sampled section for triaxial testing is about from markings D to G.

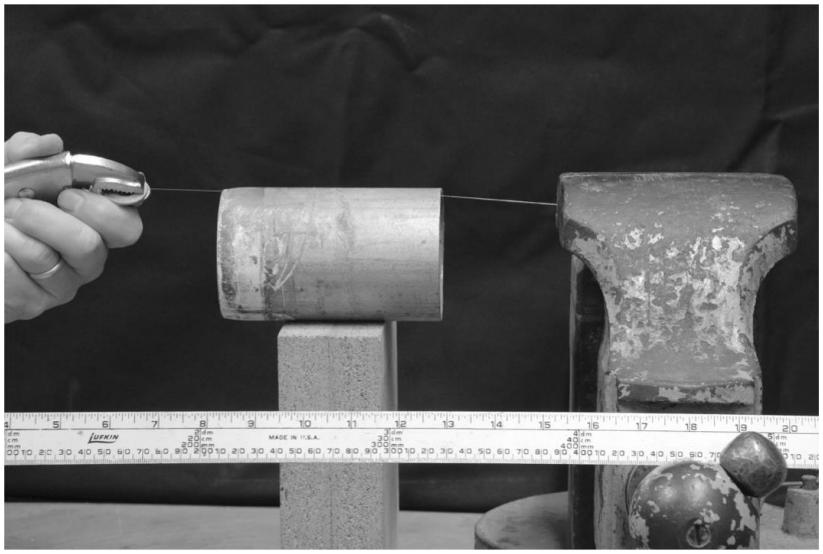

Figure 24. This is how the wire-clamp-plyer setup should look before the soil is ready to be freed from the inside of the steel pipe. Now one should hold the wire taught against the inside of the pipe while rotating to cut the bond between the soil and the pipe. Photo taken from Germaine and Germaine, 2009.

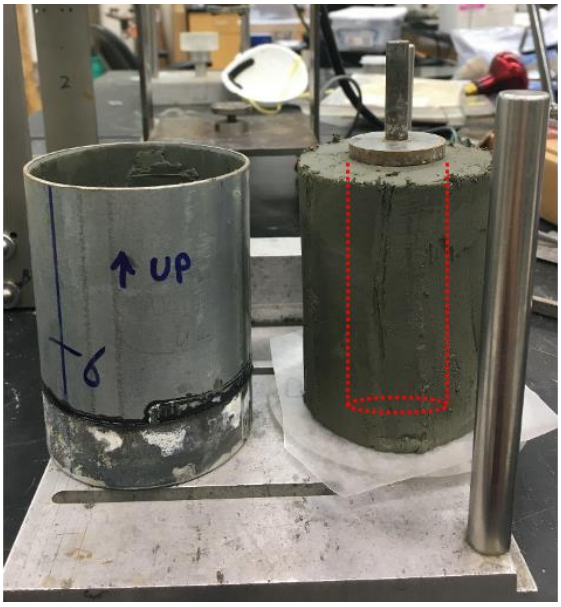

Figure 25. Image shows the intact clay cylinder after it has been extruded from the 3-inch tube. The dotted red lines on the right represent where the triaxial test specimen will be trimmed.

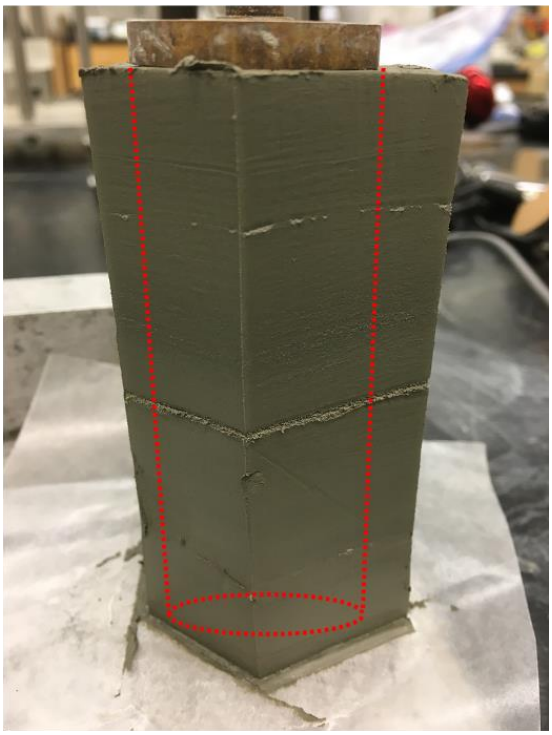

Figure 26. A rough trim is conducted to remove excess material from the 3-inch clay cylinder. The final diameter is going to be 1.4-inches so a substantial portion of clay can be removed. Some silt layers can be observed in this stage.

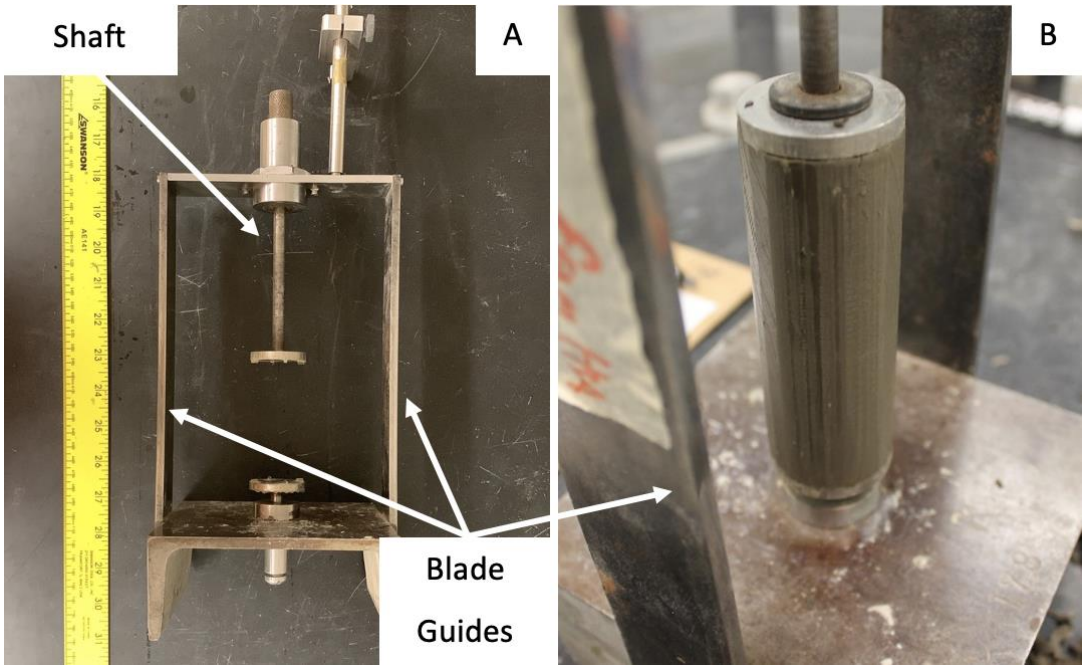

Figure 27. A) Miter box placed horizontally on the bench. B) Trimmed specimen in the miter box. A razor blade is dragged along the vertical guides as the specimen is rotated with the shaft. There are four little teeth on each pedestal to hold the specimen in place during trimming.

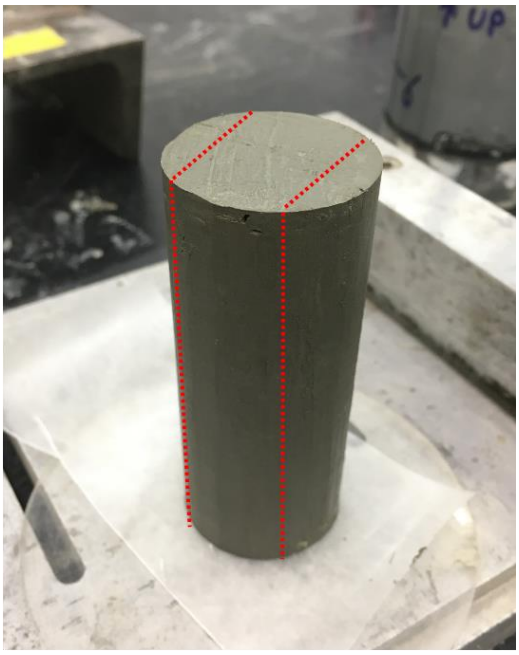

Figure 28. Shape of specimen after trimming in the miter box with a razor blade. Additional trimming is done on red dotted lines to make flat surfaces to mount the horizontal P and S-wave actuators.

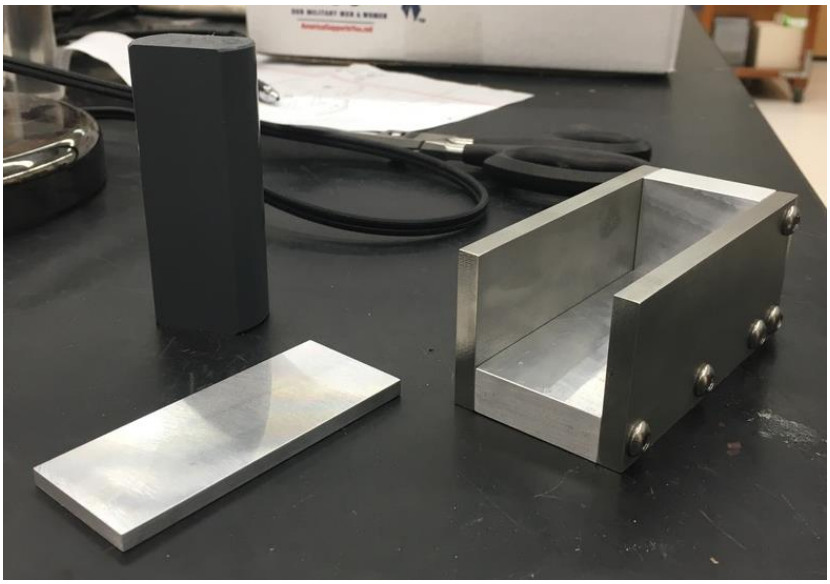

Figure 29. The miter box for the final two cuts. The top surface acts as the guides for the wire saw/razor blade. The first cut is made with the insert plate (left) removed, and the second cut has the plate inserted and the flat surface from the first cut placed face down on the insert.

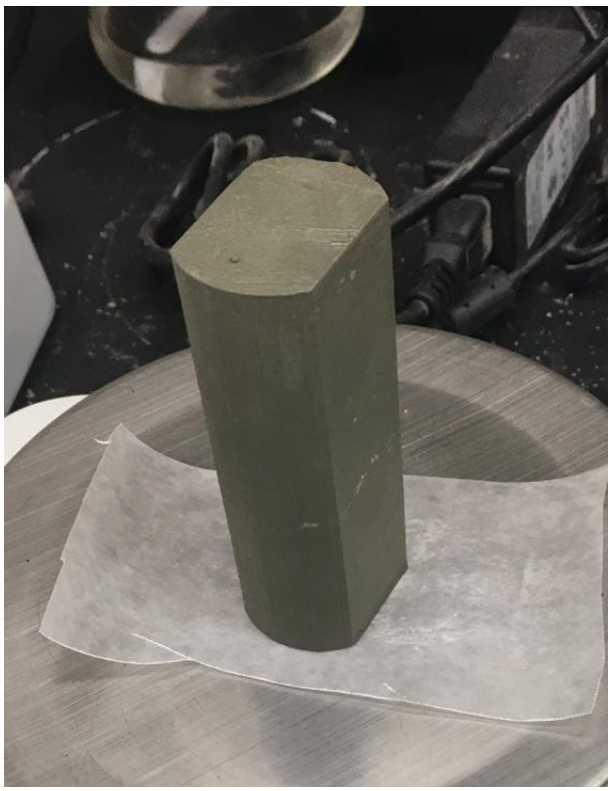

Figure 30. Final specimen Geometry.

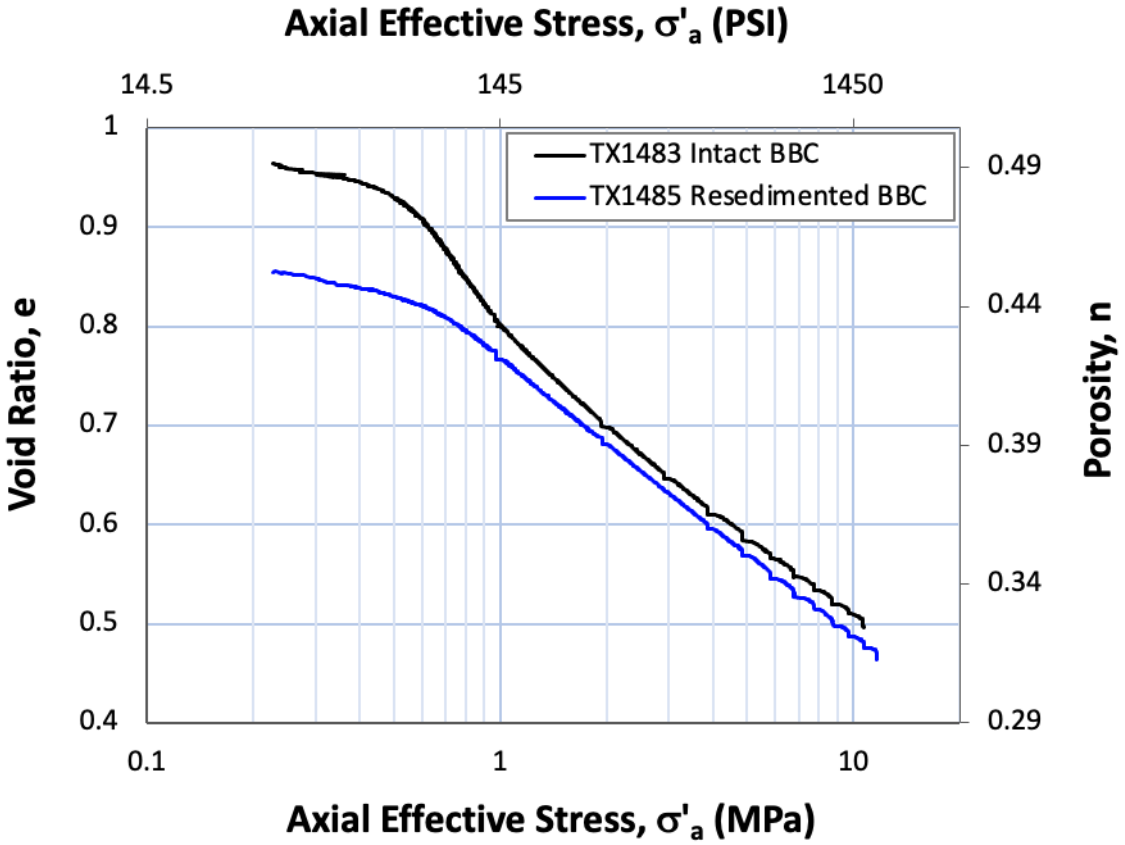

Figure 31. Intact (black) versus resedimented (blue) BBC compression curves are in good agreement. The intact compression curve shows effects of cementation, but after 1 MPa the compressibility behavior is similar. The little jagged edges are where loading was paused every 1 MPa for velocity measurements.

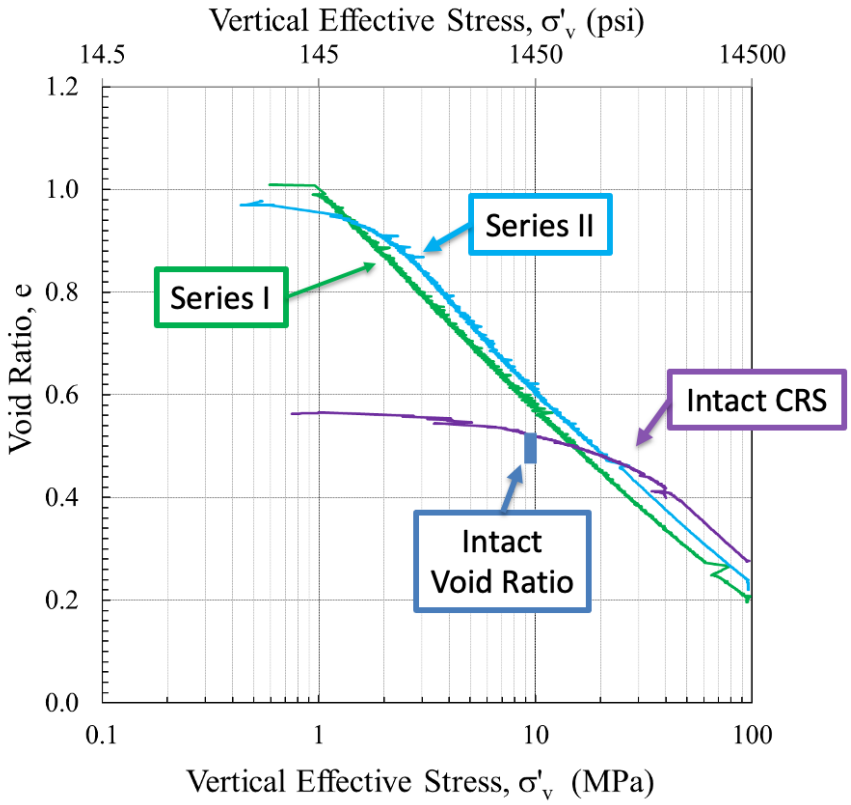

Figure 32. Difference between intact and resedimented Gulf of Guinea Clay from Finnegan, 2020.

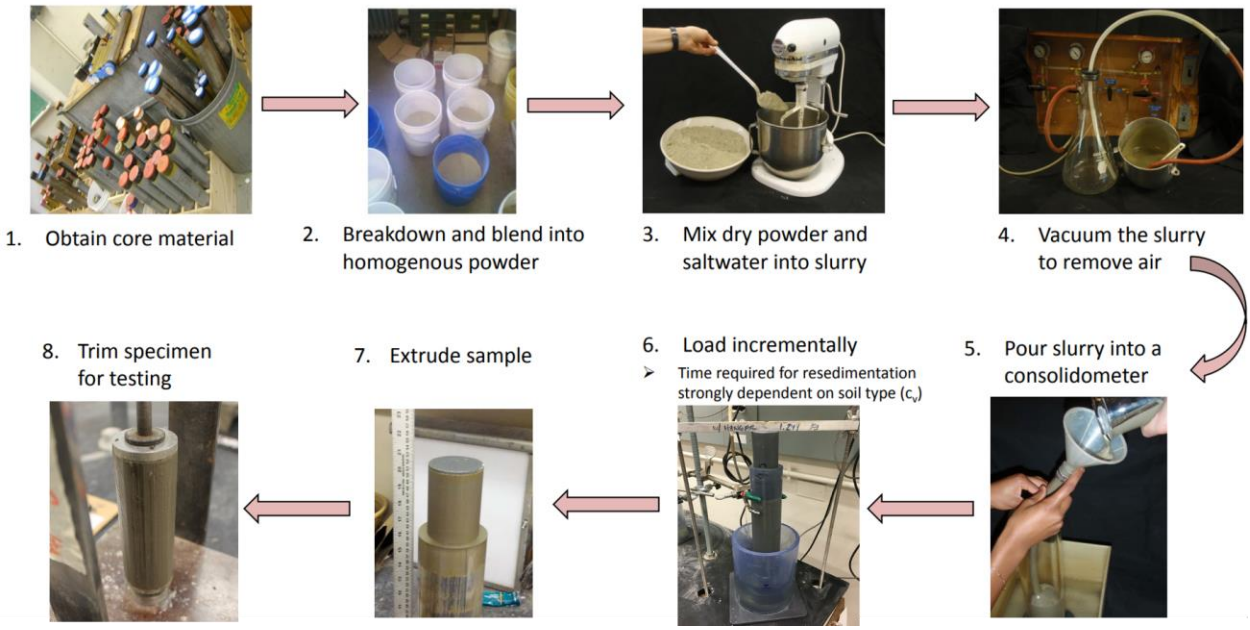

Figure 33. Resedimentation workflow from core material to specimen.

4 Laboratory Testing Equipment

4.1 Introduction to Laboratory Equipment

As mentioned previously in Chapter 1, this study has three main purposes: 1) Measure the velocity anisotropy of intact versus resedimented BBC, 2) Explore how stress path affects velocity anisotropy, 3) Study the sensitivity of P-wave velocity to shear stress during compression and undrained shear stress paths, and 4) Improve the wave pulse driver circuit technology to boost signal amplitude and eliminate sources of noise. This research is a continuation of research performed by Marjanovic and Ranjpour at MIT and Tufts respectively [19, 38]. For this study, a medium stress triaxial testing device with directional P and S-wave measurement capabilities was employed to carry out all tests. This chapter provides a detailed description of the velocity measurement system in section 4.2 and its circuitry in section 4.3, as well as the triaxial testing device itself in section 4.4.

4.2 Wave Propagation Technology

4.2.1 Introduction

The directional wave propagation technology used in this research was designed, fabricated, and calibrated at TAG Labs. The first iteration of the wave propagation technology was designed by Marjanovic at MIT and had the capability to measure wave velocities through soil specimens along a single (vertical) axis. Ranjpour at Tufts then modified this design to include horizontal actuators, allowing for horizontal and inclined velocity measurements. This study used both technologies and made modifications to the system for noise reduction.

4.2.2 Plate Actuators

Plate actuators, piezoelectric elements that respond to voltage with relative displacement, were used to send and receive waves through soil specimens.

Piezoelectric elements work because of the piezoelectric effect, which is the tendency of certain solid materials like crystals, ceramics, and biological matter like bone to accumulate electrical charge in response to applied mechanical stress. These materials change their static dimension when an electrical field is applied as well, forming the basis for the wave velocity measurement technology. This is known as the inverse piezoelectric effect.

The shear plates used in this research are the CSAP03 from Noliac, which provide a relatively large free stroke of 1.5 μm along the chamfered axis (10 mm x 10 mm x 0.5 mm) (Figure 34 a). This results in waves polarized perpendicular to their propagation direction. Horizontal S-waves are polarized along the horizontal axis and vertical S-waves are as well. These plate actuators have a relatively low capacitance of 3.321 nF, making them quick to charge/discharge even with low voltages or arrival wave amplitudes. The maximum/minimum operating voltage for this device is ± 320 V, so the + 23.4V pulse used to stimulate them is well within tolerance.

The P-wave piezoelectric actuators are the NAC2015, also produced by Noliac. These plate transducers are slightly thicker than the CSAP-03 (10 mm x 10 mm x 2 mm), and they lack chamfered edges as the directional component of the P-wave lies within the axis of propagation (Figure 34 b). The NAC2015 have a free stroke of 3.3 μm and a capacitance of 760 nF, both relatively large compared to the CSAP-03. Once again, the operating voltage is well within the tolerance of +150V.

4.2.3 Equipment Fabrication and Improvements

To minimize the necessary wires/pins and physical space taken up by the actuators within the triaxial cell, the P and S-wave piezoelectric plate actuators were stacked and epoxied before being mounted in the triaxial device. The stacking method was based on Marjanovic, 2016, where from top to bottom the stack was composed of a P-wave actuator, an insulating DuPont™ Kapton® sheet, a brass shim, an S-wave actuator, another brass shim, and a microscope glass coverslip (Figure 35) [38]. The

sandwiches were constructed using the following procedure: 1) Cut brass shims to 11 x 12 mm so that S-wave actuators fit on the shim but allow space for wires, 2) Solder 15 cm long wires onto brass shims—one wire of which is stripped of all insulating material, 3) Sandwich the S-wave actuator between the two brass shims using a very conservative quantity of conductive epoxy—if an electrical connection forms between the top and bottom brass shim the S-wave transducer will be rendered inoperable, 4) Apply pressure evenly to the sandwich using 400 g weights until epoxy cures, 5) Use Loctite E30-CL, a brittle, transparent, and stiff epoxy, to attach the Kapton sheet and P-wave actuator to the top of the sandwich from steps 1-4, 6) Similar to step 4, apply pressure evenly while epoxy cures, 7) Use the same epoxy to secure the glass slide to the bottom of the stack and apply pressure as it cures, 8) Bend and solder the stripped ground wire from the S-wave actuator to the ground of the P-wave actuator, 9) Apply a couple layers of Loctite E30-CL epoxy to the exposed ground wire and P-wave actuator to provide electrical insulation, and 10) Test the insulation with a multimeter set to audible resistance measurement mode and apply more epoxy as needed. Any exposed conductive surfaces can become sources of electrical crosstalk and therefore signal noise. The completed stack is shown in Figure 36. Once the stacks are constructed, they are embedded in the top and bottom caps using the same Loctite E30-CL epoxy (Figure 36) or used as-is to for the horizontal actuators. The final configuration requires two pairs of two opposing actuators, as shown in Figure 37.

A source of error that has now been fixed was the caulking used to route the horizontal actuator wires through the membrane. This method, while viable for several tests between re-caulkings, resulted in internal leak issues and therefore unreliable void ratios. Silicone oil from the cell would eventually find pathways along the wires to infiltrate the caulk. These leaks can impact compression curves and radial strains, leading to potential errors in horizontal and inclined velocities. The author rectified this issue by machining holes in the brass bottom cap, routing the wires through them, and filling them with Loctite E30-CL epoxy. This had the

additional benefit of eliminating more noise from the received signal due to the 9-pin connector.

4.3 Driver Circuit and Electronics

4.3.1 Introduction

The circuitry used to drive the piezoelectric actuators during this research was designed and produced by Dr. Germaine and Dr. Ranjpour at TAG Labs, and is discussed in more detail in Ranjpour, 2020 [19]. There are only a few devices necessary to produce and view the amplified square wave used to drive the actuators and the received signals. These devices are: 1) A function generator to output a 5 V square wave, 2) An integrated circuit (IC)/switch box to amplify the 5 V signal to 23.6 V and route the signal to and from the actuators, and 3) An oscilloscope to view the input and output signals. The circuit design is discussed in this section, as well as the improvements made to the circuit and signal.

4.3.2 Circuit Design and Improvements

The function generator used in this research is a B&K Precision 3003 Function Generator (Figure 38). It can produce 10 MHz waveforms with 0.02% frequency accuracy and has a 0.1 Hz frequency resolution. Its output signal ranges from -5 to +5 V, and in this research a square wave from 0 – 5 V is utilized. Square waves were chosen because they stimulate the actuators as fast as possible, producing a high amplitude wave that elicits a sharp first arrival peak. The duty cycle of the square wave used is 20 Hz for this research, rather than the 115 Hz chosen in Ranjpour, 2020, because the longer duty cycle gives the actuators enough time to fully drain stored electricity. At 115 Hz, the larger capacitance P-wave actuators still have about 7 V stored by the time they are stimulated with the next 23.6 V pulse, so the effective range of the input voltage is only 16.6 V. By using a 20 Hz pulse the actuator fully

drains, so the full range of 23.6 V is available (Figure 39). The output signal showed a roughly 40% improvement with the 20 Hz input signal (Figure 40).

The circuit box used to amplify the signal is made of aluminum which acts as a Faraday cage to block electromagnetic interference and houses a basic amplifier circuit and rotary switch to connect the circuit to the appropriate piezoelectric actuator with ease. A schematic can be seen in Figure 41 and a photograph in Figure 42. It uses two ICs and a 23.6 V power supply to amplify the 5 V signal from the function generator to 23.6 V. IC1, as seen in Figure 41, is an operational amplifier called the LT1210-CT7. Its purpose is to amplify the function generator signal to the voltage provided by the power supply. IC2 is an ultrafast MOSFET gate called the IXDD 614PI. It is the powerhouse of the circuit, capable of sourcing a 14A peak current in 25 – 35 nanoseconds. It serves the same purpose as the IC1 but provides more current. After experimentation, it was found that the 614PI alone can drive the circuit with no changes in the amplified signal. Thus, the circuitry can be simplified, and extra costs eliminated.

The oscilloscope used to collect the input/output signal data for this research was the Tektronix TBS1072B-EDU Digital Oscilloscope (Figure 43). The oscilloscope's trigger function was used to "freeze" the screen to the rise in the input (actuator power) voltage, allowing that rise to be used as a time reference to compare the output (return signal that travelled through the specimen). Another setting was used to average the signals, so the signals on screen are an average of the previous 128. This oscilloscope conveniently has a USB port for direct data storage and all velocity readings were conducted manually.

Significant improvements were made to the horizontal received signal as well. If one looks closely at the bottom of Figure 42, all the grounds from the coaxial cables are tied together. This has a significant impact on the ground stability, though the reasons remain up for debate. One hypothesis is that it is due to a phenomenon called ground bounce. Ground bounce is a type of noise that occurs during transistor (the 'T' in MOSFET) switching, when the ground on the IC and in the rest of the circuit are

different [39]. It occurs because of the parasitic inductance, capacitance, and resistance of wires, pins, and connections attached to the MOSFET IC, where inductance is the tendency of an electrical conductor to oppose a change in the electric current flowing through it. The instant logic level input to the IC changes (0 to 5 V or vice versa), there is resistance to this change left in the system's electromagnetic field, leading to oscillations in the ground signal. The oscillations in the ground reference can cause disruptions to other parts of the circuit besides the IC as well, and disruptions to the input signal itself due to positive feedback can occur. This theory remains most plausible because the noise was eliminated when the horizontal actuator ground was isolated by passing it through the brass bottom cap (Figure 44). Loops in the ground rather than branches appeared to be exacerbating this problem as well. What is clear, however, is that the horizontal P-wave first arrival has improved due to these changes.

4.4 Medium Pressure Triaxial System

4.4.1 Introduction

All triaxial tests in this research were performed using a TAG Labs medium pressure triaxial testing device (Figure 45). The medium stress device is a computer automated triaxial device used to test soils up to 10 MPa cell pressure capacity. The device used in this research was developed by Anderson [40] to test the engineering properties of frozen sands, and was later adapted by Abdulhadi [24] to test fine-grained soils. This device uses three hydraulic pistons filled with different fluids to regulate pressure to a hydraulic load jack for the axial load, the cell pressure, and pore/back pressure. These pistons are referred to as Pressure Volume Actuators (PVAs). The motors running the PVAs are run by Maxon ESCON controllers powered by a 50V DC power supply. A custom designed Strawberrytree A to D converter supplies the command voltage from the PC to the motor controllers. This PC receives signals from several transducers (axial strain, axial load, volumetric strain, cell pressure, and back pressure) through a custom AD1170-based analog to digital converter (ADC) and uses

these signals to in turn control the PVA motors. Thus, a computer-controlled feedback loop is complete, and the soil system can be controlled by QuickBASIC algorithms on the computer. All data readings from each transducer are collected by a central data acquisition system (DAQ).

4.4.2 Transducers

There are three types of transducers (besides the velocity actuators) used during triaxial testing. These are Linear Voltage Displacement Transducers (LVDTs), pressure transducers, and load cells. This section will cover information regarding each model used in this research.

Two Transtek Inc. LVDTs are used in the system to measure: 1) Axial deformation of the specimen, and 2) Volumetric strain by measuring displacement of the back pressure PVA piston (Figure 46). LVDTs consist of a ferromagnetic core that moves inside a tube composed of three solenoidal coils. As the core moves, the voltage produced by the device changes based on the relative displacement from the zero position of the device. LVDTs allow us to measure displacements on the order of microns, are low hysteresis, frictionless, and have a high linear range. The LVDTs used in this research have a 5 V DC linear range (-2.5 to +2.5 V) and can measure maximum deformations of one inch for the axial strain and two inches for the volumetric strain LVDT. The author calibrated these devices using a micrometer and the DAQ and the device was used with a 5 V DC input voltage.

The load cell used in this research is a Data Instruments JP-1000—a 1000 lb (~454 kg) capacity load cell. These load cells are no longer in production, although this model is favored due to it being able to easily fit inside the triaxial cell (Figure 47). The benefits of having an internal load cell are that frictional effects caused by the gasket seal on the piston can be ignored, and the self-weight of the piston can be minimized.

Omega™ PX-102 flush diaphragm pressure transducers are used to measure the cell pressure and the pore/back pressure (Figure 48). These pressure transducers have a 1000 PSI capacity (70.3 KSC), an input voltage range of 5 – 6 V with a 100-mV output, and only deviate 0.25% from the best-fit straight line (BSFL). They are capable of withstanding over 160 million load cycles, making them extremely robust measurement devices. This is reflected in the nearly constant calibration factor recorded by multiple students over the years.

4.4.3 Pressure Volume Actuators

As mentioned earlier, axial load, cell pressure, and back/pore pressure are controlled by PVAs. These wall mounted PVAs have a pressure capacity of 14 MPa and a volume capacity of 47 cm^3. A 0.5 tone Duff-Norton inverted ball-screw jack is driven by a Maxon Motors continuous output servomotor (with 80 mNm of torque geared at 100:1). This screw jack pushes a 2.85 cm^2 constant cross-sectional area piston upwards into the hydraulic chamber of the PVA (

Figure 49). This constant area allows for volume change to be computed since displacement of the piston is measured.

For the axial PVA, the hydraulic pressure generated in the PVA pushes a jack, which in turn drives the base pedestal upwards against a stationary crossbar. The stationary crossbar has a 10-ton capacity. The pressure is transmitted to the specimen through the hardened steel piston with the internal load cell attached (Figure 47). This PVA contains regular hydraulic oil.

In addition to the axial load PVA, two other PVAs are used to regulate cell pressure and pore pressure. These PVAs are filled with 20 centistokes silicone oil (Dow-Corning "200 fluid") and salt-water respectively. Silicone oil is used in the cell because it has a nearly nonexistent osmotic leakage potential through the membrane [41]. It also is non-conductive, which allows for electronics like the load cell and velocity

actuators to be used within the cell. The salinity of the pore PVA is adjusted for each test to match that of the resedimented specimen. It should be noted, however, that the gaskets between the piston and chamber on the PVAs can fail if debris is drawn into the PVA during unloading. It is therefore critical to filter cell fluid before it is put into the PVA if it contains visible particulates.

4.4.4 DC Motor Controllers

The custom-made motor control box was designed and manufactured at TAG Labs by Dr. Germaine. The box houses three Maxon Motor ESCON 50/5 servo controllers, an AC to DC power supply, a control card, and a fan (Figure 50). A pulse width modulated signal is used by the servo controllers to control the motors. Tachometers measure the speed of the motor, and by changing the gain and output on the servo controllers using a USB interface and the ESCON software one can make the motor move more even with the same control voltage coming from the PC. This can be especially useful, as the gear ratio is hard to manually change as significant disassembly of the PVA motor housing is required. Another way to change the gain of the motors is to add a voltage divider to the tachometer and ground, which can be done by the motor or in the box itself. The box also houses electronics to control the limit switches and manual switches on the outside.

4.4.5 Data Acquisition System

In addition to the local data from the PC controlling the test, high precision data from the pressure transducers, LVDTs, and load cell are necessary for data analysis. A Hewlett Packard HP3497-based central data acquisition system (DAQ) is used for this process. The central DAQ is an auto-ranging, low-noise dual slope integrating A/D converter. With the expansion unit it has 200 channels, meaning that 200 transducers can be monitored in the lab simultaneously. A custom-built software program called Windap allows one to use a Windows PC to set up data recording tasks

with the channels of choice, desired reading interval, and total number of readings. It also allows one to save data, take manual readings, and retire tasks as necessary. The author took manual readings for each velocity measurement so that all soil engineering properties could be known with precision at the time of velocity measurement. It is important to take note of the reading number on the screen, as finding the exact line of data when you took a velocity measurement can be tedious without that information.

4.4.6 Data Analysis

After running a test and collecting the .dat file from the central DAQ, one can analyze it using innumerable methods. The simplest is to set up an Excel file with the calibration factors of each transducer and functions in place to calculate each engineering parameter of interest. However, even the most organized Excel sheet leaves room for error. For this reason, all final data reduction was performed using the QuickBASIC triaxial test data reduction code created by Dr. Germaine and his students. This program takes the specimen measurements, channels, normalized zero voltages, calibration factors, and raw data and outputs all factors of interest. Although there remains the chance a number could be inputted incorrectly, it greatly diminishes the probability of a calculation error. The author altered the program to correct for the apparatus compressibility of the device. This program helped streamline and increase the accuracy of the data reduction process.

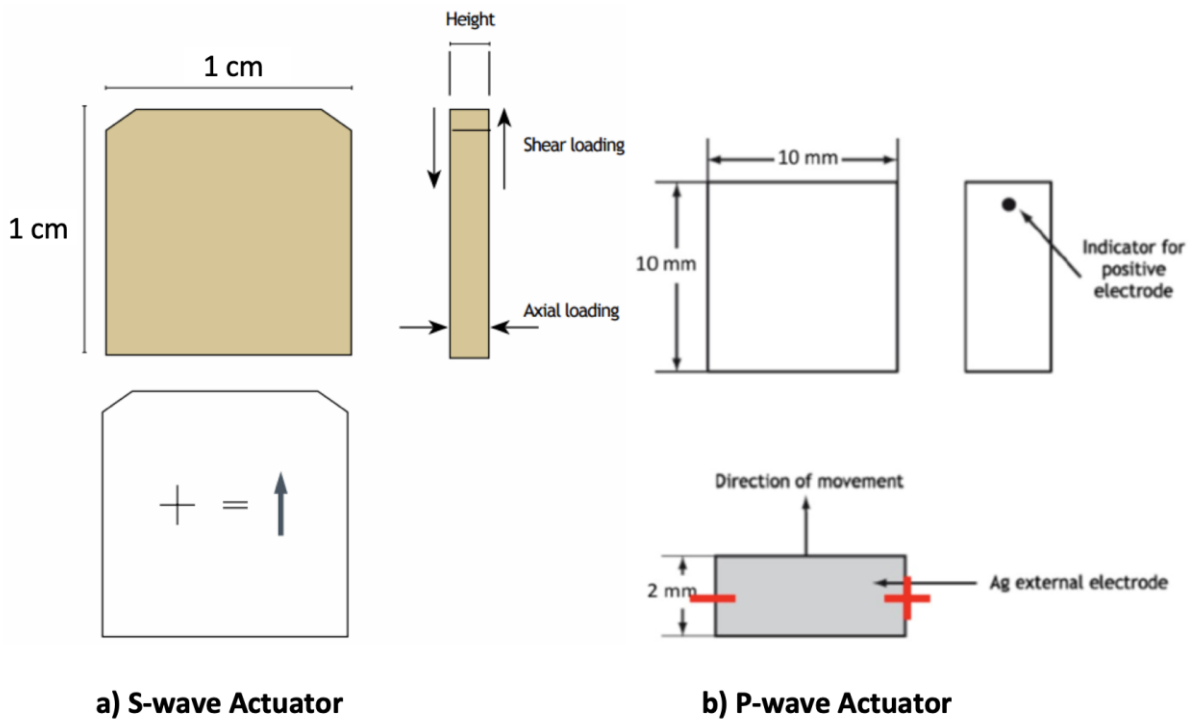

Figure 34. Schematic of the Noliac a) CSAP03 shear plate and b) NAC2015 actuator.

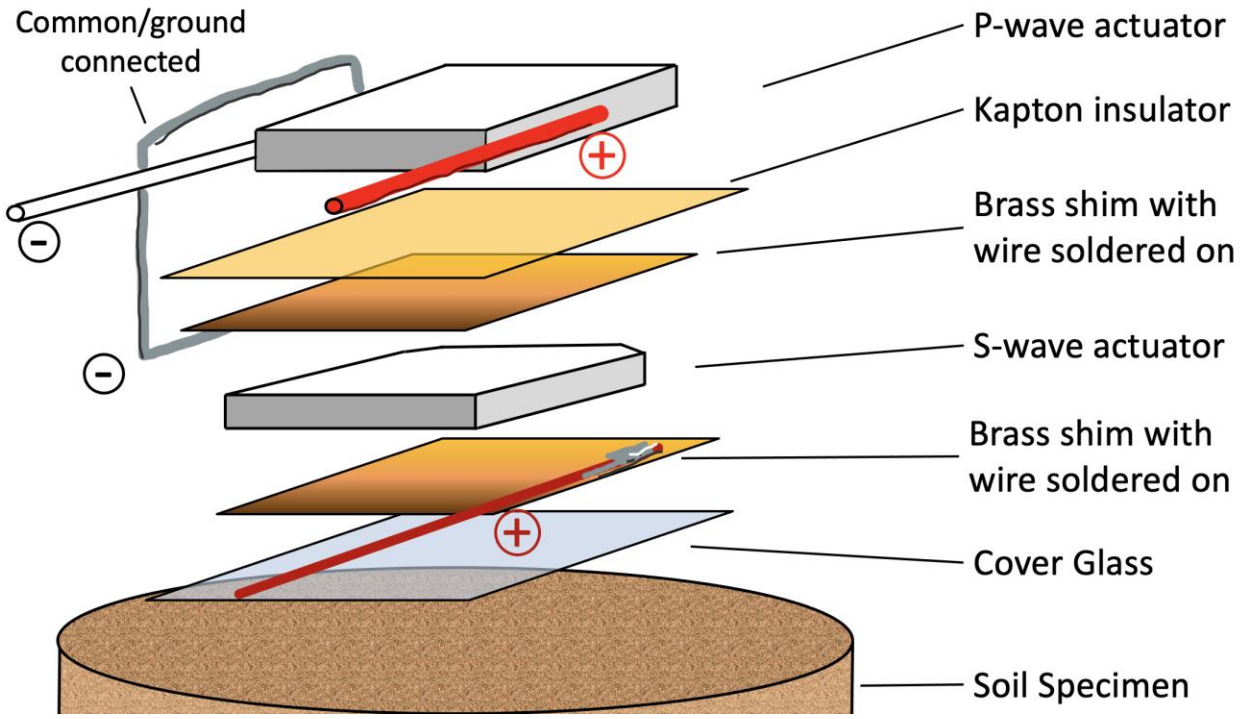

Figure 35. Breakdown of the piezo actuator stack with marked voltage signs. The stack is held together by various conductive and insulating epoxies.

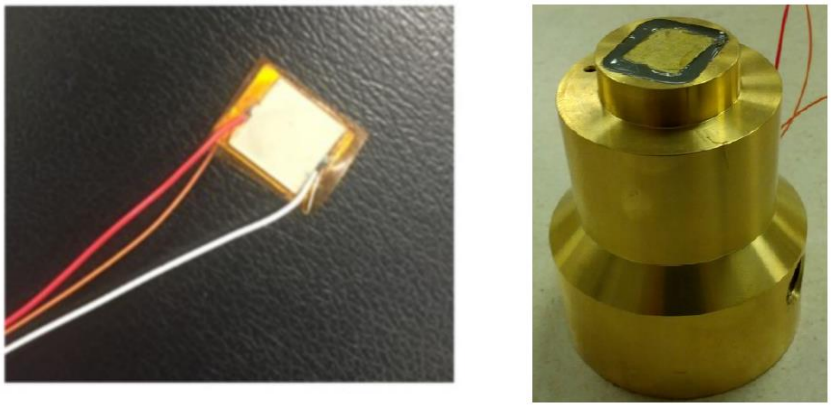

Figure 36. The completed piezo sandwich is shown on the left, where the red and orange wires power the P and S-wave actuators, respectively. The clear yellow material is the Kapton. A custom end cap (top cap) is shown on the right. Donut-shaped porous stones fit onto top and bottom caps, allowing drainage of pore fluid from specimen.

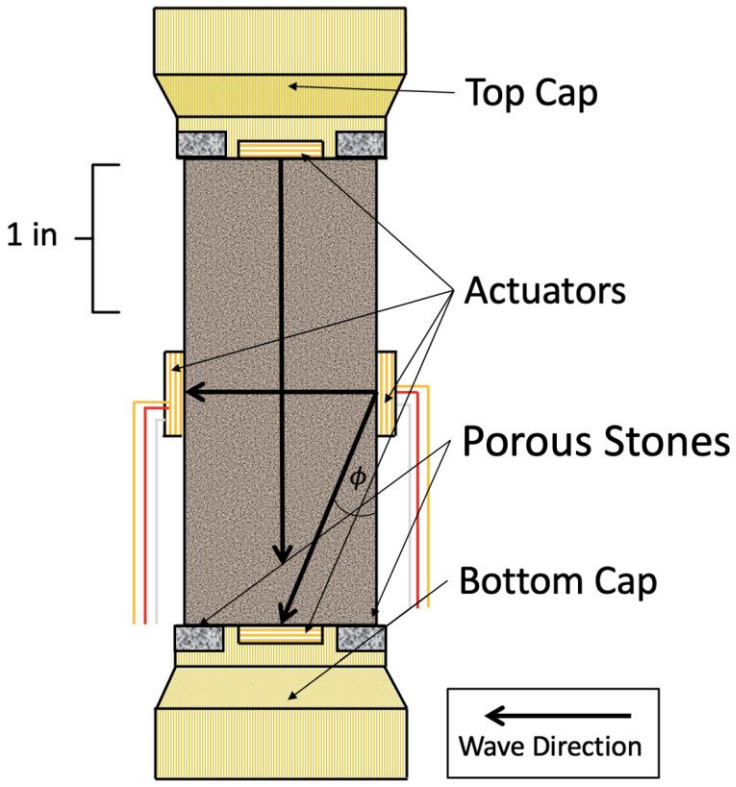

Figure 37. Diagram of all actuators mounted on a specimen. Wave propagation directions are shown with bold black arrows.

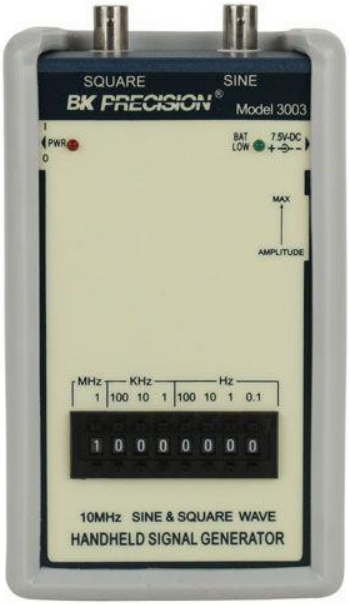

Figure 38. Signal generator generates the 5 V square wave used to drive piezoelectric actuators.

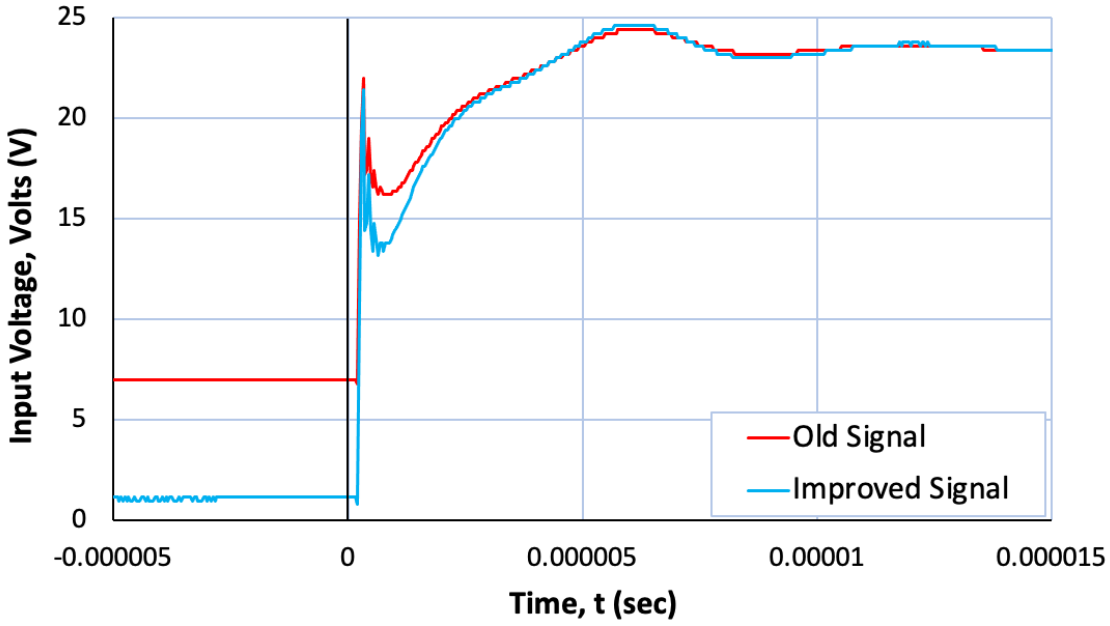

Figure 39. Improvements made in range of input signal after transition of 115 Hz (Red) to 20 Hz (Blue). Voltage fluctuations after initial spike are speculated to be due to imperfections in ICs and ground instability.

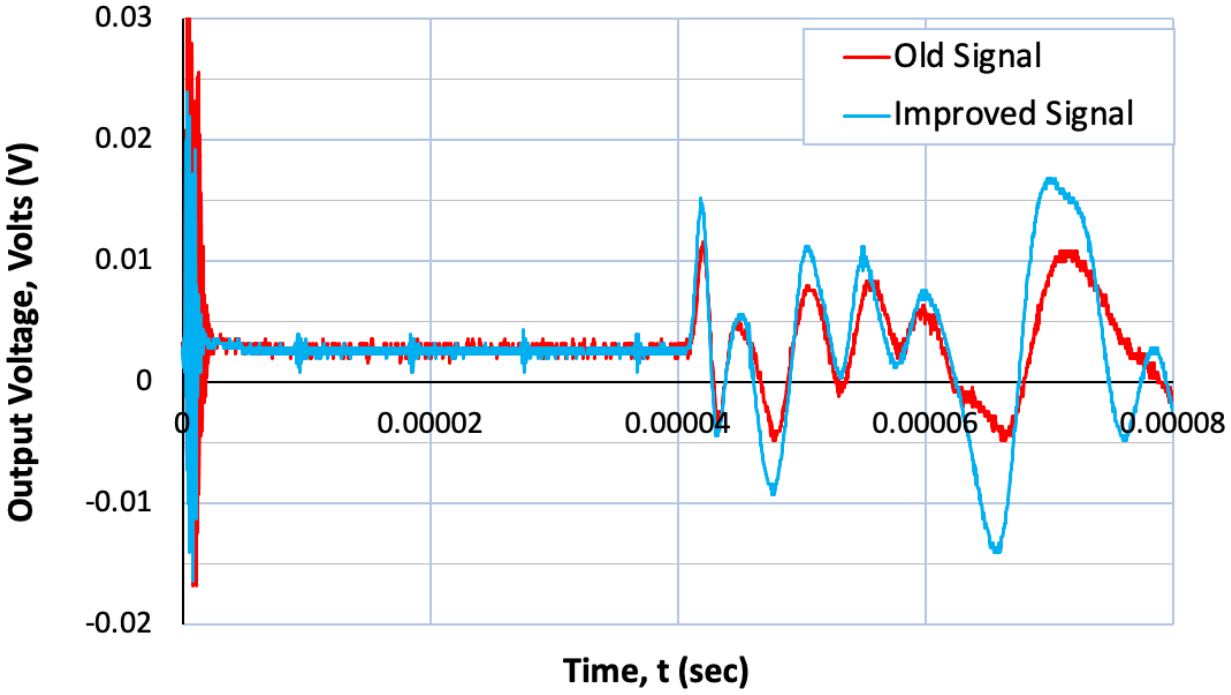

Figure 40. Output signal amplitude (first peak) improved 40% from using the full voltage range (blue) versus about two-thirds the range (red).

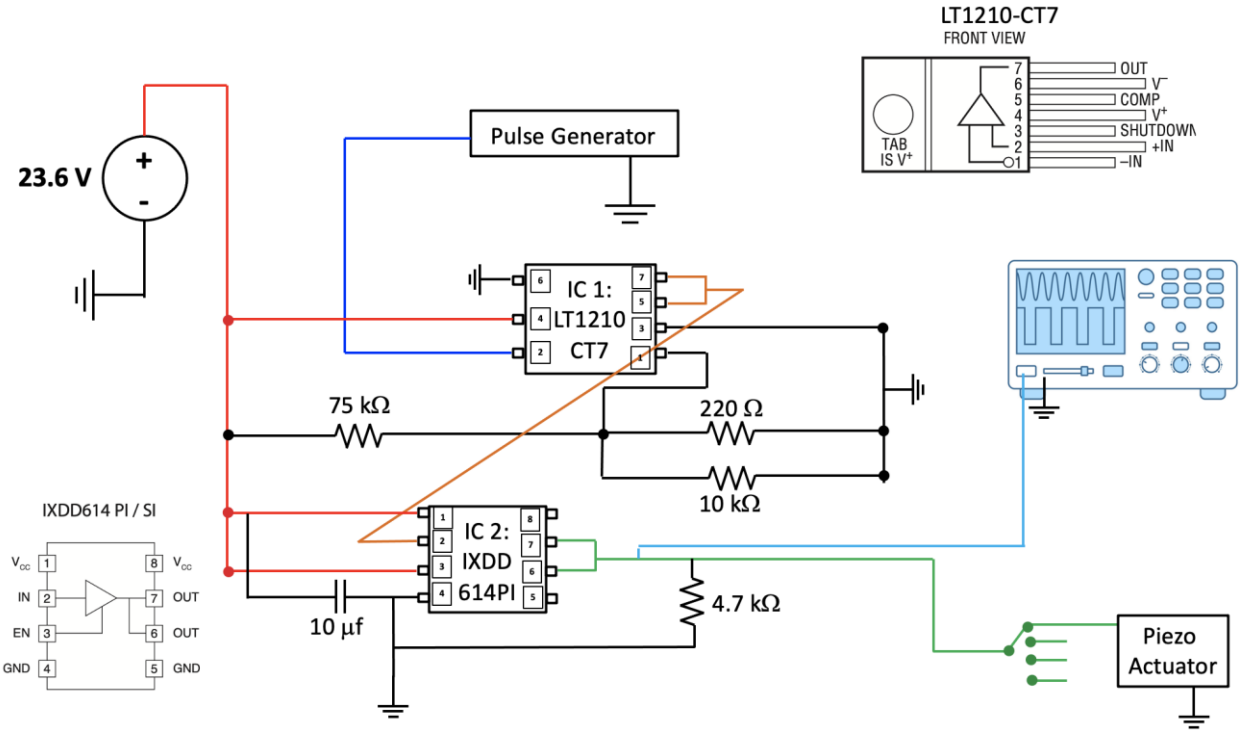

Figure 41. Circuit diagram of the driver system. The physical box contains the two ICs and a rotary switch for switching between actuators.

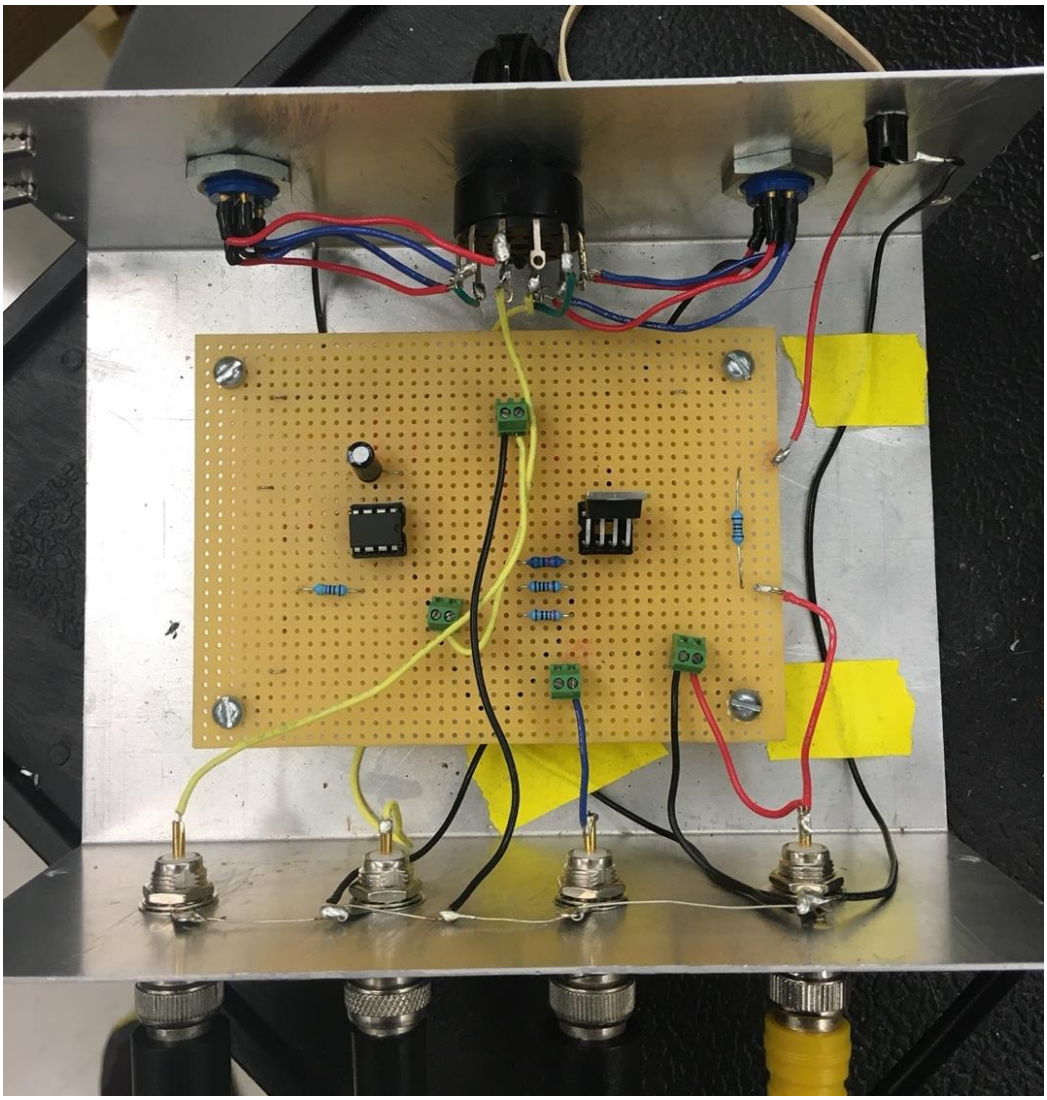

Figure 42. Photograph of IC/switch box. The IC on the left is the MOSFET amplifier and the one on the right is the Op Amp. The upper left 5-pin connector is for the input voltage to the actuators while the one on the right is for the received signal. The four coaxial cable connections on the bottom of the photo from the left are for the input to oscilloscope, output to oscilloscope, function generator signal to IC1, and 23.6 V power supply to the circuit.

Figure 43. Photo of oscilloscope used in this research.

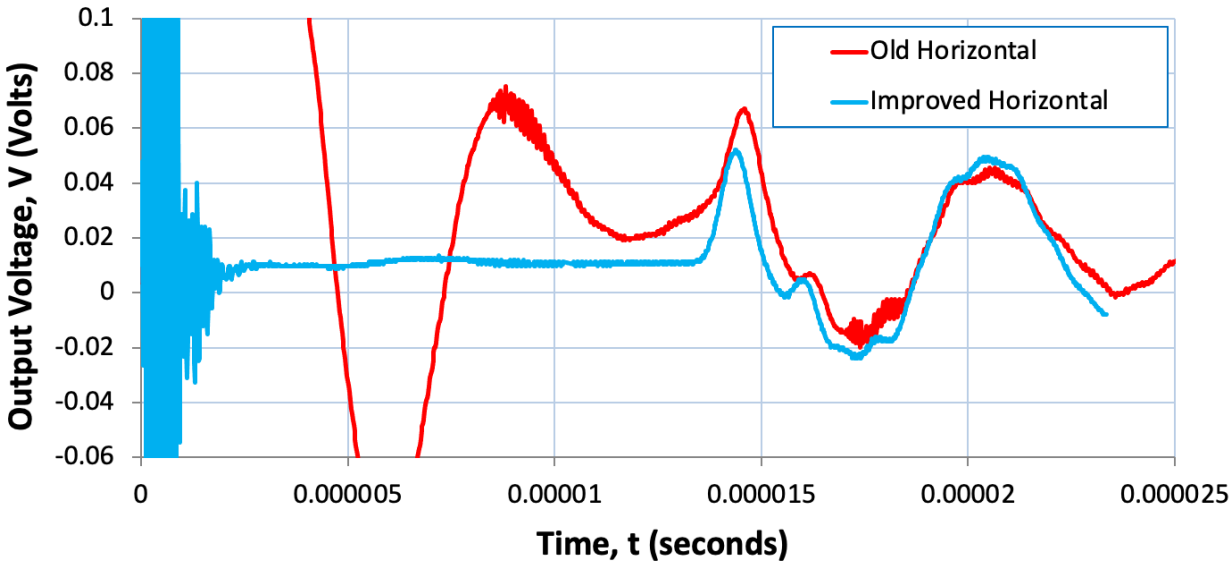

Figure 44. Signal difference between new (Blue) and old (Red) horizontal output signals is shown. The new signal shows a sharp first arrival which was not clear in the old signal.

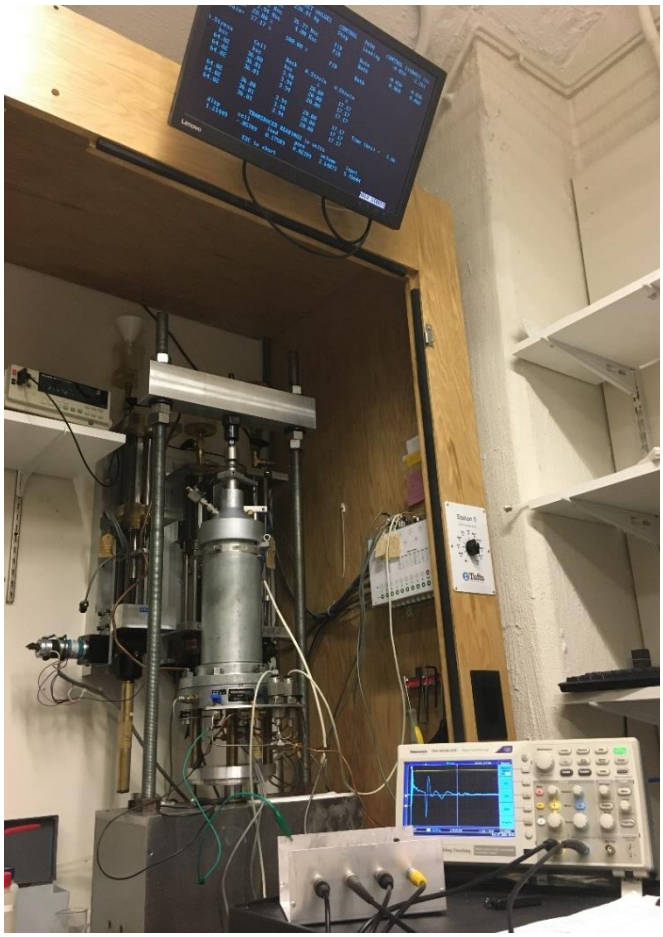

Figure 45. Photo of medium stress triaxial device. The three PVAs are wall-mounted and can be seen behind the device. The oscilloscope in the foreground is recording a horizontal S-wave.

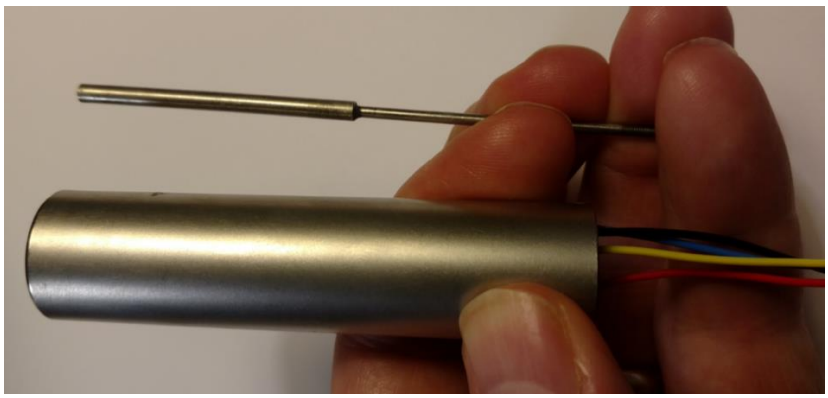

Figure 46. LVDT. The core sliding in the tube produces a DC voltage change proportional to displacement in the linear range. Photo from Dr. Germaine's CEE 244 Course notes.

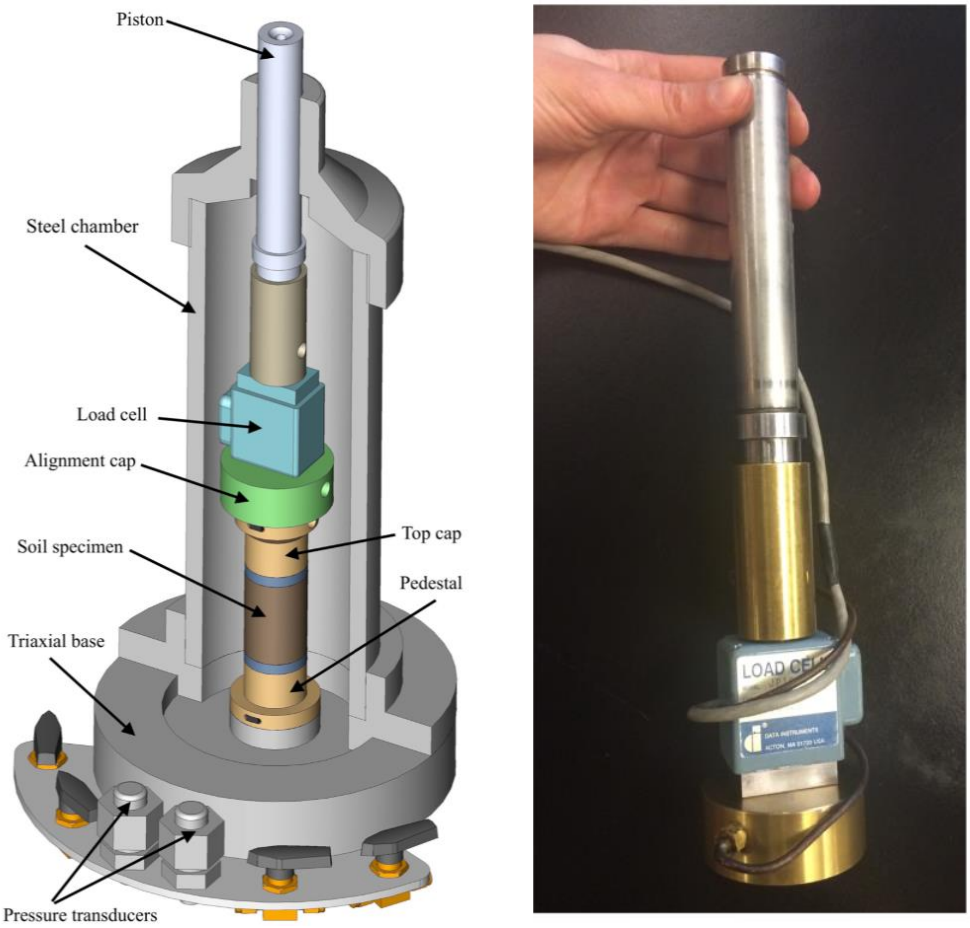

Figure 47. Cross section of the triaxial cell (left) shows the internal components. The piston setup can be seen on the right, where the load cell is nearly in direct contact with the specimen.

Figure 48. Photo of a PX-102 1000 PSI pressure transducer from manufacturer.

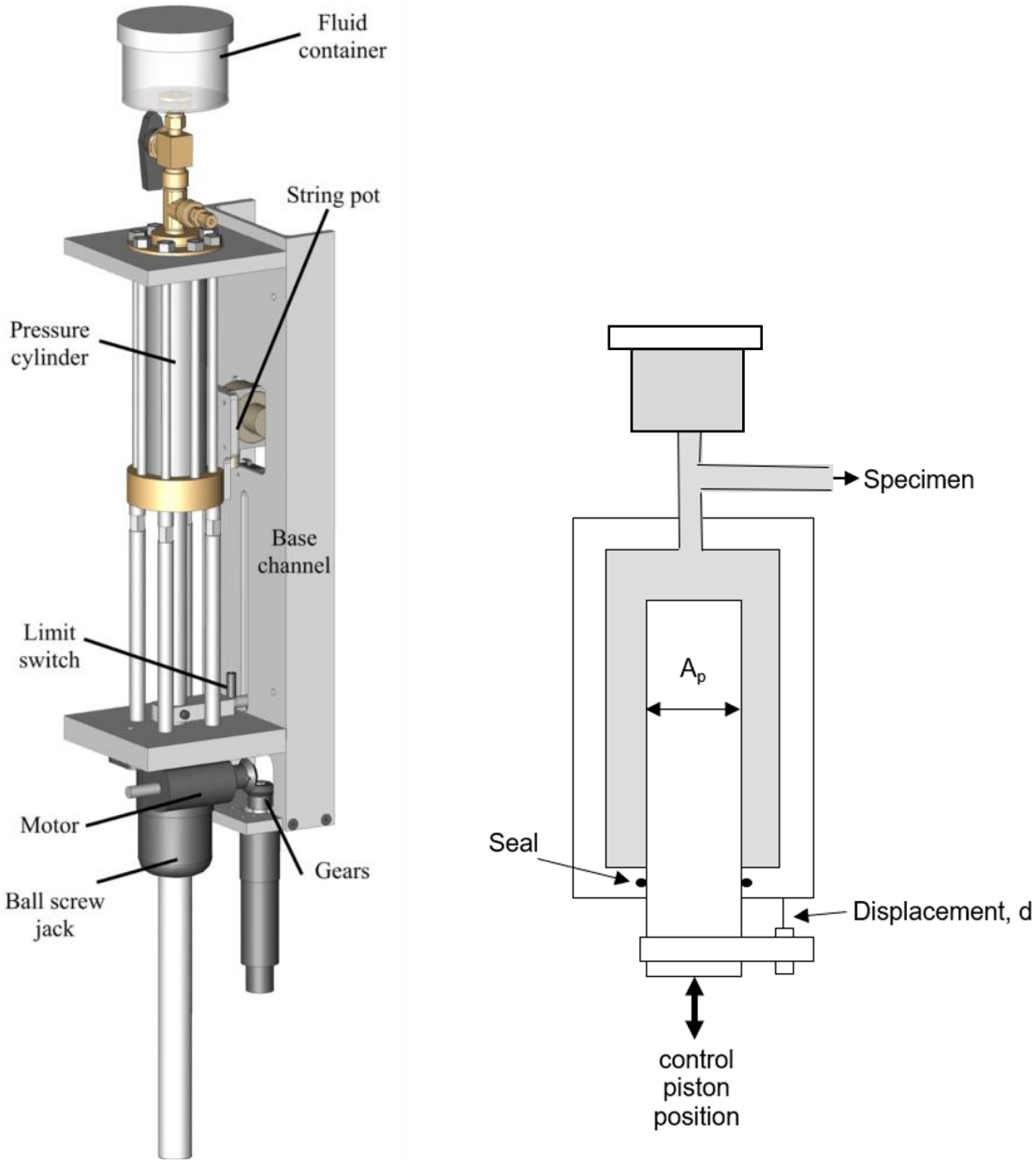

Figure 49. PVA schematic (left). A cross section of the pressure cylinder is shown on the right (image from Dr. Germaine's CEE 244 Course Notes).

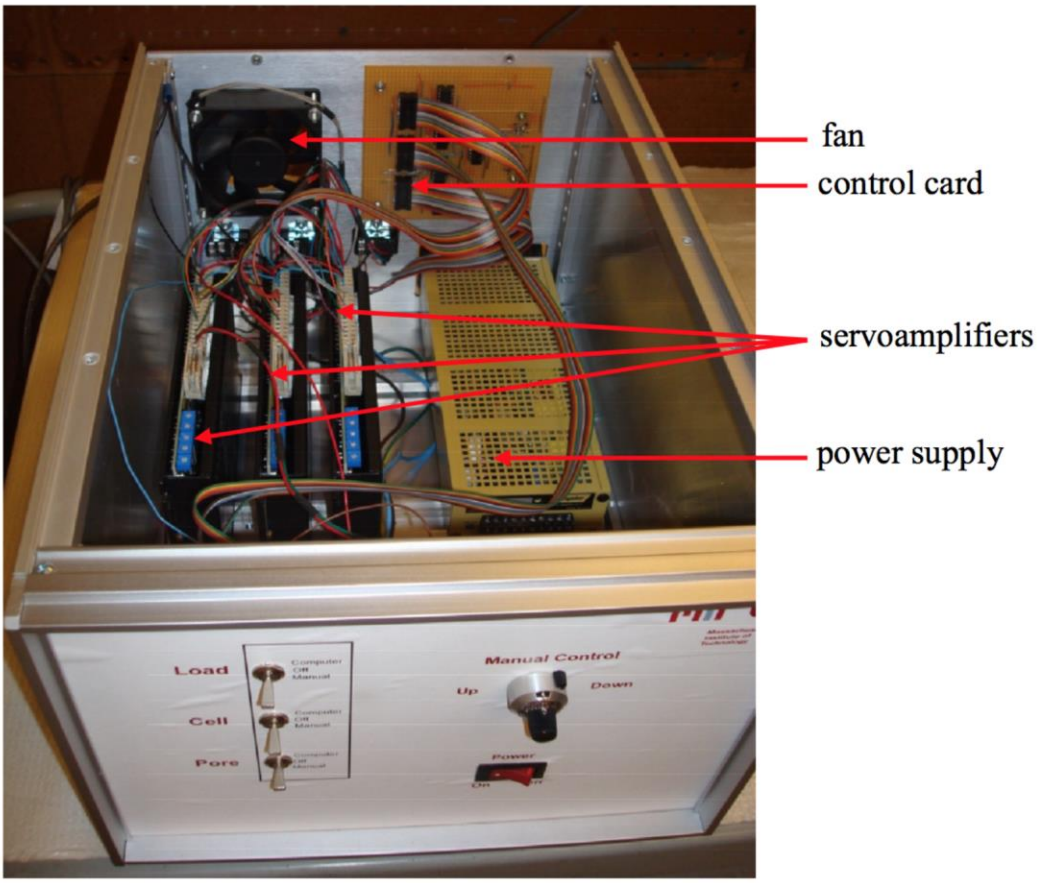

Figure 50. Photograph of motor control box. Manual switches are on the front of the box.

5 Research Methodology

5.1 Introduction

This chapter aims to codify the processes used to conduct triaxial tests during this research. Having a set of guiding principles and key steps in mind during the process can greatly improve the chances of success, thus maximizing the quality of data produced. The details of triaxial test setup are discussed first from start to finish. This is arguably the most critical phase of research, as minor errors in parameters like the height of the specimen or wet mass can have cascading impacts on the compression curve, anisotropy, and the velocity – effective stress relationship.

Next, the equally laborious process of signal collection and processing is covered. This covers topics like selecting the appropriate arrival time and factors considered in the velocity calculations. After a brief discussion of apparatus compressibility measurement and its implications, this chapter wraps up with the data analysis workflow. Hopefully, this section can help future researchers avoid pitfalls made over the course of this research.

5.2 Triaxial Test Setup

5.2.1 Specimen Preparation and Initial Pressure-Up

As stated earlier, test setup is the most important process during a triaxial test. The main tasks on day one of testing are sample extrusion, specimen preparation, setting up the triaxial device, inputting parameters to the computer, and beginning the pressure up sequence. In the pressure up process, the specimen is isotropically reloaded to bring the specimen back to its sampling effective stress while maintaining piston-top cap contact. This process allows one to check for internal leaks as well.

The following is a detailed step by step on the tasks completed on day one of a typical triaxial test during this research. These steps are the same for intact and resedimented specimens. The following steps begin after the specimen has been trimmed to the dimensions specified in Chapter 3. Please note that all zero values mentioned refer to the normalized zero, which is the transducer voltage output divided by the input voltage (generally 5.5 V).

1. Log test number and test details (name, material, project, etc.) in laboratory testing logbook and fill in appropriate sections of triaxial testing datasheet.
2. Wrap trimmed and measured specimen in wax paper and place in a plastic bag to avoid desiccation during setup. Place this plastic bag inside another bag with a damp paper towel inside.
3. Prepare a 350 mL sea salt solution in a 1L capacity vacuum flask with the appropriate salt concentration and mix until all salt grains are dissolved. If the vacuum flask is too small, it runs the risk of tipping over or breaking during the preparation procedure. For all tests in this research, a salt concentration of 80 g/L was used.
4. Carefully transport the specimen, membrane stretcher, specimen alignment jig, vacuum flask of salt water, scissors, large adjustable wrenches (x2), and a rubber mallet to the triaxial testing station. Using the utility cart is the easiest way to do this.
5. Gather two annular porous stones, two filter papers, a condom, two 0.025-inch thick 1.4-inch diameter triaxial membranes, six 1.4-inch diameter O-rings, and vacuum grease.
6. Use the vacuum grease to lightly grease the sides of the brass bottom and top cap. Clean hands with a paper towel afterwards.
7. Remove condom from packaging and cut one inch off the tip and cut off another 1-inch section which will be used to hold the horizontal actuators in place.
8. Stretch condom onto the bottom cap so that it can be rolled upwards and over the specimen. Keep it long enough so it can roll over the top cap as well.

9. Place the porous stones on the top and bottom cap and position the filter papers.
10. Place and position the specimen so the bottom cap shear actuator is aligned with the wide, rounded radial axis. Put to top cap on as well.
11. Apply a miniscule amount of vacuum grease to the side actuators and fix them to the specimen using the 1-inch section of condom.
12. Roll the condom up and over the specimen and top cap. Make sure no wrinkles are present, as these can act as conduits for water or cell fluid.
13. Measure the height of the center of the horizontal actuators from the top of the porous stone. This will be necessary for the inclined velocity measurement.
14. Apply some more vacuum grease on the condom covering the top and bottom cap to provide a seal between the 1.4-inch membrane and condom.
15. Using the membrane stretcher, carefully enclose the specimen with one 0.025-inch thick 1.4-inch diameter membrane. Use the O-ring stretcher to attach two greased O-rings on the bottom cap and two on the top cap. Re-grease the ends.
16. Attach another thick membrane using the stretcher. This time one O-ring will be put on each end in-between the pair already on each end. This makes a tight seal, so leaks are less likely to occur. Try not to miss the narrow gap.
17. Slide the top drain line over the specimen, hold the specimen in place with the alignment jig, and screw the drain line into the top cap and base using a three-eighths-inch box wrench. Make sure to grease O-rings on the drain line and clean debris out of threaded holes before screwing them in.
18. Connect P and S-wave actuator wires to the top cap and appropriate 9-pin connector on the base.
19. Keeping the alignment jig in place, use the vacuum flask and tubes with rubber stoppers on them to pull a vacuum on the pore pressure transducer port on the base. This will draw excess air trapped in the condom and membranes out, letting the top cap be in tight contact with the specimen. Keep this vacuum running until step 31. Over time the water will de-gas and stop boiling. Then, the tube is pushed further through the rubber stopper in the top of the vacuum

flask until the tip immersed in the salt water. It should bubble slightly as gas is pulled out of the system. If no leaks are present, it will eventually stop bubbling. The top and bottom drain valves should be open during this process.

20. Check whether the piston was retracted after the last test by using the two large wrenches. If not retracted, when the cell is lowered onto the base the piston can destroy the test specimen.
21. Grease the large O-ring on the base, then use the electric winch to pick up the triaxial cell.
22. Reduce the winch speed, and slowly lower the triaxial cell onto the base. Once it is a few inches away from the base, plug the internal load cell into the 9-pin connector. Monitor the load cell channel on the voltmeter as the triaxial cell is lowered the remainder of the way to make sure it is not crushing the specimen.
23. Tighten the cell to the base using a torque wrench, nuts, and washers with 35 Nm of torque. The nuts should get tightened in opposing pairs and not all the way at once for each pair to ensure a relatively even pressure on the base O-ring.
24. Begin central data acquisition recording task on all transducer and power supply channels. The load cell zero is taken from this first reading when the piston is not in contact with the specimen. In addition to the DAQ, record voltages shown by TX station PC as these voltages can differ due to using a different A/D converter (AD1170).
25. Use the rubber mallet to tap the piston down lightly until it meets the top of the specimen/top cap. Check the load cell channel while tapping to look for the moment the voltage changes, indicating the load cell feels the contact with the top cap. At this moment, get a manual reading on the DAQ for the zero of the axial LVDT. A depth micrometer measurement of the protruding piston can indicate whether contact with the top cap is achieved as well. The LVDT position is set using a steel dummy specimen to ensure the LVDT starts in the beginning of the linear range and stays there throughout the test.

26. Using the manual controls, raise the base of triaxial cell until the piston contacts the load frame. The steel ball used as the moment break should still rotate but not feel tight.
27. Fill the cell with fluid by pressurizing the silicone oil chamber to 20 PSI and opening the Swagelok valve to the pressure chamber on the base of the triaxial cell. Use the overflow bubbler device to monitor when the cell is full. The clear tube will fill with silicone oil when it is full, and at this point the base Swagelok valve should be shut off first, then the swage valve at the top where the bubbler is attached.
28. Open the valve on the Cell PVA and the valve on the TX base that connects to the cell. Perform a manual reading on the DAQ to record the cell pressure zero value.
29. Close the valve on the Cell PVA but leave the base valve open to cell. Now the Cell PVA can be used to increase the cell pressure.
30. Input normalized zero voltages for cell pressure transducer, axial LVDT, and load cell into the TX station PC, as well as the specimen measurements and appropriate transducer calibration factors. Go to pressure up (or target stress) subroutine and type in appropriate pressure up values. For this research, a cell pressure of 3 KSC was selected, as this is 1 KSC above the effective stress the sample experienced before extrusion. A deviatoric stress of about 0.1 KSC is applied as well to keep the piston in contact with the top cap as the hydrostatic loading can cause it to lift off.
31. Turn the cell and axial motor switches on the box to the computer control mode, and let the computer take over the test. The pore PVA motor should remain off during this time. To give a bit of a boost, use the cell fluid pressure chamber used to fill the cell to apply pressure cell. This will save the cell PVA piston stroke.
32. Once the target stress is achieved, the system is ready to be vacuum saturated. At this point the water in the vacuum flask should be bubble-free. Ensure that the top and bottom drains remain open so that the entire pore fluid system

(specimen, pipes, PVA) are under vacuum. Pulling off the vacuum hose from the side of the vacuum flask will cause water to be drawn into the system, saturating it. The pore pressure transducer is then reattached and hand tightened. Open the pore PVA valve to the atmosphere and record the zero value for pore pressure. This can be entered in manually using the ctrl + break command on the keyboard, the F6 button, and typing the normalized zero value manually for the "zpore" variable.

33. Close the top and bottom drainage lines so pore pressure can build up. Keep the pore PVA motor switch off and use the current Volumetric strain LVDT voltage as the zero.
34. Clean up tools and check to make sure the computer controls are stable.
35. Wait for 24 hours. An axial strain of < 0.4% ε_a and a pore pressure increase of about 1 KSC should be observed. If the pore pressure is equal to the cell pressure after waiting, there is likely an internal leak and cell fluid is entering the specimen. If this happens, take apart the cell by first reducing the axial stress and then the cell pressure, then repeat the setup process after obtaining a new set of dimensions and mass measurements.

5.2.2 Backpressure Saturation

The next step is backpressure saturation, where backpressure is applied and dissolves any air bubbles still present in the pore fluid system and specimen. On this day, the pore pressure is incrementally stepped up using the PC subroutine until about 4 KSC, at which point all air bubbles should go into solution. Axial stress and cell pressure are proportionally stepped up during this process to maintain the sampling effective stress. Increments of pressure should be added every 1 KSC at a time over 5 – 10 minutes. The specimen is then held for 24 hours or until the volumetric strain stabilizes. This stability implies that the specimen has absorbed as much water as it will, and the PVA motor no longer needs to work to maintain the

target pore pressure. If there is a linear decrease in the volumetric strain, there is likely an external leak, so pore lines need to be checked.

To test the saturation of the specimen the next day once the volumetric strain has stabilized, the Skempton B parameter is measured using the following relationship:

$$B = \frac{\Delta u}{\Delta \sigma_c} = \frac{1}{1 + n\frac{C_w}{C_{sk}}} \tag{5.1}$$

Where Δu is the change in pore pressure, $\Delta\sigma_c$ is the change in cell pressure, n is the porosity, C_w is the compressibility of water (kPa^{-1}), and C_{sk} is the compressibility of the soil skeleton (kPa^{-1}) [35]. The proportional increase in pore pressure in response to an applied cell pressure gives the B-value. Soft, normally consolidated to medium stiff clays will show a B = 1 when fully saturated, though a B-value above 0.95 is considered acceptable. For this research, a cell pressure application of 0.5 KSC was used to test the B-value. The specimen needs to be undrained for this to work, so top and bottom drain lines are closed during the cell pressure increment. If the B-value is too low (0.9 or lower), step up the back pressure another 1 KSC while maintaining the sampling effective stress and wait another 24 hours before re-measuring the B-value. If the B-value is greater than one, there is likely an internal leak so one cannot perform K_0 consolidation at the test setup process needs to be repeated.

5.2.3 Stress Path Consolidation

After obtaining a good B-value, a one more step is required before drained consolidation can be performed. This step is to reset the volumetric strain LVDT zero value, as the piston moved when applying back pressure to the specimen. The new volumetric strain LVDT zero should put the volumetric strain at 3 times that of the axial strain, as the sample should have deformed isotropically (ignoring the stiffness anisotropy). Thus, the cross-sectional area is slightly smaller than when measured.

To perform stress path consolidation, the strain rate, final axial effective stress, and final radial effective stress are inputted into the stress path subroutine. This allows the user freedom to choose any stress path possible. In this research, lateral stress ratios of K = 1, 0.85, 0.8, 0.75, and K_0 were chosen. The back pressure from back pressure saturation is maintained throughout stress path consolidation, making this a fully saturated, drained test. Tests were consolidated using strain control at a strain rate of 0.07 %/hr for BBC and about 0.06 %/hr for RGoM-EI clay.

Throughout consolidation, the five velocities are collected roughly every 1 MPa to generate a relationship between mean effective stress and velocity. Velocity measurements were taken on the VCL without stopping the motors for RGoM-EI tests, and motors were stopped every 1 MPa for BBC tests. The same velocity collection process was used during K_0 consolidation as well.

5.2.4 K_0 Consolidation

K_0 consolidation requires more confidence in the test setup, as the test relies greatly on a leak-free system and carefully tuned PID control algorithm constants. To test whether the test is leak free before K0 consolidation, the pore motor is switched off and drain lines closed with the pore pressure transducer monitoring the specimen. If the pressure continuously increases at this point, that means that cell fluid is leaking through the membrane into the specimen and driving the pore pressure up. A decrease in pressure would imply an external leak in the system between the system and the drain lines. If the specimen pore pressure does not fluctuate for about 5 minutes, then the test is ready to proceed.

To maintain the same cross sectional area during consolidation, the algorithm adjusts the cell pressure to keep the change in volumetric strain of the specimen equal to the change in axial. This is based on the assumption that no bulging occurs and the specimen remains a right cylinder, thus all strain experienced by the specimen is in the axial dimension [42]. Somewhat different than the stress path consolidation

subroutine, the limiting conditions of K_0 are the maximum axial strain and maximum effective stress allowed. The desired strain rate is set for this subroutine as well. This type of consolidation can take a 2 – 3 weeks for each test at a strain rate of 0.06 %/hr, as specimens undergo much more axial strain during K_0 than isotropic consolidation.

5.2.5 Secondary Compression

Once the desired end stress or strain condition is met from either stress path or K0 consolidation, the computer takes the specimen into a hold stress subroutine. Depending on the strain rate or the clay permeability, one may have slight excess pore pressures built up which need time to drain before the specimen can be sheared. Thus, the specimen is held at the same state of stress for at least 24 hours. During this time, the specimen undergoes axial and volumetric deformation due to secondary compression.

Secondary compression is the phenomenon where at a constant effective stress, the specimen continues volumetrically deforming. It is a specific type of creep, where creep is the time-dependent strain behavior of a material at constant total stress. The rate of secondary compression is influenced by numerous factors, a few of which are the consolidation stress, load increment ratio, and specimen mineralogy. Though it is a topic for debate, it is thought that pore pressure remains constant during secondary compression, and the driving force is purely mechanical reorientation or collapse of grains.

5.2.6 Undrained Shear

To check that the specimen is ready for the undrained shear phase of triaxial testing, a similar test to the leak check is conducted. The drain lines are closed, and the pore pressure monitored for about 5 minutes. If the pore pressure continues increasing, it means that the specimen needs to be held at the same effective stress for more time. For this research, the pore pressure increase was monitored every 24 hours until the

specimen exhibited no more increase in the pore pressure with closed drain lines. The drain lines remained open between leak checks while the computer was in the hold stress subroutine.

To shear the specimen, the undrained shear subroutine is selected, and the strain rate, limiting axial total stress, and limit axial strain are selected. For this research, a strain rate of 0.5 %/hr was selected with a strain limit at 10% plus whatever axial strain had been accumulated during consolidation. Only undrained shear in compression was tested for this research. Only vertical P and S-save velocities were collected during undrained shear as the specimen bulges unpredictably during undrained shear, rendering the horizontal and inclined velocities useless. Velocities were measured at about every 0.5 % axial strain during undrained shearing. Since the volume of the specimen doesn't change during undrained shear, the void ratio should remain the same and therefore the P-wave velocity should remain constant.

5.3 Signal Collection and Processing

5.3.1 Arrival Picking and Velocity Modeling

Once the stacks of input and output waveforms for consolidation and shear were collected and saved to the USB, they were backed up to the cloud and analyzed. First, the oscilloscope waveform data is imported to a custom velocity calculation spreadsheet. This spreadsheet allows one to manually select the arrival time based on the wave shape as seen in Figure 51 and Figure 52. The arrival times in this research were selected using the pulse first arrival method, where the first significant change in amplitude is chosen as the arrival [43]. This method is chosen due to its relative simplicity and because minimal noise is present in the output signals. In cases with more noise, more complex methods like signal cross-correlation can be conducted [44]. Once the arrival times are selected, the stress and strain values derived from the data reduction at the times of measurement need to be inputted.

The specimen dry mass is required to proceed with the phase relationship and data reduction calculations. Mass measurements were conducted weekly until no fluctuations in mass were recorded. Once the mass is obtained and the data reduced using the reduction program, the data is ready for use in the velocity calculations. Since velocity recordings correspond to a given manual DAQ reading, a single row of reduced data corresponds to the soil engineering properties at that measurement. The axial strain, volumetric strain, axial stress, radial stress, and void ratio are then copied from the reduction to the velocity spreadsheet. Now, the velocity is calculated using equation 2.1 after the distances are corrected for whatever strain occurred. Using this data, a relationship between the mean effective stress and wave velocity can be constructed as seen in Figure 53. The same process is done for the shear waves as well (Figure 54). The same process is replicated for the undrained shear P and S-wave velocities, just without the horizontal and inclined waveforms. The horizontal and inclined velocities become unusable due to the specimen bulging and there being no internal strain measurements.

Once all velocities are compiled for a test, a power law model can be used to obtain velocities from any stress level throughout the test. The two equations used to model the P and S-wave velocity with mean effective stress are shown as follows:

$$V_P = 1500 + A(\sigma'_m)^B \tag{5.2}$$

$$V_S = C(\sigma'_m)^D \tag{5.3}$$

Where A, B, C, and D are shape parameters solved for by trying to minimize the sum squared error between the model and the test's velocity data by iteratively altering the shape parameters.

5.3.2 Actuator Calibration

Due to factors like wire length, actuator inertia, epoxy, and the glass slides on the face of the velocity actuators, the velocity system requires calibration. These physical layers between the actuator and the specimen cause the travel distance to be greater,

affecting the velocity values. Using the methodology from Ranjpour 2020, a series of PVC and acrylic spacers of known length were used to find the delay time of the velocity system [19]. The results of the calibration are shown below from Figure 55 - Figure 59. The validity of the assumption for the inclined wave that the center-to-center distance is appropriate to use was tested as well, as the center-to-center distance shows the least velocity variability over multiple PVC specimen lengths (Figure 57). The multiple materials tested show that there is nearly no variability in delay time. Averaged delay values were used for the inclined wave velocity calculations for consistency.

5.4 Apparatus Compressibility

5.4.1 Methodology

During triaxial testing, the axial deviator load applied often exceeds 500 kg and the cell pressure 10 MPa. These forces, while not high enough to plastically deform steel, are enough to cause elastic deformation of the piston string and of the cell. These deformations are made even larger by backlash in the gasket seal of the bottom cap, gaps between the porous stones and bottom cap, and screw connections of the cell itself. These deformations manifest as an increase in axial strain even though the specimen itself is not deforming. Thus, it is important to quantify and correct for the apparatus compressibility.

The apparatus compressibility of the piston string (piston through bottom cap parts) is measured by putting a stainless-steel dummy specimen in the cell and applying load using the axial motor. Similar to specimen setup, a vacuum should be applied to the dummy in a membrane so backlash between the specimen, porous stones, and top cap can be minimized. This simulates the conditions during the beginning of a test, which are of interest. Then, the load channel, axial LVDT channel, and input voltage channel are monitored using the central DAQ for at minimum two load/unload cycles. A chart of displacement versus applied load is then generated with these data, and

an equation is used to fit a curve to the data Figure 60. This relationship can then be used to correct the axial strain in real time during the test and during post-processing data reduction. The equation used to model apparatus compressibility is as follows:

$$Axial\ displacement = \frac{ax}{b+x} + \frac{cx}{d+x} \tag{5.4}$$

Where a, b, c, and d are shape parameters, axial displacement is in cm, and x is the axial load in kg.

A similar process is done to measure the apparatus compressibility due to cell pressure increase. This test was pioneered by Padraig Doran of TAG Lab. For this test, like before, a stainless-steel specimen in a membrane is vacuumed at the beginning to minimize backlash. Then, a load of 100 kg is applied to the system to further eliminate backlash in the system. At this point, cell fluid is introduced to the cell using the same pressure chamber method described earlier. The cell pressure is then increased and decreased for at least two cycles to build a relationship between cell pressure and axial deformation (Figure 61). The effects of cell pressure on axial strain are substantial, showing a 0.44 % axial strain error at 10 MPa for a standard 8.1 cm long test specimen. The cell apparatus compressibility can be corrected for using the relationship between cell pressure and axial deformation during the test and during post processing. In this research, the apparatus compressibility was corrected for during post-processing using a 2nd order polynomial.

5.4.2 Effects on Velocity

Apparatus compressibility will affect the calculated velocity because not all the measured axial strain will be caused by the specimen deforming. This implies that the velocity with no apparatus compressibility correction will be lower than the real velocity through the specimen because the specimen height is shorter after applying the correction. When apparatus compressibility is considered, the specimen is slightly larger than measured, so the actual velocity through the specimen is higher.

The worst-case scenario for error in velocity is at high axial stress with relatively high cell pressure. For a K_0 consolidated test at the maximum stress level (σ'_a = 10 MPa and σ'_c = 7.5 MPa), the combined axial and cell apparatus compressibility is 0.045 cm. The specimen height at this point is about 6.7 cm and the arrival time of the P-wave is 0.00003285 seconds. This means that the uncorrected P-wave velocity is 2037 m/s. When apparatus compressibility is considered, the velocity is about 2050 m/s. This means that the velocity error in the worst-case scenario underpredicts the velocity by 13.7 m/s, which is a -0.67 % error. Considering the minimum velocity threshold is 1500 m/s (the P-wave velocity through salt-water), if we subtract 1500 m/s from each velocity the error becomes about a 2.5% underprediction of velocity. In the case of isotropic consolidation, the same scenario results in a 1.76% underprediction. Apparatus compressibility also results in a systematic error in the radial strain which is calculated using the axial strain and volumetric strain, though this error is on the order of less than 1 m/s even at peak stress levels.

5.5 Error Analysis

Vertical S-wave arrival times in BBC and RBBC were not clear due to low signal amplitude, thus S-wave-derived values like anisotropy may be offset. If the wavelength of the arrival signal is similar in RBBC and RGoM-EI, this time offset could be as large as 50 μs, which could change the velocity of a test up to 160 m/s. The shift in velocity would be towards a faster arrival time, which would elevate the vertical S-wave velocity and thus produce a lower γ value. This would put S-wave anisotropy values closer to those from RGoM-EI. The near-vertical anisotropy, δ, values also are prone to error due to low signal amplitude and a low phase angle being chosen. There also are reproducibility errors in how plate actuators are oriented, as the actuators may shift during the specimen setup process. These errors were smaller in RGoM-EI, as S-wave arrivals were less attenuated. Overall, these problems can be rectified by shortening the specimen, increasing specimen width, increasing driver signal voltage, and maintaining a leak free pore pressure control system.

It cannot be stressed how important pore system maintenance is for successful triaxial testing. When lateral strain isn't measured internally, the volumetric strain is the only way to indirectly measure the radial strain. Deviations in void ratio due to leaks can also change the slope and shape of the compression curve. Tests were lost due to minor internal leaks stemming from the use of silicone plumbing caulk to thread the horizontal actuator wires from the 9-pin connector in the cell to inside the specimen membrane. Silicone cell fluid would flow into the cell along the wires, artificially inflating the volumetric strain. This problem was fixed by threading the wires directly through the brass bottom cap and epoxying the machined holes so pore fluid would not leak out from the specimen. Minor external leaks from aged and corroded copper pipes also occurred and were rectified by cleaning copper piping and valves and connections with calcium/lime/rust remover. Replacing the old, corroded swage ferrules also helped.

The arrival signals and driver circuit still require more improvements, though significant improvements were made during this research. The noise muddling the arrival time of the horizontal P-wave was remedied by isolating the receiver actuator ground from the driver ground. The range of the driver input voltage was increased from 16 to 23 volts, which increased the amplitude of arrival signals by a factor of 1.4. The apparatus compressibility due to axial load and cell pressure were considered, increasing signal accuracy further. Work is also underway to change the specimen geometry and increase the driver voltage, which will further increase arrival signal amplitude.

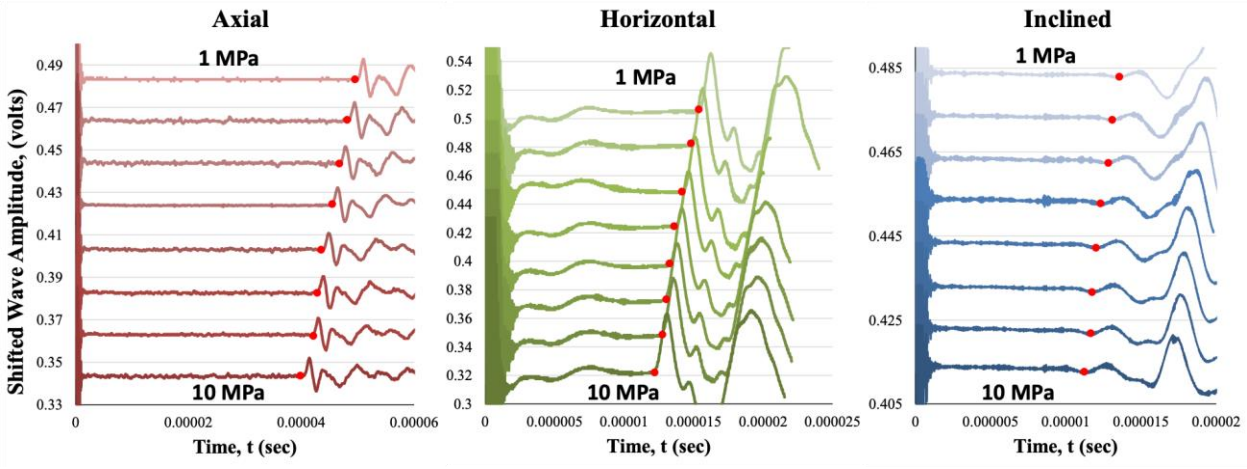

Figure 51. P-wave arrival picks (red dots) of a typical test during consolidation are shown for the axial (red), horizontal (green), and inclined (blue) waveforms.

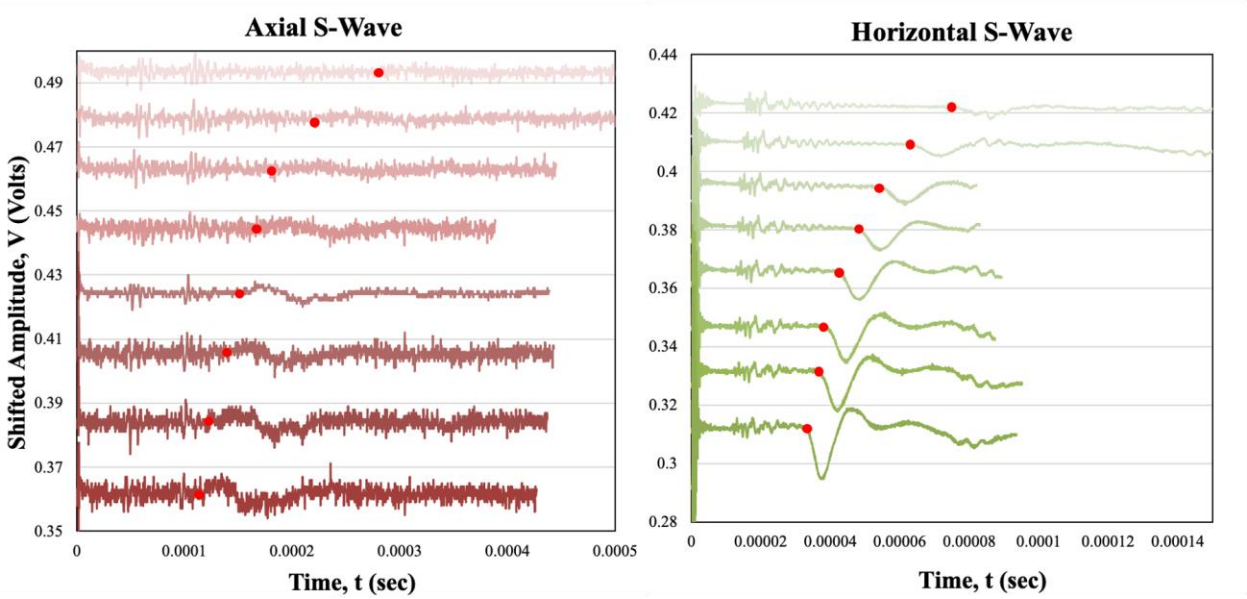

Figure 52. S-wave arrival picks (red dots) for a typical consolidation test. The vertical waveforms are red and horizontal are green, where once again the lighter shades represent lower stresses. The orientation of one of the horizontal S-wave actuators was rotated 180 degrees, which is why the arrival waveform is inverted.

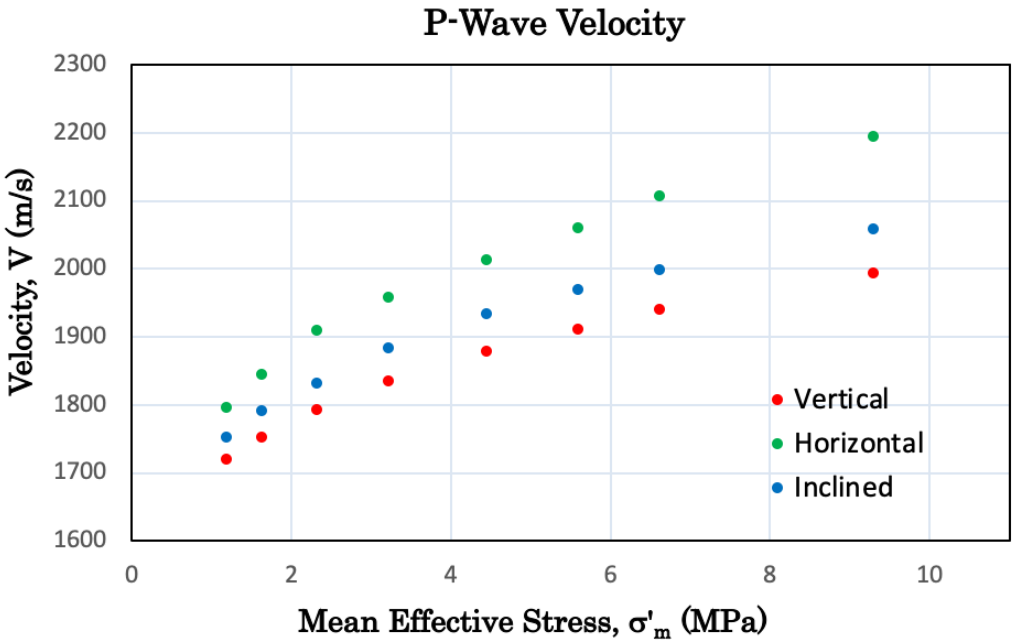

Figure 53. P-wave velocity vs mean effective stress. The vertical P-wave velocity is shown in red, while horizontal is green and inclined is blue.

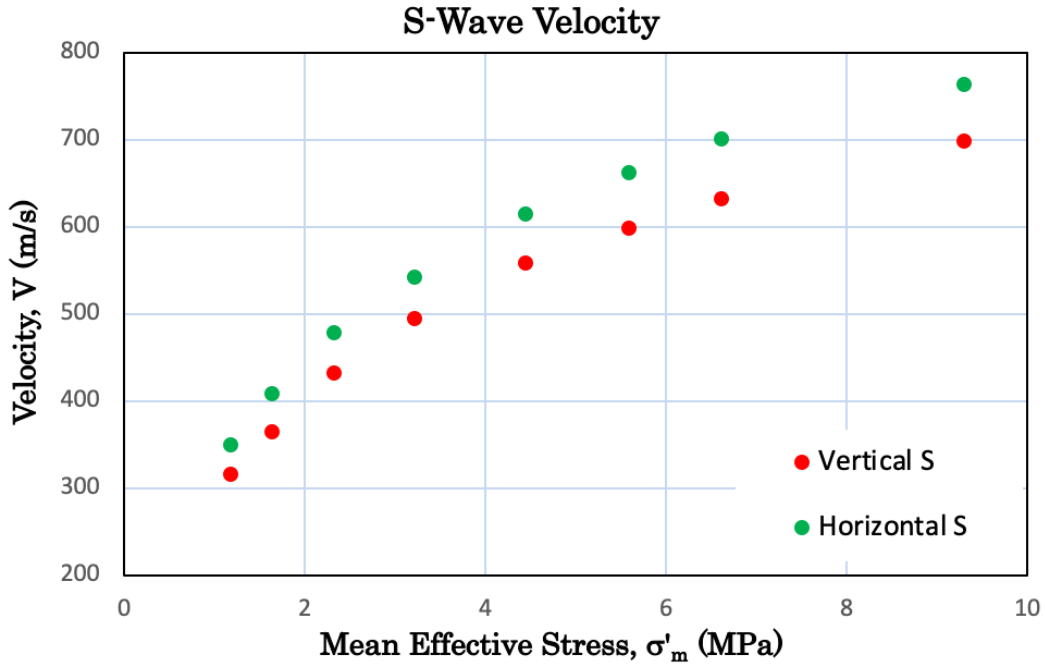

Figure 54. S-wave velocity vs mean effective stress. Once again, the vertical waves are shown in red while horizontal is green.

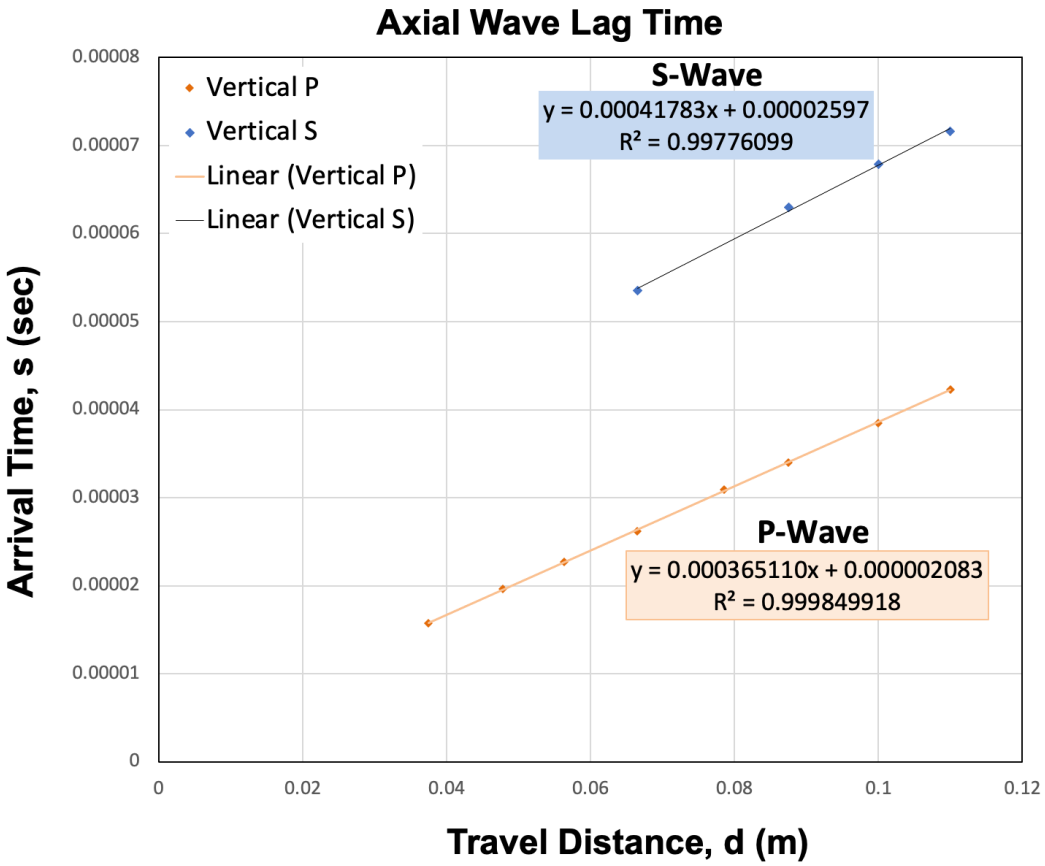

Figure 55. Experimentally derived wave delay times. The Y intercept is the delay time. Interpretation of the S-wave arrivals are more ambiguous, leading to the smaller r^2 value.

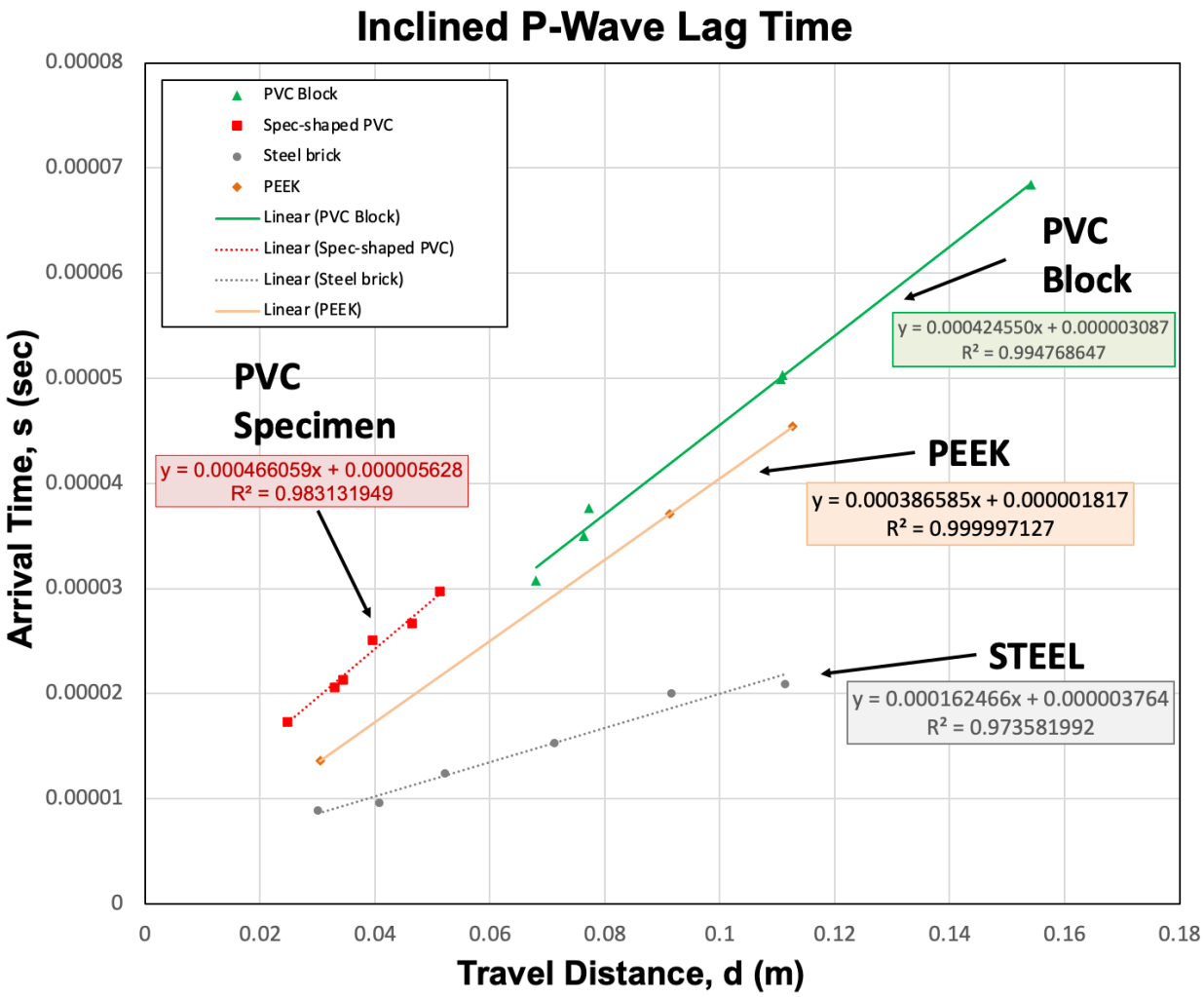

Figure 56. Inclined P-wave lag time calibration. Multiple materials were used to check the effect material has on the wave delay.

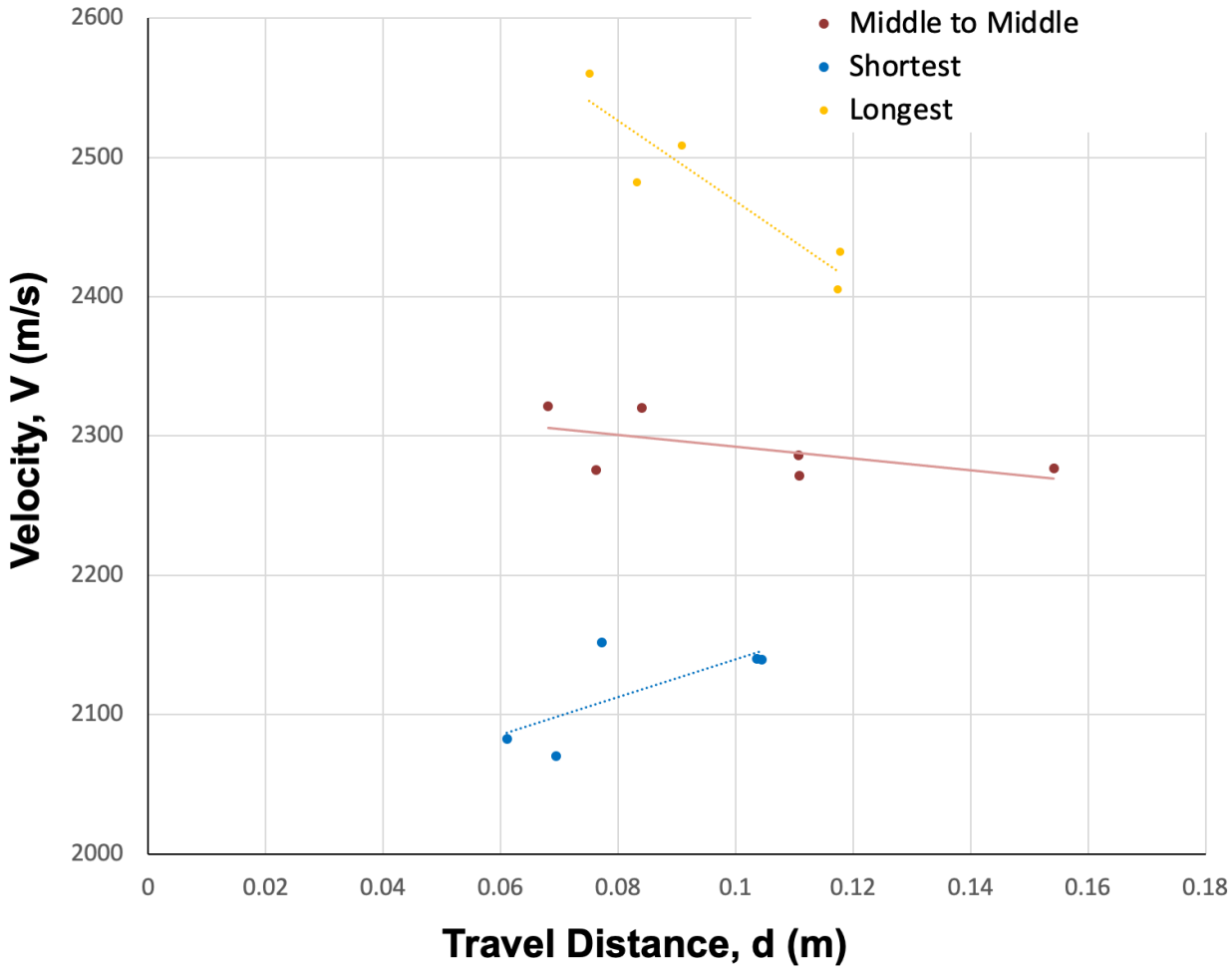

Figure 57. Test to check whether middle to middle distance is appropriate for inclined distance during velocity calculation. Inner edge to inner edge of the actuator is shown by the blue dots (shortest distance between actuators), and outer edge to outer edge is shown by yellow (longest distance). Although there is some scatter, middle to middle distance seems most appropriate.

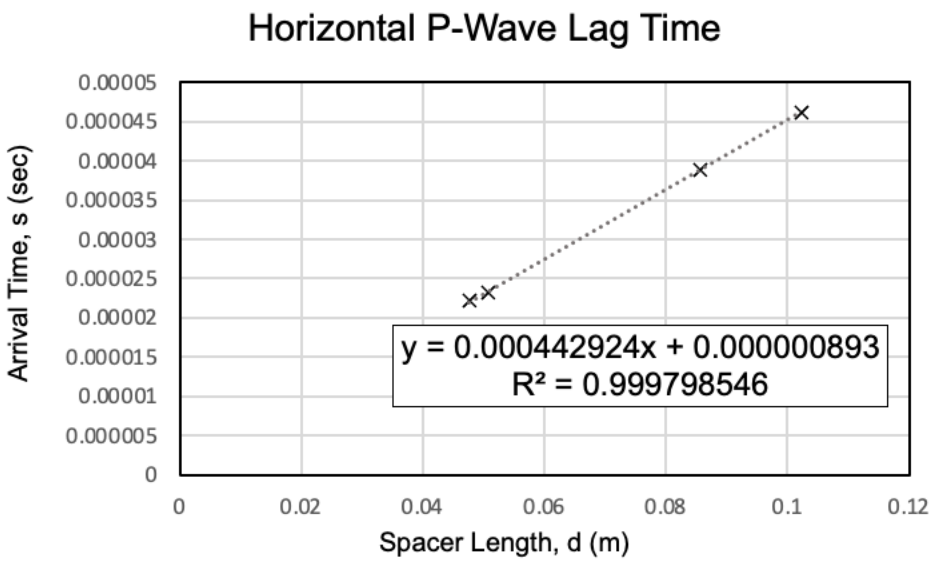

Figure 58. Horizontal P-wave calibration

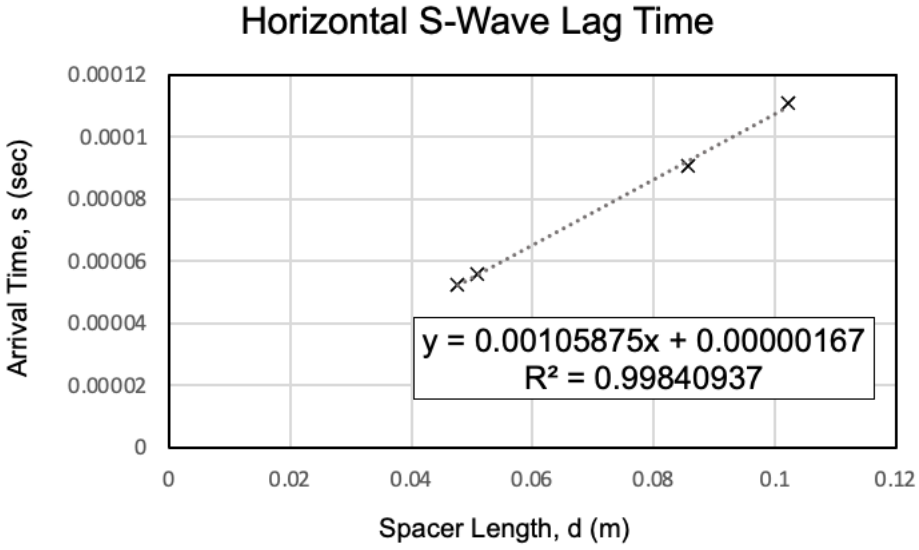

Figure 59. Horizontal S-wave calibration

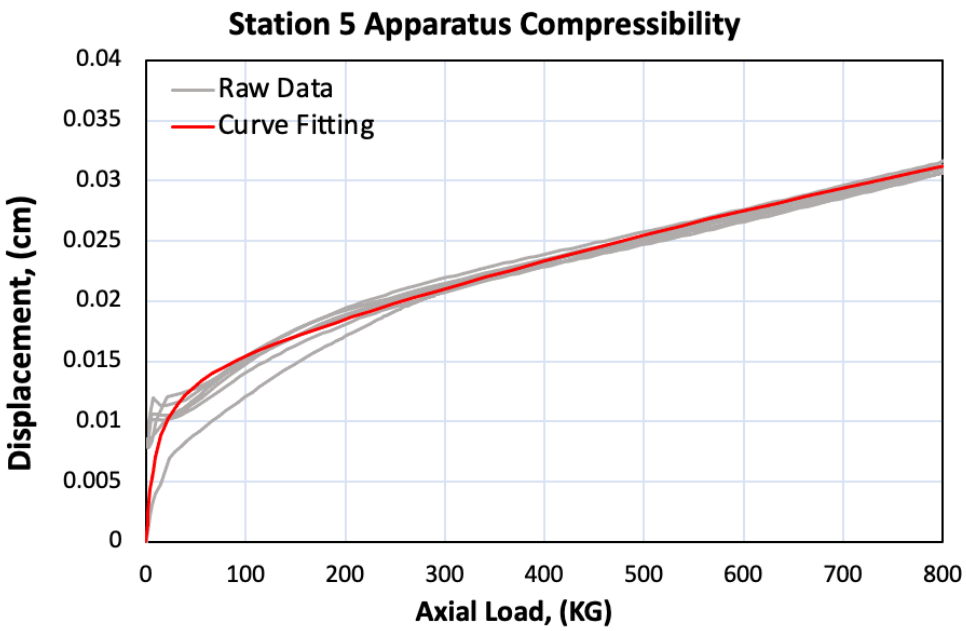

Figure 60. Axial piston string apparatus compressibility. Gray data is the raw data from loading/unloading and the red line is the fit curve.

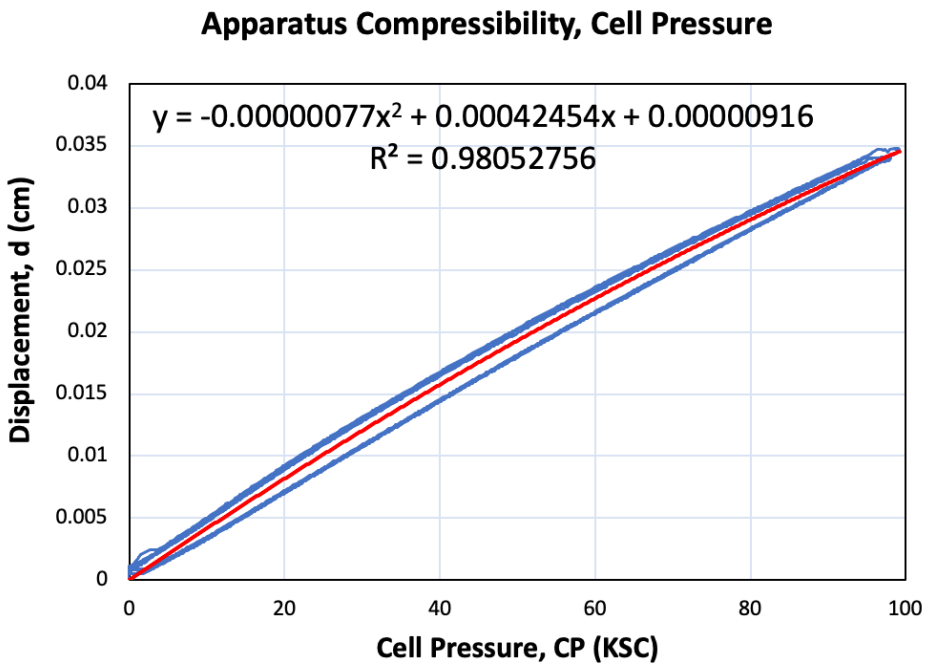

Figure 61. Apparatus compressibility of the cell. Deformations incurred during the 100 kg axial loading are subtracted from this figure. Red is the curve fit and blue is the raw data.

6 Experimental Results and Discussion

6.1 Overview of Experiments

A total of 10 successful medium stress triaxial tests with velocity measurements were conducted during this research (Table 3). Two of these tests were performed on BBC, one of which was on intact material and the other on resedimented. The remaining eight tests were performed on RGoM-EI clay. All resedimented samples were batched at a salinity of 80 g/L and 105% water content to ensure hydration and uniformity across samples. The resedimented samples were all consolidated to 0.8 MPa vertical effective stress as well, although some secondary compression due to samples remaining in resedimentation tubes did occur. This chapter covers the results of the tests performed and discusses the factors affecting velocity, velocity anisotropy, and the impacts of stress paths for normally consolidated specimens. TX1527 is thought to have had an internal leak issue but is included because velocity measurements are still reliable.

Table 3. Summary of all tests

Test No. Station	Material Type	Test Type	Initial			Normal Consolidation		At Max. Stress		
			w_0 (%)	e_0	σ'_p (MPa)	C_c	I	σ'_{vm} (MPa)	$K_{(NC)}$	e
TX1483 STA05	Intact BBC	CAUC (NC)	34.04	0.98	0.6	0.258	0.264	9.41	0.55 - 0.6	0.502
TX1485 STA05	RBBC	CAUC (NC)	32.89	0.869	0.8	0.280	0.268	10.73	0.55 - 0.59	0.471
TX1506 STA05	RGoM-EI	CIUC (NC)	33.38	1.003	0.8	0.371	0.350	9.77	1	0.519
TX1507 STA05	RGoM-EI	CIUC (NC)	33.35	1.013	0.8	0.386	0.351	9.31	1	0.534
TX1508 STA05	RGoM-EI	CAUC (NC)	33.73	1.04	0.8	0.388	0.360	6.02	0.75	0.537
TX1509 STA05	RGoM-EI	CAUC (NC)	33.49	1.016	0.8	0.334	0.339	10.03	0.8	0.49
TX1510 STA05	RGoM-EI	CK_0UC (NC)	33.15	0.987	0.8	0.346	0.313	12.29	0.66 - 0.74	0.471
TX1517 STA05	RGoM-EI	CAUC (NC)	34.18	1.02	0.8	0.335	0.337	12.21	0.85	0.479
TX1527 STA05	RGoM-EI	CAUC (NC)	34.35	1.045	0.8	0.413	0.390	8.69	0.76	0.49
TX1537 STA05	RGoM-EI	CIUC (NC)	33.71	1.026	0.8	0.336	0.335	7.23	0.99	0.54

6.1.1 Intact vs Resedimented Boston Blue Clay

The compression behavior of the intact BBC and resedimented BBC is very similar after overcoming the preconsolidation stress, as shown in Figure 62. Curves are plotted in void ratio versus log axial effective stress. Both clays were consolidated along anisotropic stress paths using K values equal to K_0 values measured from previous tests on RBBC. Stress path consolidation, rather than K_0, was selected because these tests were among the first conducted by the author and were prone to internal leak issues. The intact material was sampled from a similar depth and within 0.2 km of the RBBC site at MIT, so it is no surprise they exhibit similar compression properties. What is noteworthy, however, is that the intact material shows a "shoulder" in the beginning (upper left) of the compression curve before a steeper drop in void ratio, indicating structure or cementation of the clay. The resedimented specimen exhibited no such structured behavior, as lab resedimented samples lack the same sedimentation process and geochemical processes as sediments deposited in nature. In the geotechnical practice, such a structured clay soil could be cause for concern due to the large increase in compressibility after overcoming the preconsolidation stress and therefore high amounts of settlement could be observed during loading.

6.1.2 Resedimented Gulf of Mexico Eugene Island Clay

Compression curves for all tests on resedimented Gulf of Mexico Eugene Island clay are shown in Figure 63. Curves are plotted in void ratio vs log mean effective stress space. The colors represent the different lateral stress ratios, where shades of black represent the isotropic tests where K = 1, red is K = 0.85, purple K = 0.8, K = 0.75 being blues, and pink being K_0 (Figure 64). While MCC theory dictates that the slopes of the compression curves with differing K values should be parallel, this is not consistently observed. Instead, what is observed are similar slopes in tests conducted at similar lateral stress ratios, especially the isotropic tests. This deviation from MCC could be caused by K values changing throughout the test (i.e., TX1508, 1509, 1510),

the buildup of excess pore pressures inside the specimen, internal leaks changing the specimen area and therefore axial stress, and errors in the measured axial strain due to alignment issues. This could also be due to real clay compression behavior not matching modeled behavior precisely as well.

Minor errors in void ratio were identified and corrected for by comparing the final measured void ratios to those calculated from the volumetric strain in the data reduction software. These values often differed slightly, offsetting the compression curves along the void ratio axis. The difference between the phase relationship and data reduction void ratio (generally < 0.05) was applied as an offset to the data reduction void ratio, shifting the compression curves to where the physical measurements indicate they presumably should lie.

What is encouraging, however, is that despite these issues, the compression curves tend to decrease in void ratio throughout the test when there is more shear stress during normal consolidation. Another good quality indicator is that tests ran at duplicate lateral stress ratios tend to cluster. These clusters have similar compression indices as well, indicating that relatively consistent results are achieved (Table 3).

6.1.3 Comparison to In-House Data

RGoM-EI has been studied extensively over the years by Dr. Germaine and his students. Casey, Marjanovic, and Ranjpour ran medium stress K_0 triaxial tests on the material, while Nordquist, Horan, and Parry used the Constant Rate of Strain device for their research [19, 23, 38, 45-47]. Currently, Uyeturk is conducting both CRS and OED tests to carry out K_0 consolidation testing on RGoM-EI. Compression curves from this research are compared against data from Uyeturk's compiled average RGoM-EI K_0 compression curves. All curves from this research lie very slightly above Uyeturk's average, including the author's single K_0 consolidation test (Figure 65). The deviation of the average compression indices from all RGoM-EI tests

conducted in this research vs Uyeturk's is below 5%, giving confidence to the trends established by the compression data generated in this research.

6.2 Velocities

6.2.1 Intact vs Resedimented Boston Blue Clay

For BBC, P-wave velocities were measured in the vertical, horizontal, and inclined directions while only the horizontally polarized vertical and horizontal S-wave velocities are measured. Velocities were measured every 10 ksc (~1 MPa) axial effective stress from 1 – 10 MPa, where a hold stress routine ensured that stress is maintained for velocity measurement (Figure 62). This routine meant that a new target stress based on the stress dependent K_0 was chosen as the test advanced each 10 ksc increment in axial effective stress. The drawback of this approach was that sometimes a few hours of secondary compression occurred during the hold stress phases, leading to slightly elevated velocity values (5 – 15 m/s).

The combination of all P-wave velocities on intact and resedimented BBC in velocity vs axial effective stress space is shown in Figure 66. For both materials, the vertical velocity is the slowest, the inclined velocities are slightly higher, then the horizontal velocities are the fastest. Velocities all increase with increasing axial effective stress in a power law relationship. Similar trends are observed for the S-waves as well, where the horizontal S-waves are faster than the vertical (Figure 67). P-waves in the intact material were slightly slower overall (Figure 66). The S-wave velocities on the other hand were higher in the intact BBC vs the resedimented, possibly due to the stiffer material fabric from the natural sedimentation process. P-waves seem more controlled by the porosity, where since the intact material has a higher void ratio throughout most of the compression curve the intact P-waves are slower. More tests should be run on both materials in the future to verify these differences, however.

6.2.2 Resedimented Gulf of Mexico Eugene Island Clay

Like the velocity testing on BBC, tests on RGoM-EI clay were conducted at roughly 1 MPa increments over the 1 – 10 MPa stress range. These tests also measured V_{pV}, V_{sVH}, V_{pH}, V_{sHH}, and V_{pI} so the velocity anisotropy could be calculated. These velocities are plotted versus mean effective stress in Figure 68. What differs from the BBC velocities are that these measurements were made while the clay is still on the normal compression line with the motors still running, so velocities are not impacted by any secondary compression. The velocities could be impacted by very slight changes in stress (< 0.03 ksc) from the time difference between the first and last measurement, however. The horizontal velocity measurement circuitry was improved for this portion of testing as well, leading to sharper signal arrivals and less ambiguous arrival times. What is interesting to note, is that the more shear stress there is, the higher the P and S-wave velocity. This is similarly reflected in Figure 63, where higher shear stress tests tend to have lower void ratios at the same mean effective stress.

6.2.3 Comparison to In-House Data

In the BBC specimens, the vertical P and S-wave velocities compare well with those from Marjanovic, 2016 when compared in velocity – axial effective stress space (Figure 69, Figure 70). It should be noted however that this comparison is only valid for RBBC, and that the intact BBC test is shown only for consistency. For the vertical S-wave, the velocities from this research are slightly higher due to the different arrival time selection method, however the effects of this only become apparent at higher axial effective stresses. This ambiguity is caused by the low amplitude of the shear wave signal, which has now been improved moderately. Axial effective stress is used for the BBC comparisons rather than mean effective stress because of limited mean stress availability from past RBBC velocity tests.

For RGoM-EI specimens in the same velocity – axial effective stress space, the velocities from this research cluster together neatly and show agreement with the results from Ranjpour, 2020 (Figure 71, Figure 72). The improvements made to the axial signal by Ranjpour were very effective, as evidenced by the lack of scatter in the signals from this research. What remains unclear is why the velocities for Marjanovic's RGoM-EI measurements differ so much from this research and Ranjpour's despite the same material being tested in the same triaxial testing device.

6.3 Velocity Anisotropy

6.3.1 Intact vs Resedimented Boston Blue Clay

Figure 73 presents that velocity anisotropy is generally weak for BBC (anisotropy << 1), with only minor differences between the resedimented and intact material. There is a consistently higher horizontal velocity than the vertical for both the P and S-waves (Thomsen parameters ε and γ respectively) that appears to grow larger with increasing axial effective stress. The strongest anisotropy is observed in the horizontal versus vertical shear waves (γ), where values as high as 0.3 are observed. These higher γ values are likely reflective of the fabric of the material being composed of highly oriented grains. P-wave anisotropy is more reflective of the pore fluid, which drains as the specimen is compressed, leading to higher anisotropy. It starts off very low around 2 % at 1 MPa, and quintuples by 10 MPa. What is noteworthy as well, is that the γ values for the intact material are consistently about 0.05 higher than the resedimented, possibly due to the further particle orientation and layering from the natural sediment deposition process. ε may be lower for the intact BBC because of the higher specimen void ratio as well. The near vertical anisotropy, δ, remains below 0.1, and appears to decrease with increasing effective stress. This parameter has the biggest margin for error, however, since distances are small, the arrival signal weak, and lateral strain is not directly measured. Since the ε and δ parameters lie in a

similar range of values (and are equal at times) the wavefront shape is thought to be close to elliptical [4].

6.3.2 Resedimented Gulf of Mexico Eugene Island Clay

RGoM-EI clay, like BBC, exhibits relatively weak anisotropy regardless of stress state between 1 and 10 MPa mean effective stress. Its anisotropy values lie at or below 0.15, even for the γ parameter which was as high as 0.3 for BBC. Parameters tend to slightly increase as mean effective stress rises, although some γ values for certain tests remain constant. What is interesting is that the amount of shear stress doesn't appear to have an impact on the degree of anisotropy for the γ and δ values. The ε parameter, on the other hand, appears to be higher when there is more shear stress during consolidation. This indicates that the horizontal P-wave velocity increases proportionally more than the vertical with an increase in mean effective stress, especially when more shear stress is present. Like BBC, the wavefront geometry appears to be near elliptical, with hydrostatic stress path tests being closest to the ellipticity condition (Figure 75). In the $\delta - \varepsilon$ space the test data tends to cluster, with tests with the most shear stress being furthest from ellipticity due to their higher ε values. What is interesting is that even hydrostatic tests show increasing ε and δ parameters. This is thought to be a result of stiffness anisotropy arising from grain/void orientation, so the same stress applied on the top deforms the specimen more than the stress applied radially.

6.3.3 Comparison to In-House Data

Ranjpour, 2020 was the only study conducted at TAG Labs that experimentally derived the anisotropy parameters for RGoM-EI clay. Ranjpour ran K_0 consolidated tests ($K = 0.66 \sim 0.8$) and used power law fits of the velocity data to generate anisotropy parameters (Figure 76, Figure 77). The anisotropy behavior from Ranjpour 2020 agrees relatively well with this research, although trends deviate at

higher stresses. Ranjpour's δ parameters show a decreasing trend even though all tests in this research indicate δ increases with stress. The major takeaway is that both sets of research indicate that velocity anisotropy is relatively weak for RGoM-EI, staying at or under 0.1.

6.4 Stress Paths and Velocity Behavior

6.4.1 Sensitivity of Velocity to Compression Stress Paths

According to critical state soil mechanics that forms the basis of the MCC model, for any given stress path in a cohesive soil like clay, the porosity depends on the shear stress and mean effective stress. Porosity is equivalent along elliptical curves called iso-porosity lines, which are the same shape as MCC yield surfaces. Since density and the modulus control the P-wave velocity in cohesive soils, the iso-porosity curve is the same as the iso-velocity curve if modulus remains constant. Thus, the path taken to reach a particular velocity should not matter as long as the point lies on the iso-porosity ellipse. This theory was experimentally tested using the various stress path tests on RGoM-EI clay.

To evaluate the theory, all stress paths from the eight RGoM-EI tests were plotted in the same chart in $\sigma'_m - q$ space (Figure 78). Since every data point in the $\sigma'_m - q$ space has a corresponding row of reduction data which include stresses, strains, porosity, etc., the mean effective stresses were used to calculate the P-wave velocities with the fitted power law formulas. The corresponding $\sigma'_m - q$ values from points of equivalent velocity (i.e., 1,900 m/s across all tests' stress paths) and porosity were then plotted in this space on top of their corresponding stress paths (Figure 79, Figure 80). Porosity was calculated from the void ratio generated during data reduction.

The results from this research indicate that the shear stress acting on a specimen strongly affects P-wave velocity and porosity. It also appears that the shape of the iso-porosity and iso-velocity curves are similar, as evidenced by Figure 85 and Figure 86. Even if mean effective stress is the same between two points in $\sigma'_m - q$ space, if

any shear stress is acting on a point the vertical P-wave velocity will be higher than its isotropic counterpart and vice versa for porosity. Points at equivalent velocities and porosities mapped in $\sigma'_m - q$ space also form what appear to be elliptical curves, supporting MCC iso-porosity theory (Figure 79, Figure 80). This trend is still present when σ'_m and q values of iso-velocity and iso-porosity points are normalized to the maximum mean effective stress (Figure 84, Figure 85, Figure 86). It is also interesting that the normalized iso-velocity and porosity points nearly stack on top of one another in the normalized stress space, indicating a strong control on velocity by the porosity at these stresses. It is also interesting that the velocity and porosity datapoints lie closer to the undrained shear stress path rather than the MCC ellipse.

6.4.2 Velocity During Undrained Shear

Since porosity appears to greatly impact velocity during normal consolidation, if the test is undrained and no volumetric strain is allowed then the P-wave velocity should remain the same. During undrained shear, shear stress is applied at a constant strain rate of 0.5 %/hr with no drainage. Over time, excess pore pressure builds up within the specimen and its mean effective stress decreases until it reaches the critical state. In $\sigma'_m - q$ space, this should result in a quasi-elliptical or elliptical stress path that curves to the left until it hits a point on the critical state line (CSL). During this whole process the P-wave velocity should remain unchanged if it is controlled by porosity, and this ellipse should mirror the MCC iso-porosity curve because porosity remains the same.

Results from this research appear to support the MCC theory, as the test data shows that P-wave velocity remains nearly constant during undrained shear (Figure 81) and the points on the curve show relatively good agreement with those derived from drained compression (Figure 83). Interestingly, the S-wave velocities remain relatively constant as well, though they appear to fluctuate around 570 m/s. Research by Ranjpour showed that S-waves tend to decrease during undrained shear, so it

would be interesting to see what trends emerge as more undrained shear tests are performed. Another reason more undrained shear tests are necessary is that one dataset from a single CIUC test cannot adequately generalize velocity behavior. It has also been shown by other researchers at TAG Labs and MIT that the shape of the RGoM-EI yield surface is not elliptical but rather asymmetrical and stress path dependent, thus further tests are necessary to determine undrained shear velocity behavior.

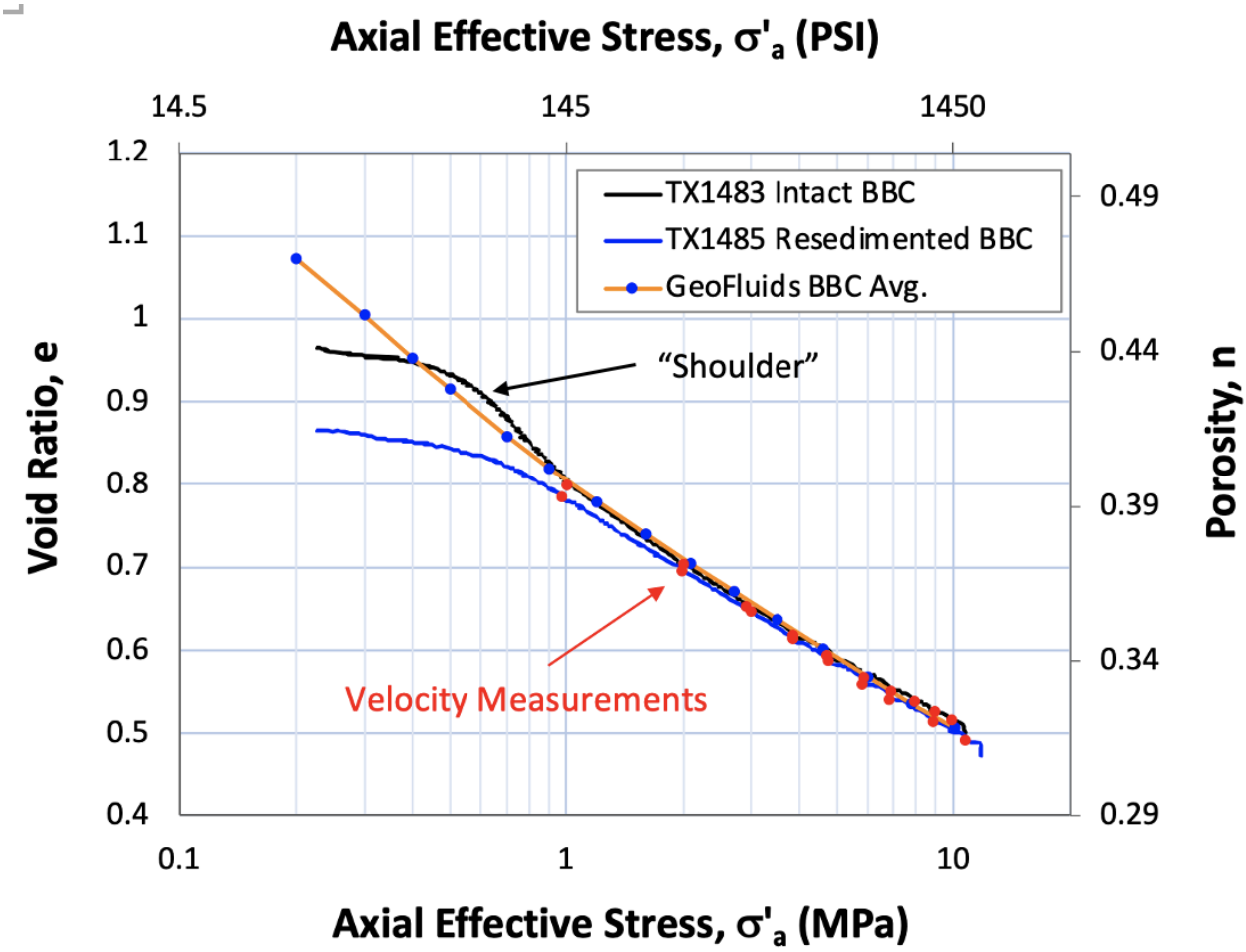

Figure 62. Compression curves of intact BBC (black), resedimented BBC (blue), and the GeoFluids average RBBC K_0 compression curve created by C. Emre Uyeturk (orange with blue points). Red dots represent stress levels with velocity measurements.

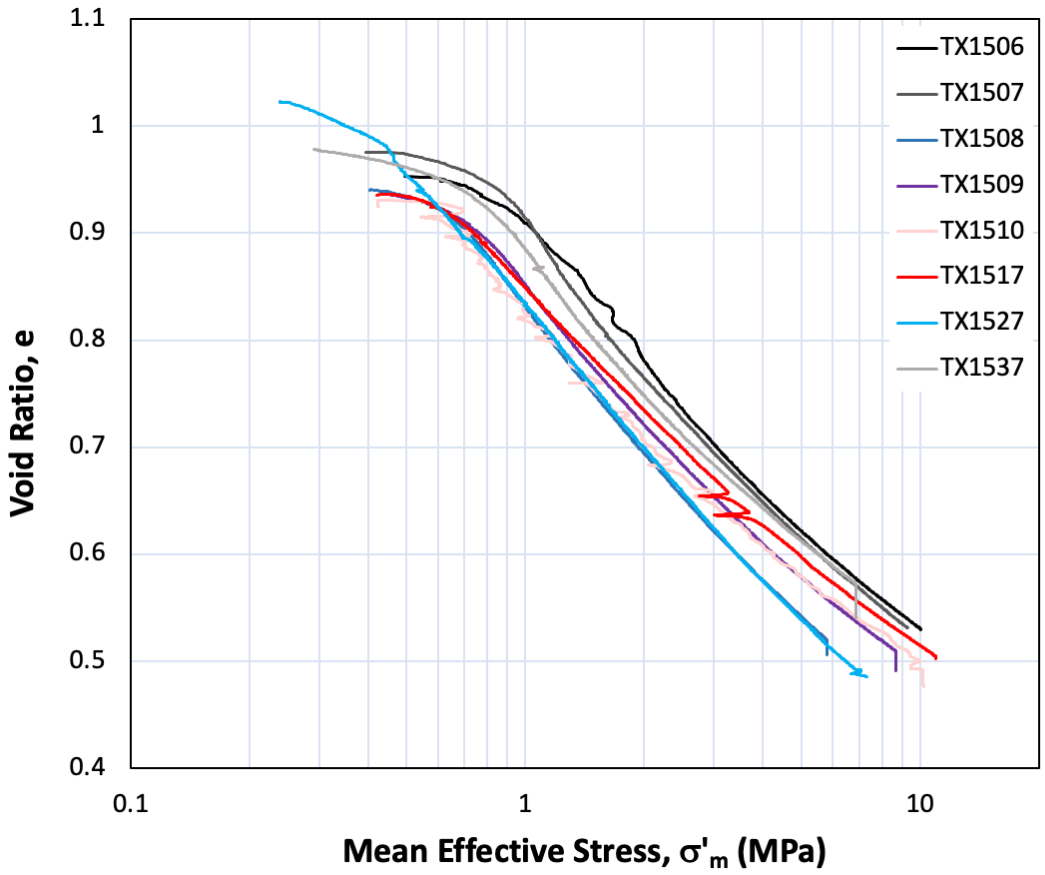

Figure 63. Compression curves from RGoM-EI tests on different stress paths. Black/gray tone curves are for isotropic (K = 1) tests, blue curves are at K = 0.75, red from K = 0.85, purple from K = 0.8, and pink from K_0.

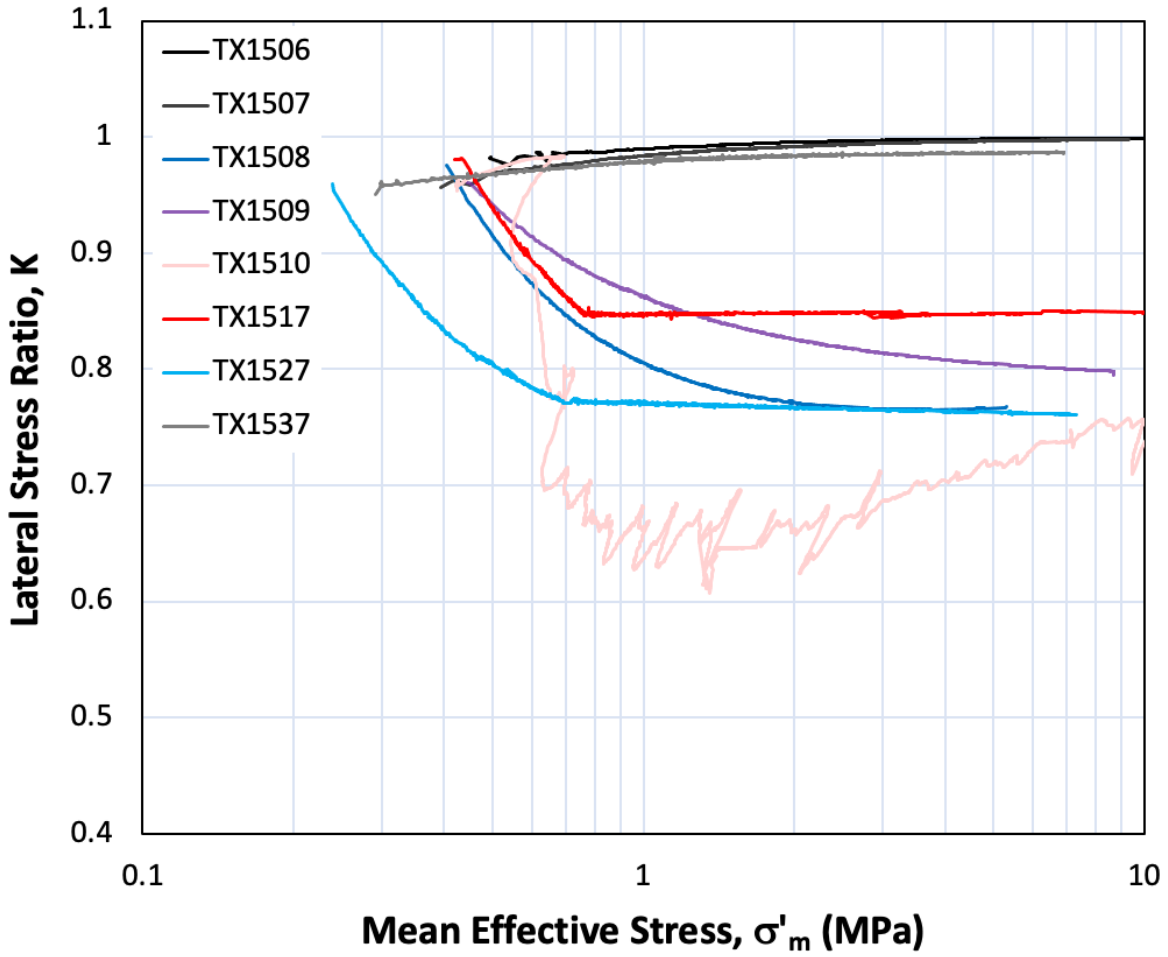

Figure 64. Lateral stress ratios by stress from all RGoM-EI tests. Color scheme is the same as before.

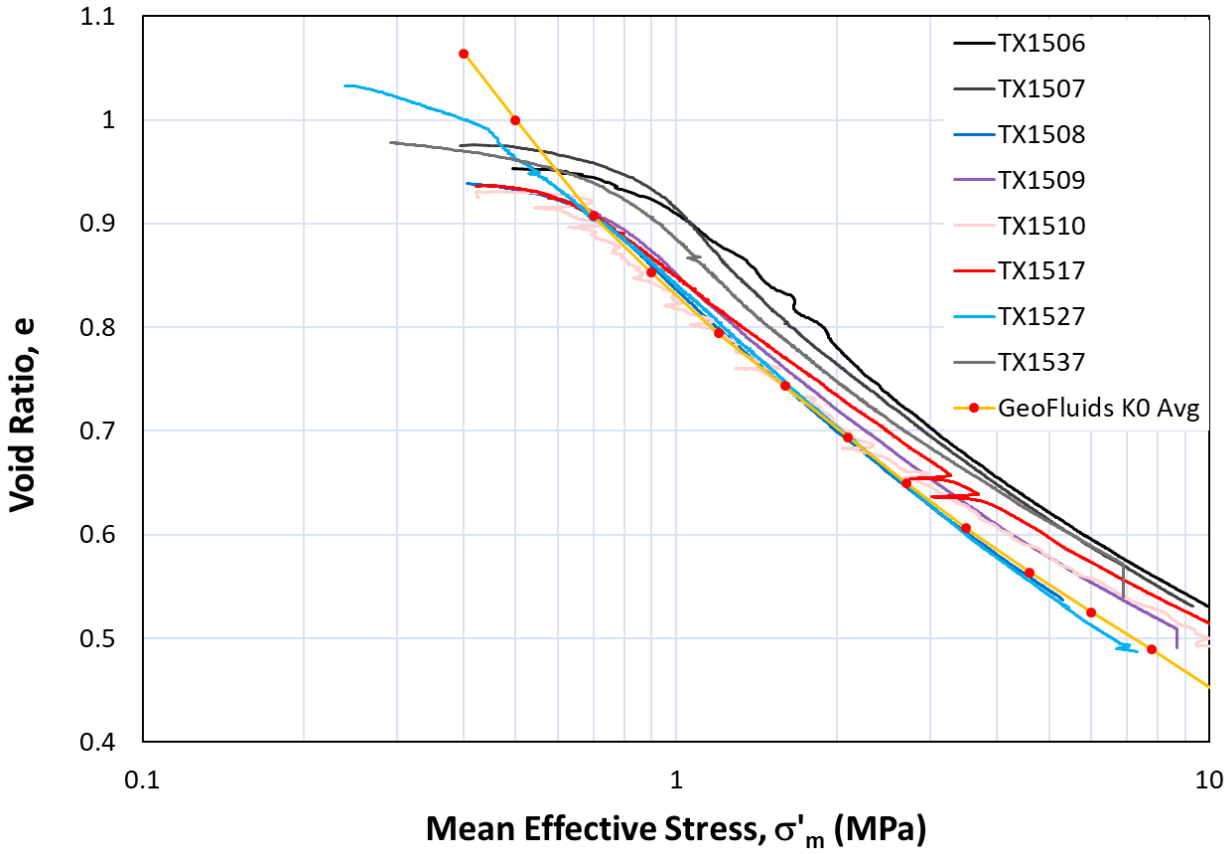

Figure 65. Comparison of RGoM-EI void ratio vs log axial effective stress data. The curves from this research show acceptable agreement to the GeoFluids average.

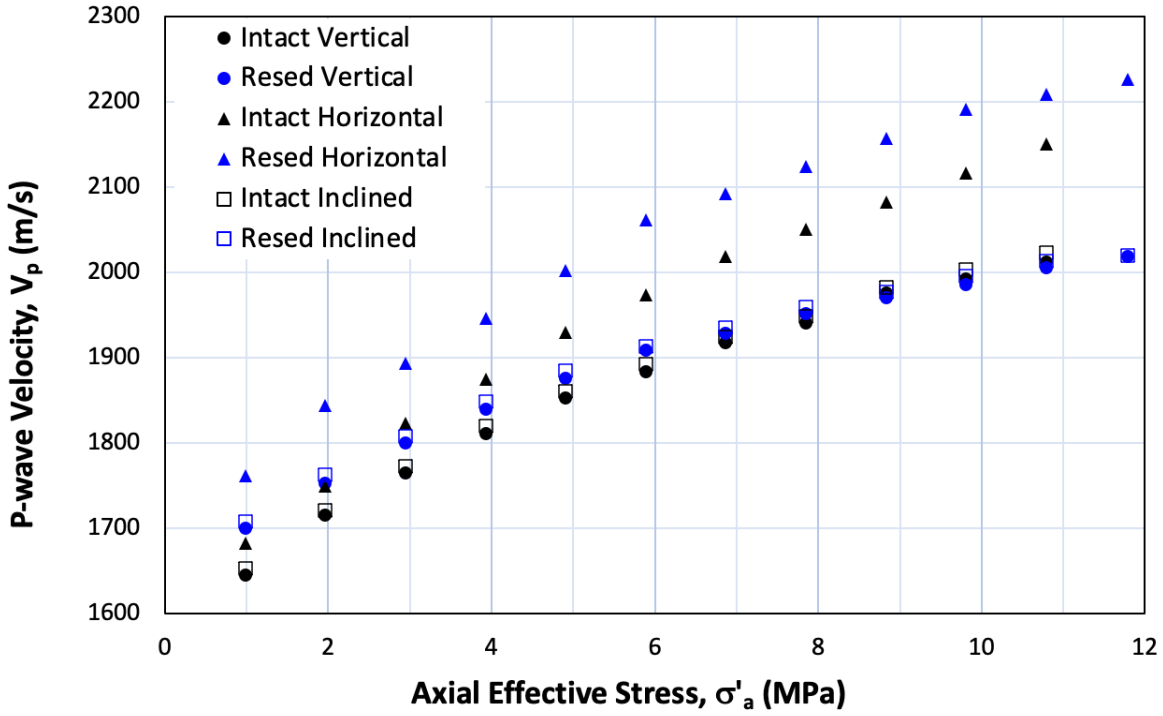

Figure 66. P-wave velocity versus axial effective stress. Blue markers represent resedimented velocities while black is intact. The vertical velocities are filled circles, horizontal are filled triangles, and inclined velocities are open squares.

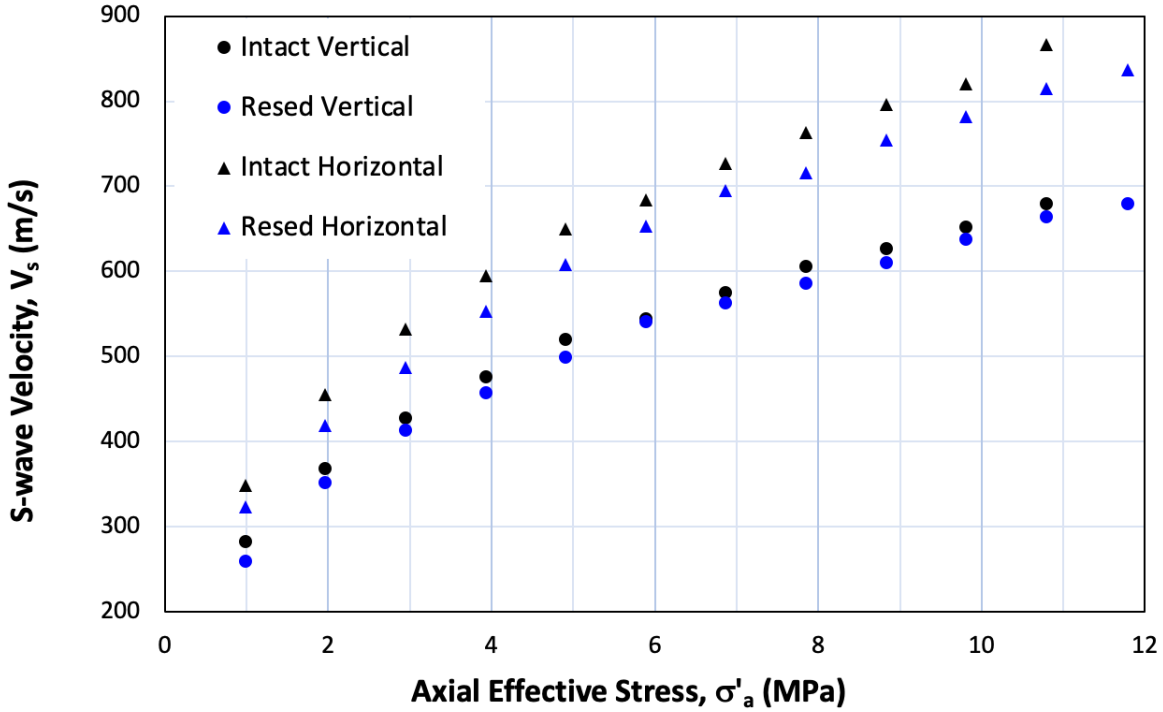

Figure 67. S-wave velocities in BBC (black) vs RBBC (blue).

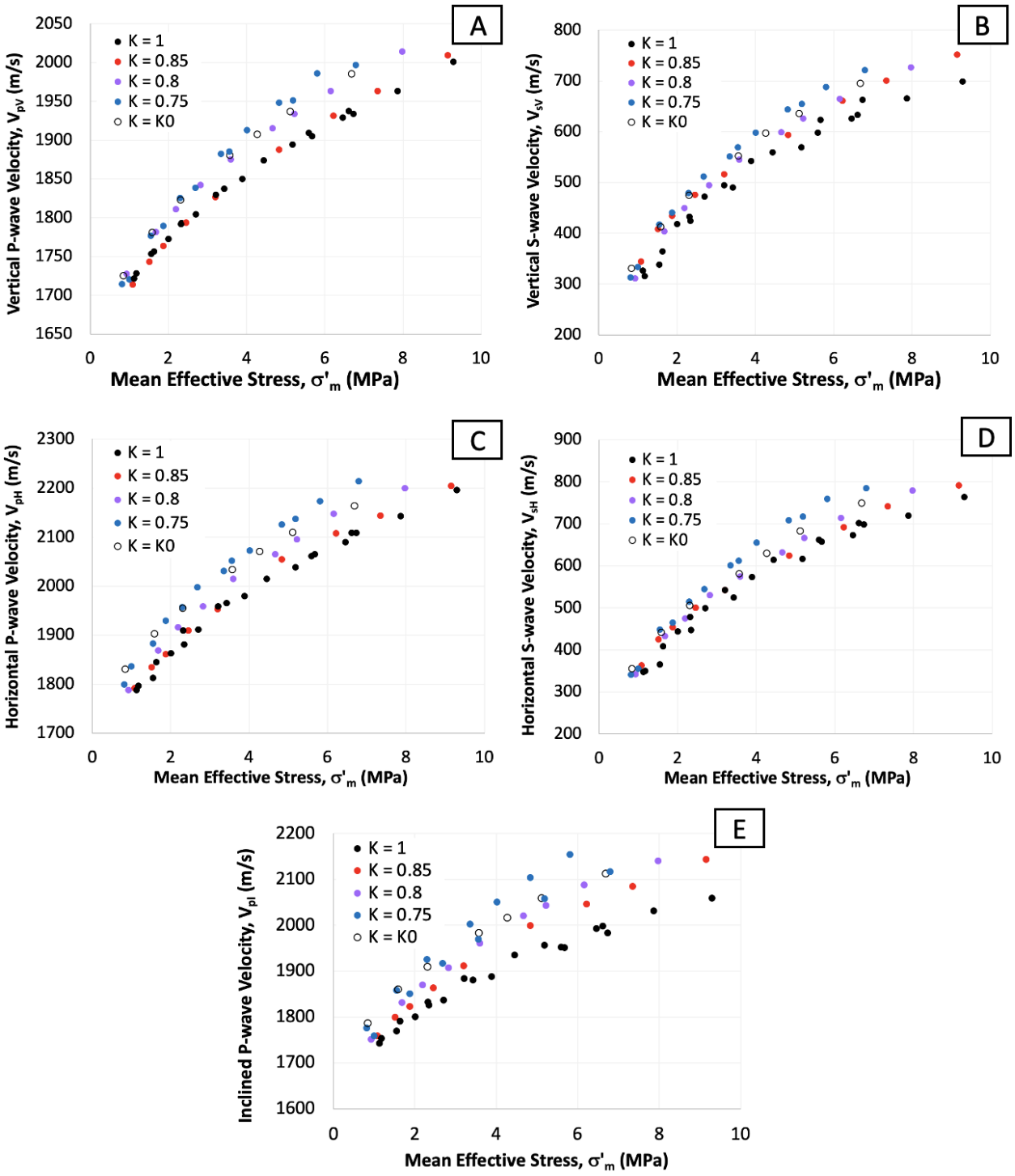

Figure 68. Plots are of all P and S-wave velocities for all tests on RGoM-EI clay. A) is the vertical P-wave velocity, B) vertical S-wave velocity, C) horizontal P-wave velocity, D) horizontal S-wave velocity, and E) is the inclined P-wave velocity. Lower K ratios exhibit higher velocities in general.

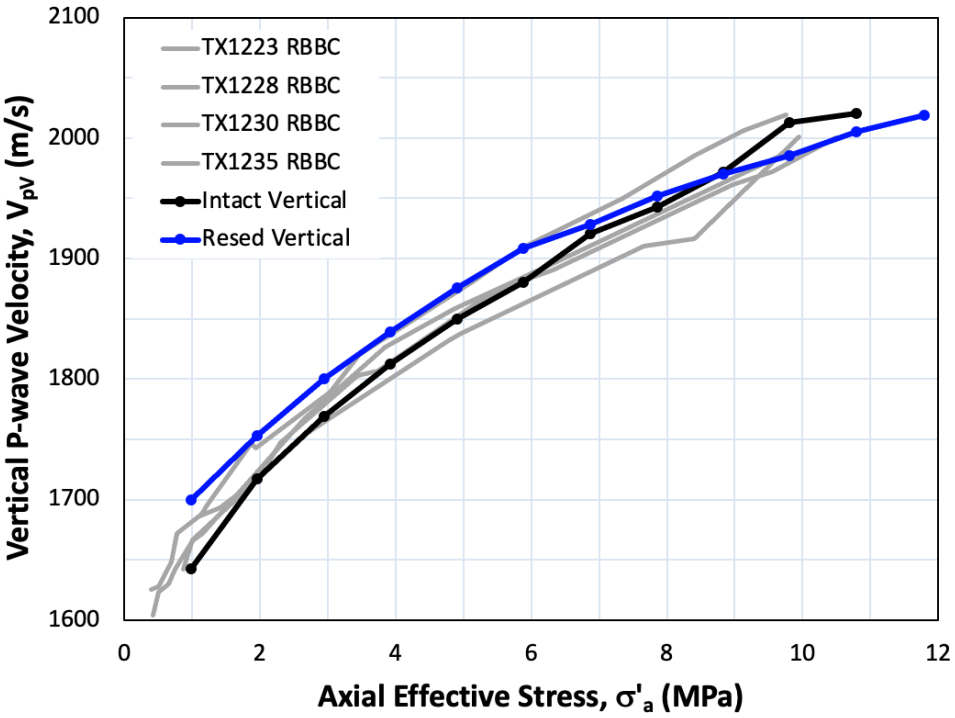

Figure 69. Vertical P-wave velocities from this research (black and blue) compared to those from Marjanovic 2016 (gray). P-wave velocities show good agreement.

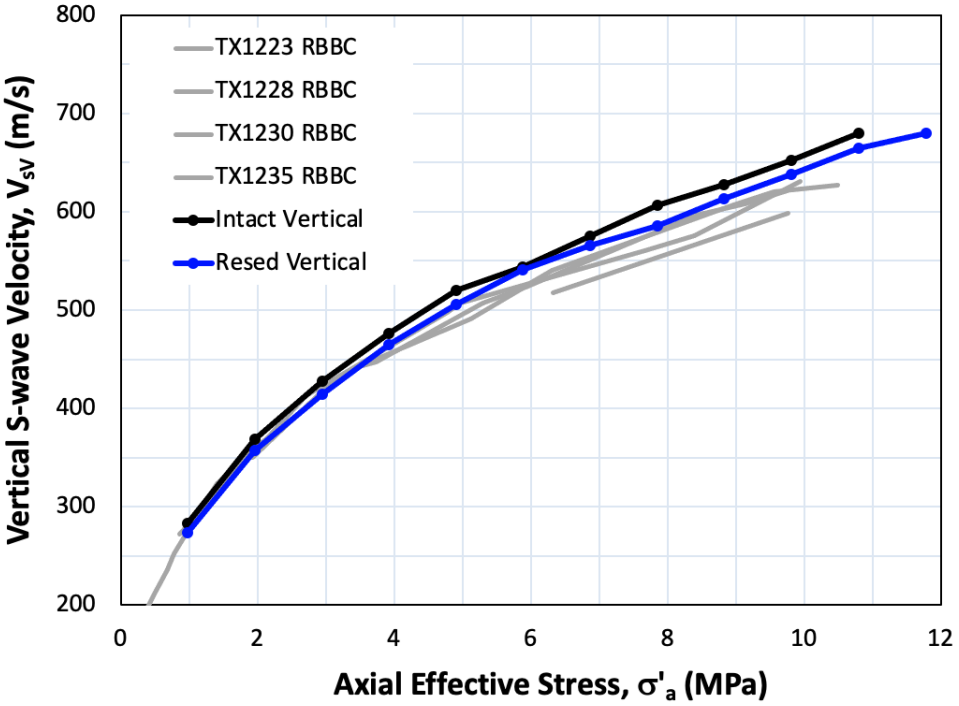

Figure 70. Vertical S-wave velocity comparison between this research (black and blue) and Marjanovic 2016 (gray) shows good agreement.

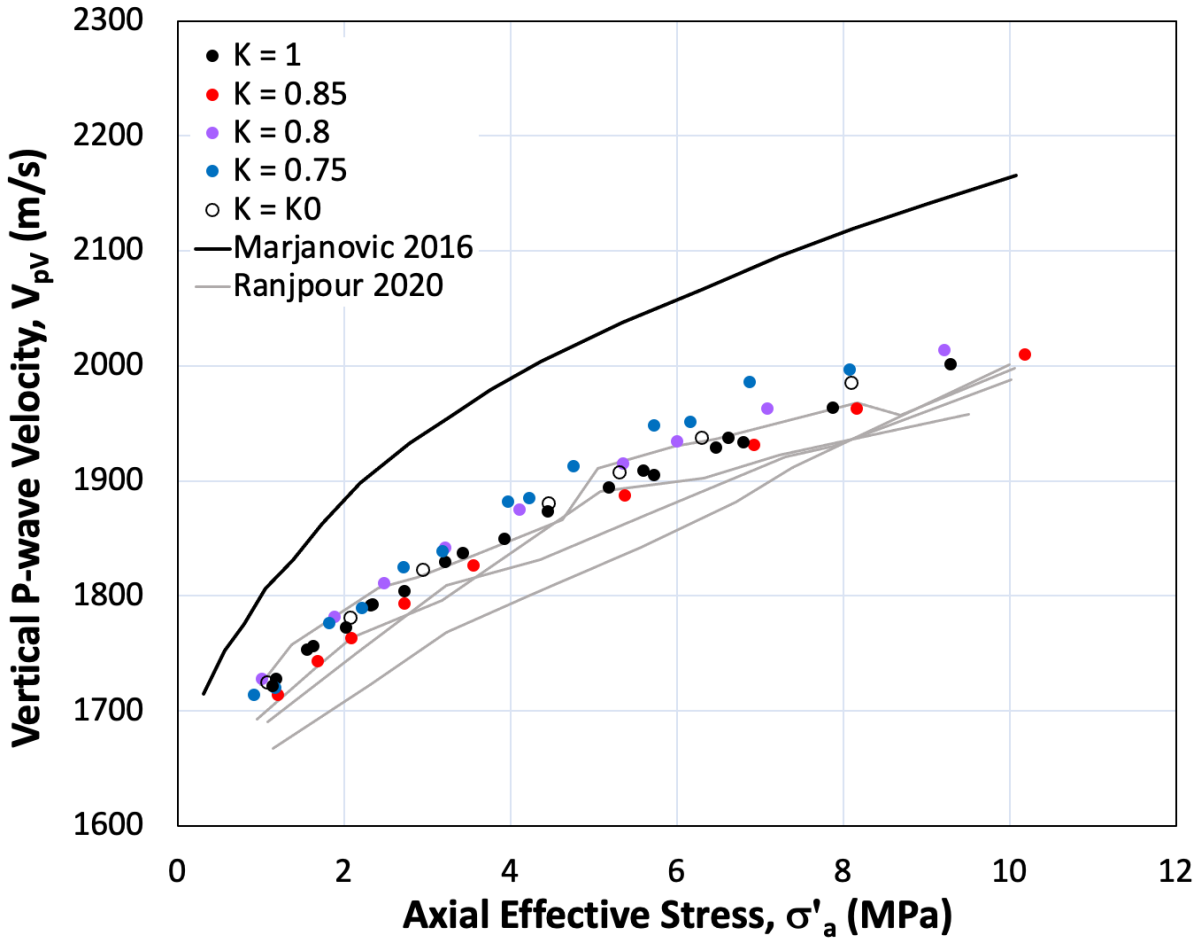

Figure 71. RGoM-EI vertical P-wave velocity vs axial effective stress comparison between Marjanovic (black line), Ranjpour (gray lines) and this research.

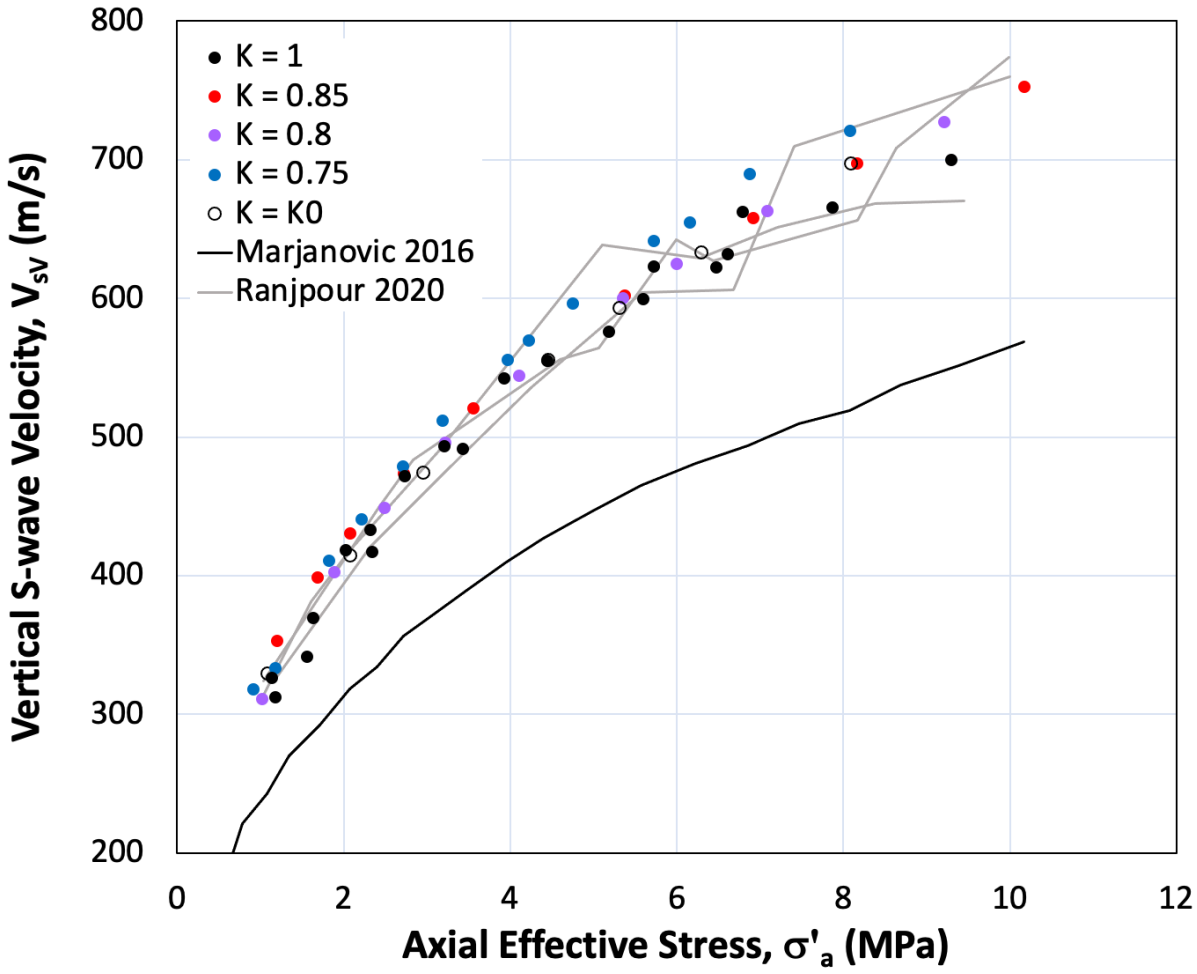

Figure 72. RGoM-EI vertical S-wave velocity vs axial effective stress comparison between Marjanovic (black line), Ranjpour (gray lines) and this research. Results agree well with velocities from Ranjpour.

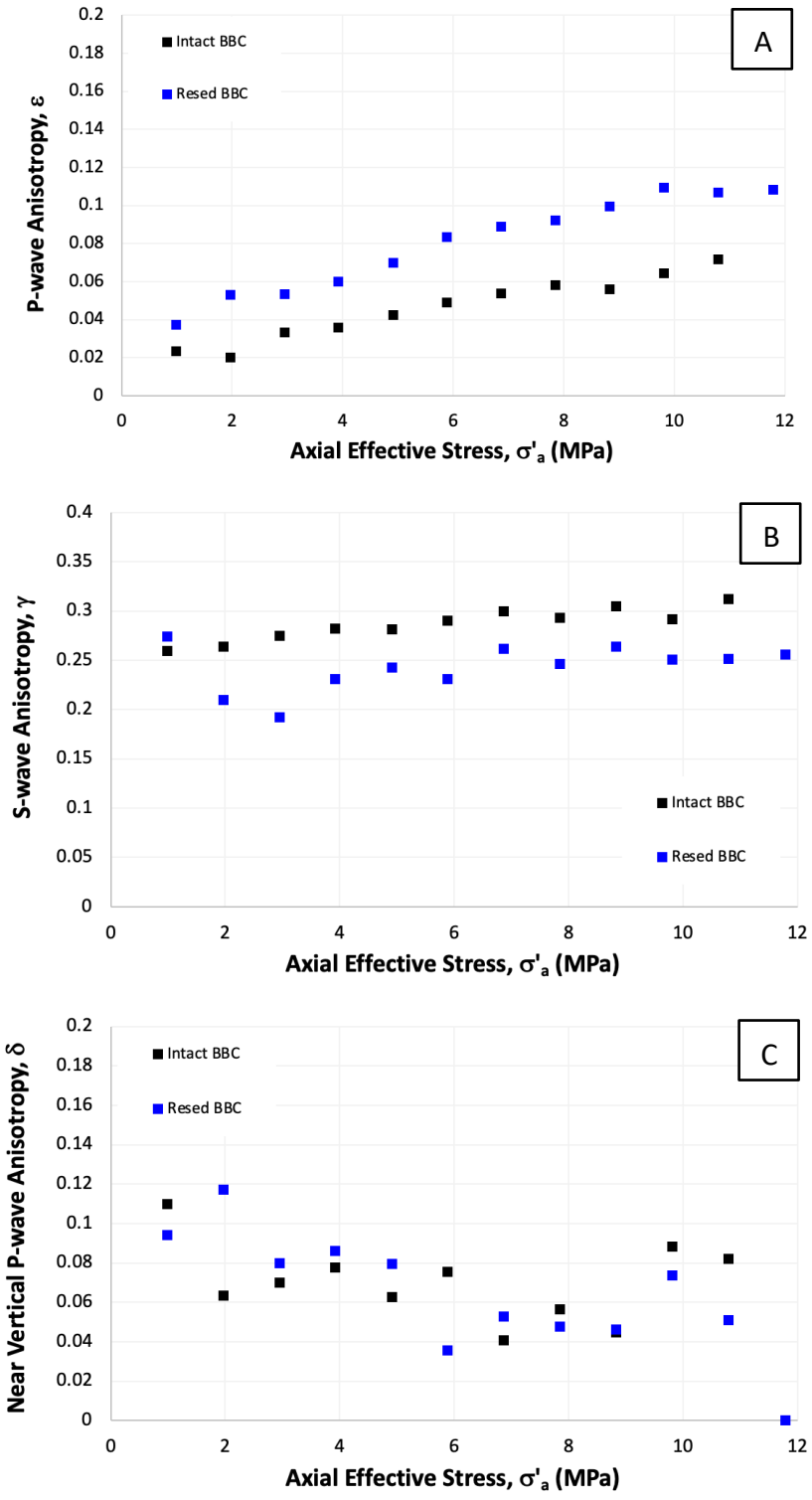

Figure 73. Anisotropy vs axial effective stress for intact BBC (black) vs RBBC (blue). A) is for P-wave anisotropy ε, B) S-wave anisotropy γ, and C) near vertical P-wave anisotropy δ. Anisotropy parameters are derived from the 5 principal velocities, the group angle, and mass densities.

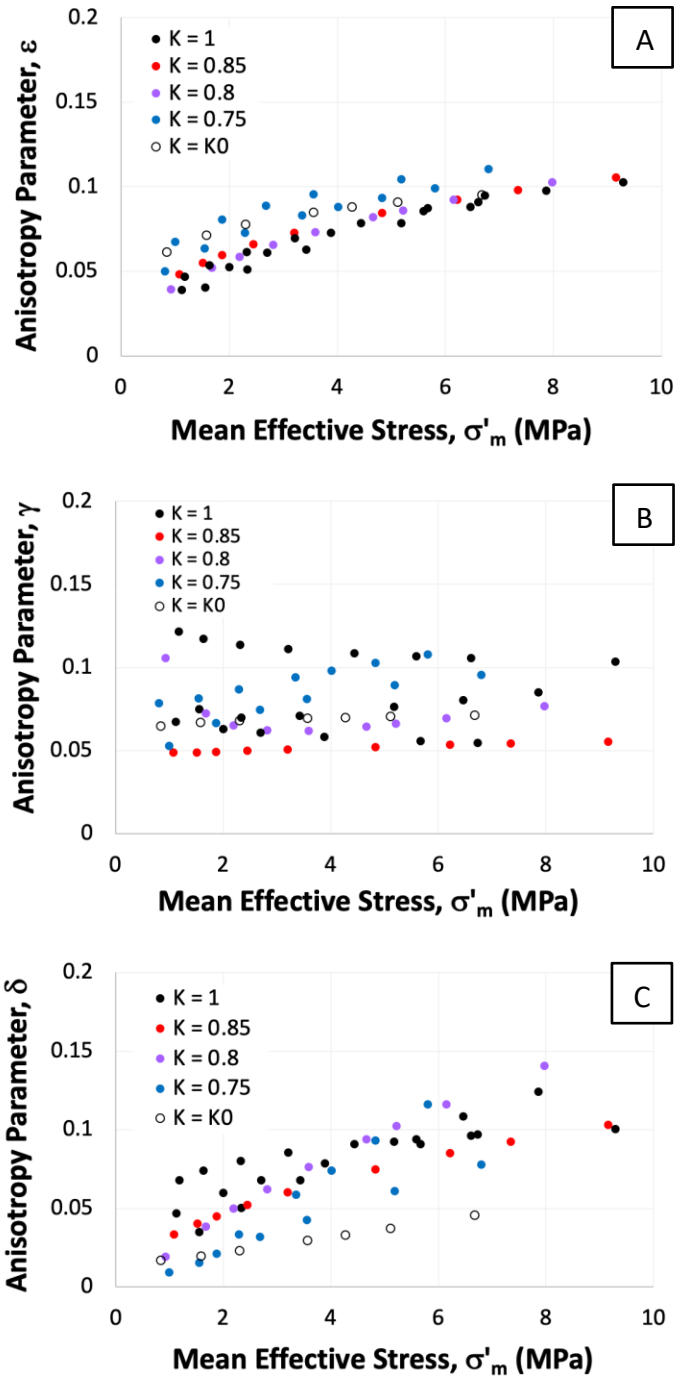

Figure 74. RGoM-EI velocity anisotropy vs mean effective stress. A) is for P-wave anisotropy ε, B) S-wave anisotropy γ, and C) near vertical P-wave anisotropy δ.

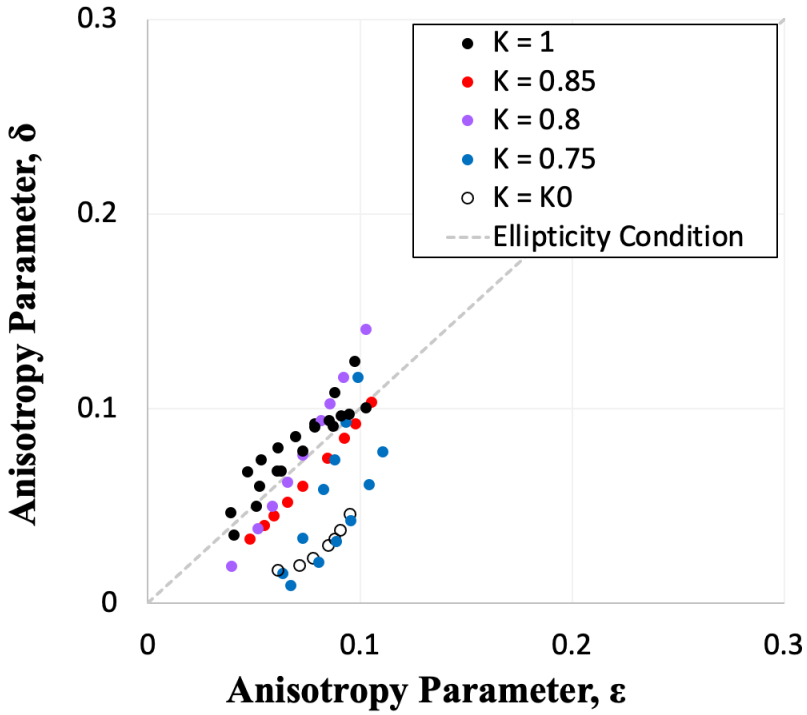

Figure 75. RGoM-EI δ vs ε chart shows that hydrostatic stress path tests appear to have more elliptical wavefront geometry.

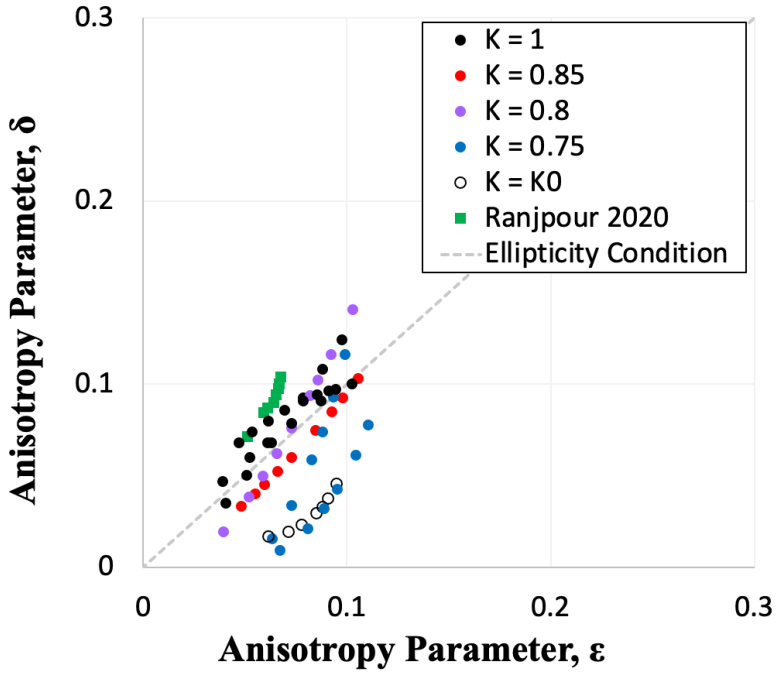

Figure 76. RGoM-EI δ vs ε chart with Ranjpour 2020 data.

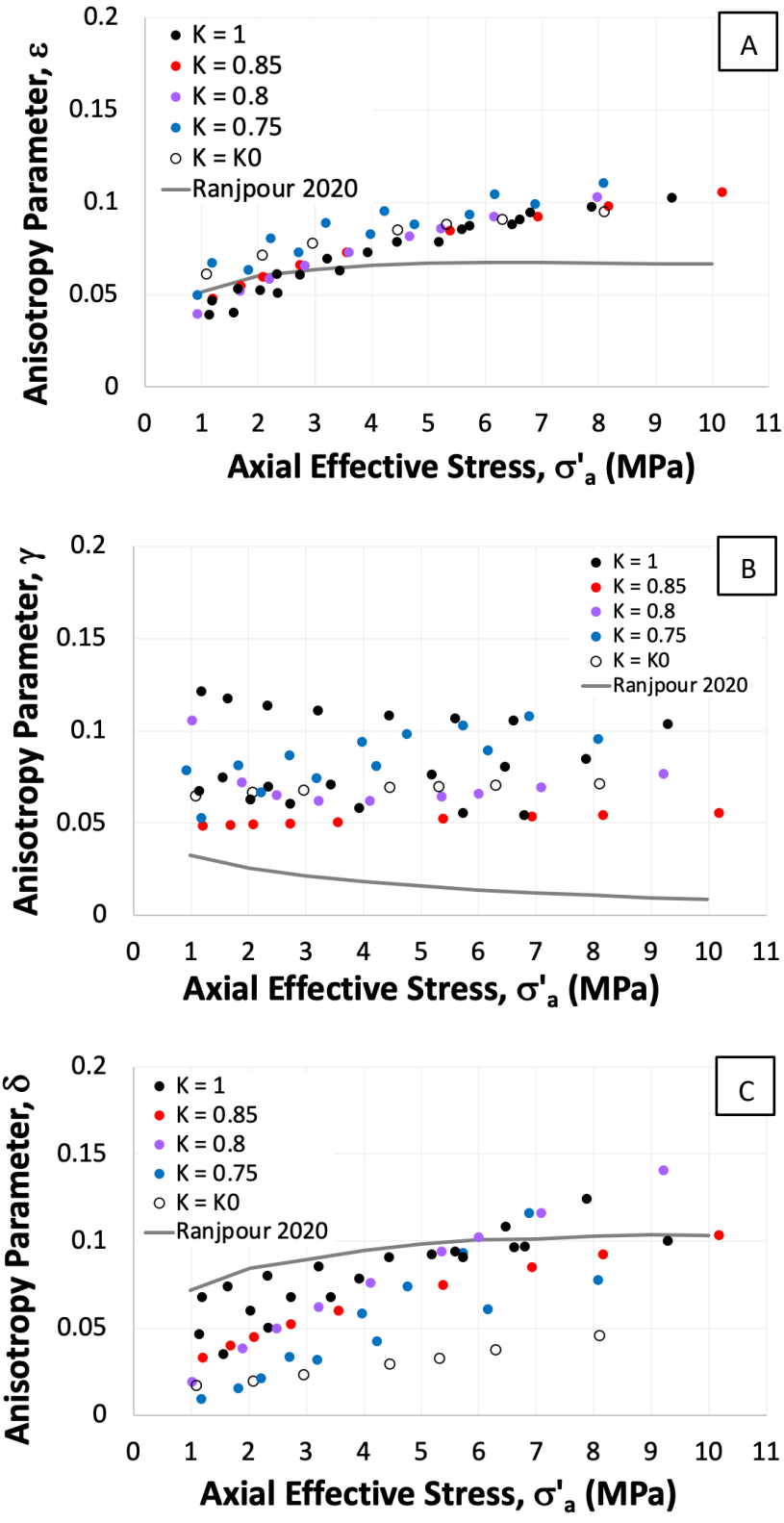

Figure 77. Comparison between Ranjpour 2020 anisotropy in Thomsen parameter – axial effective stress space.

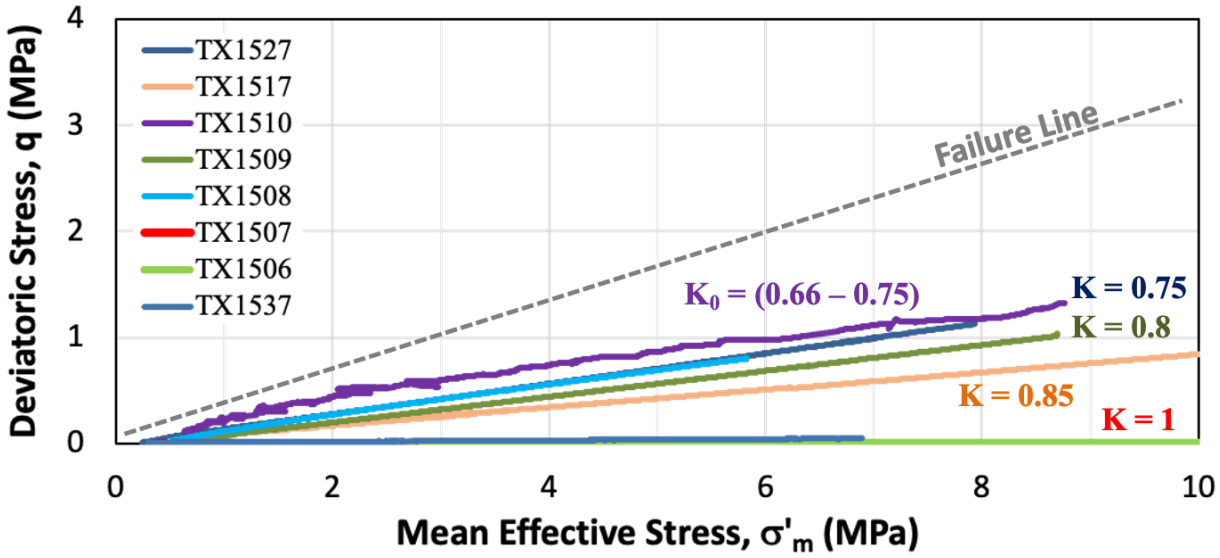

Figure 78. P' – q stress paths of all RGoM-EI drained compression tests. K values are lateral stress ratios. Failure line is idealized, as it is not linear and has a y intercept based on cohesion.

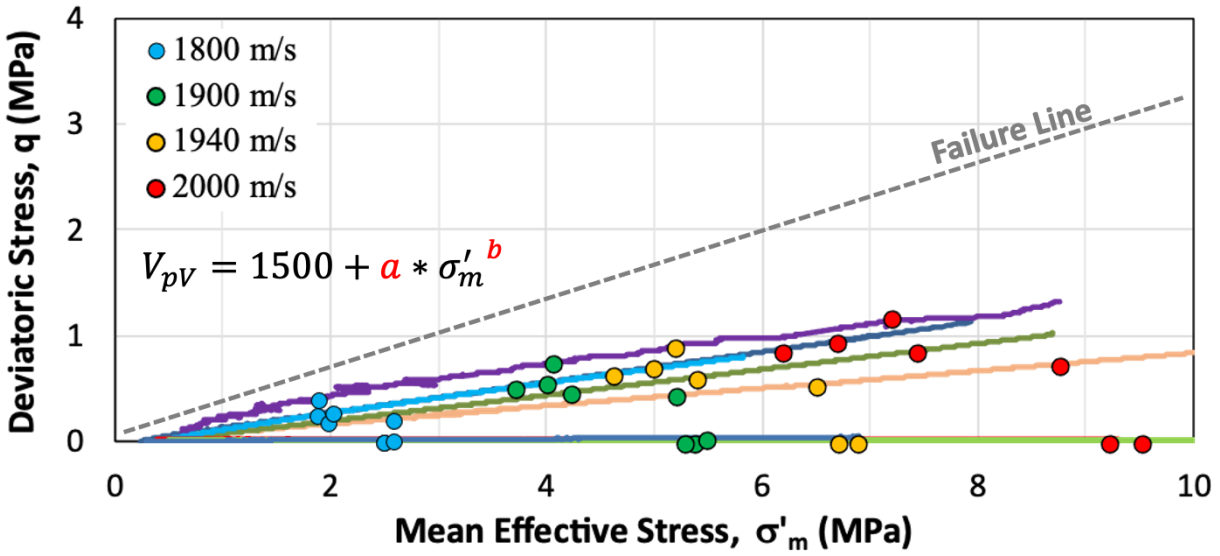

Figure 79. Equivalent velocity points mapped on p' – q stress paths of all RGoM-EI drained compression tests. P-wave velocity was calculated for any data point during the test using the power law above. The p' and q corresponding to that velocity were then plotted.

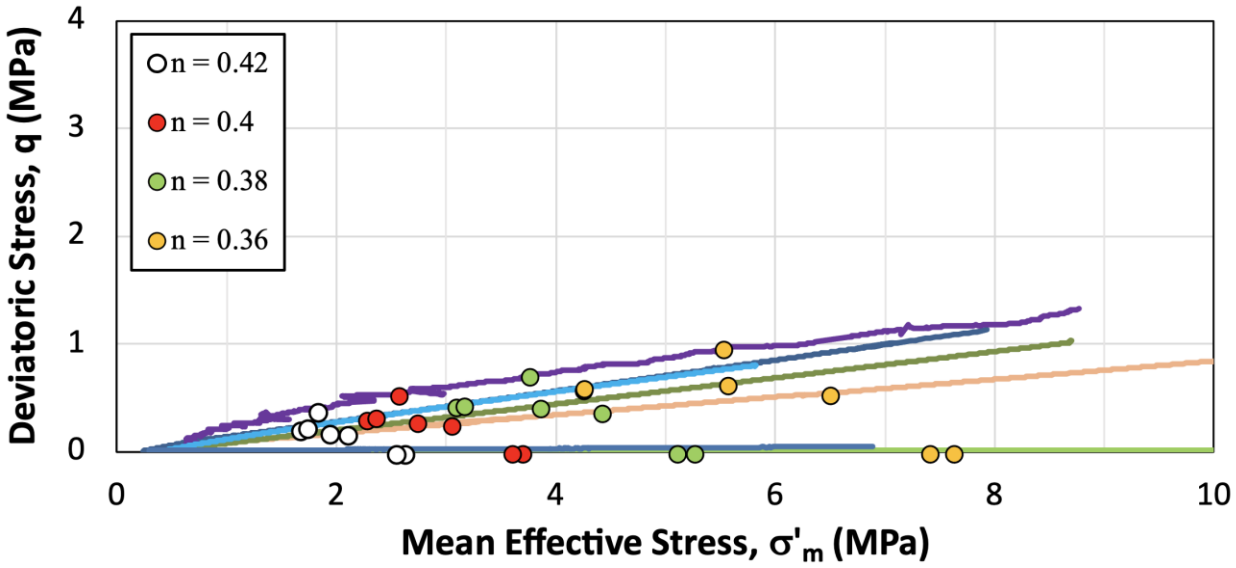

Figure 80. Equivalent porosity mapped on p' – q stress paths for RGoM-EI.

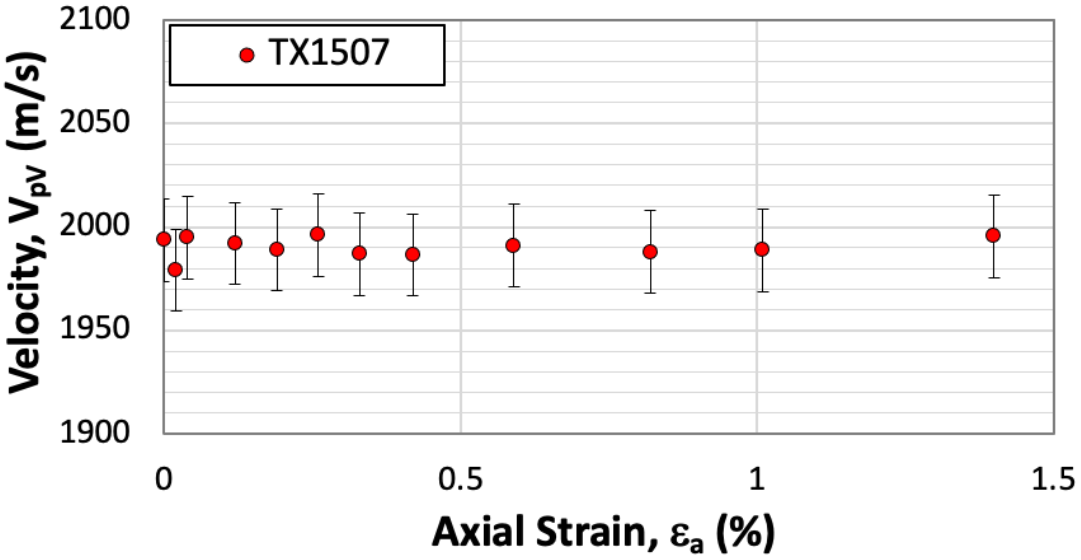

Figure 81. Vertical P-wave velocity during undrained shear for a single RGoM-EI test.

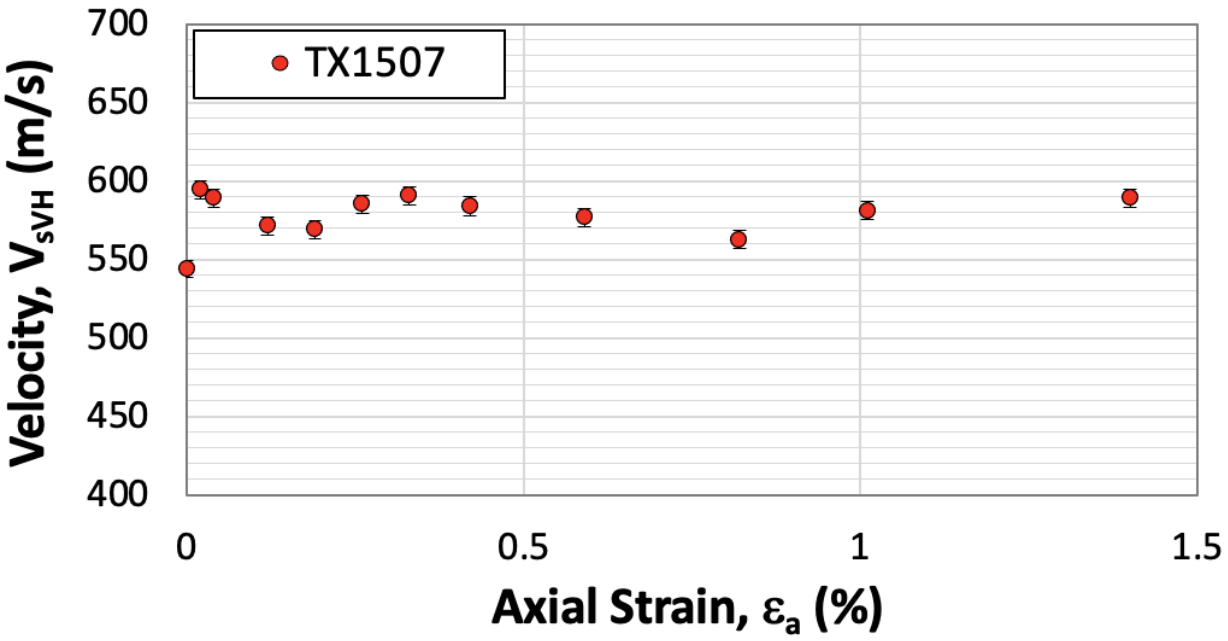

Figure 82. Vertical S-wave velocity during undrained shear

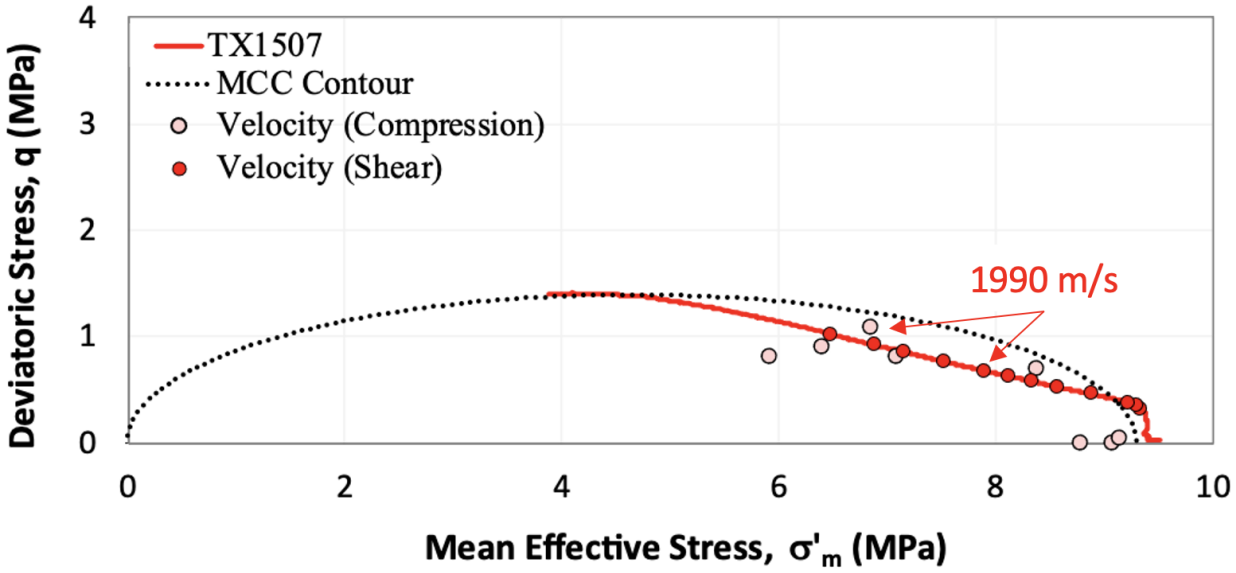

Figure 83. Undrained shear stress path (red line) with velocity measurement points (red circles). Compression-derived iso-velocity points of the same velocity as those measured during undrained shear are in pink. The dotted black line is the MCC ellipse.

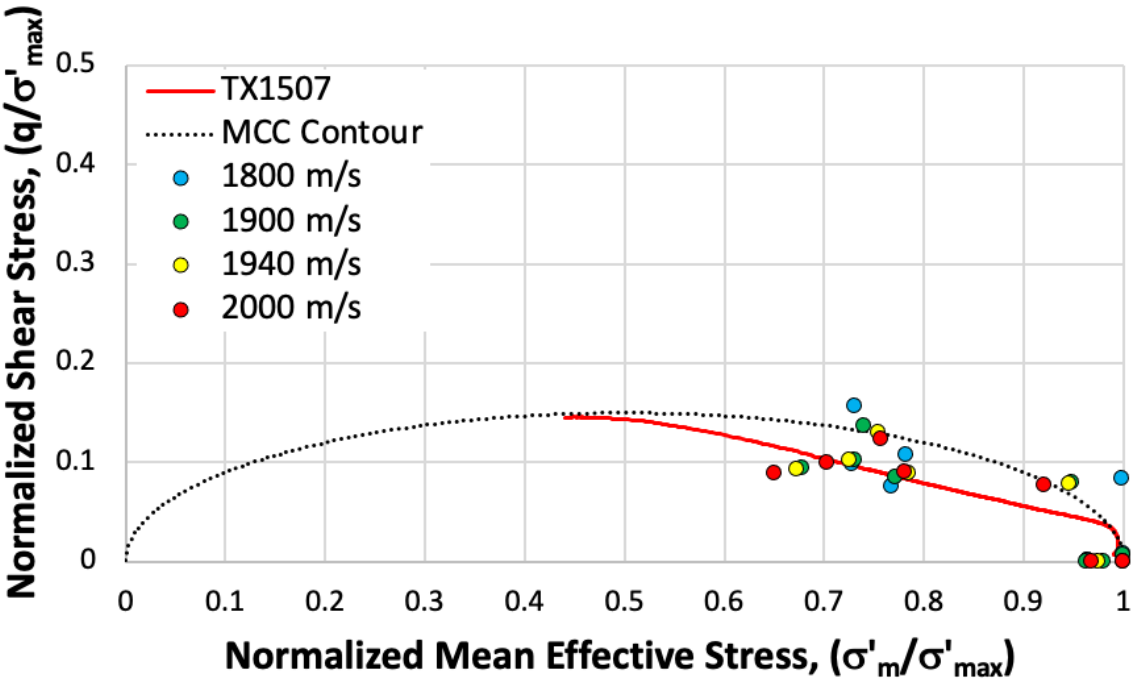

Figure 84. Normalized iso-velocity points and undrained shear stress path with MCC iso-porosity contour.

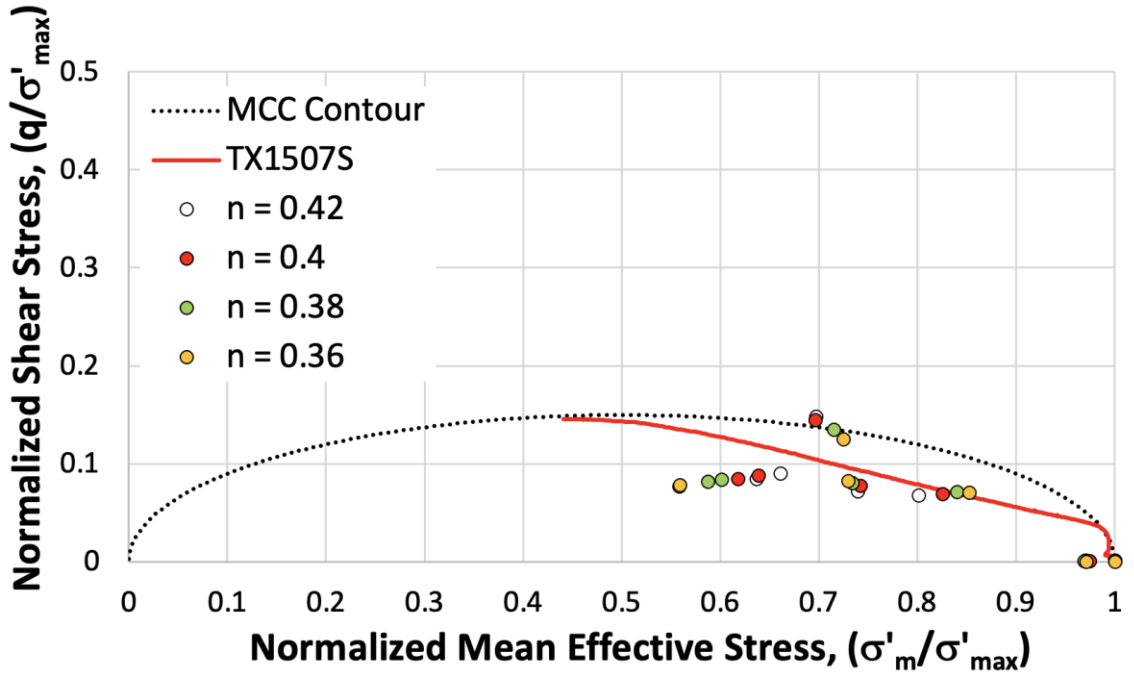

Figure 85. Normalized iso-porosity points and undrained shear stress path with MCC iso-porosity contour.

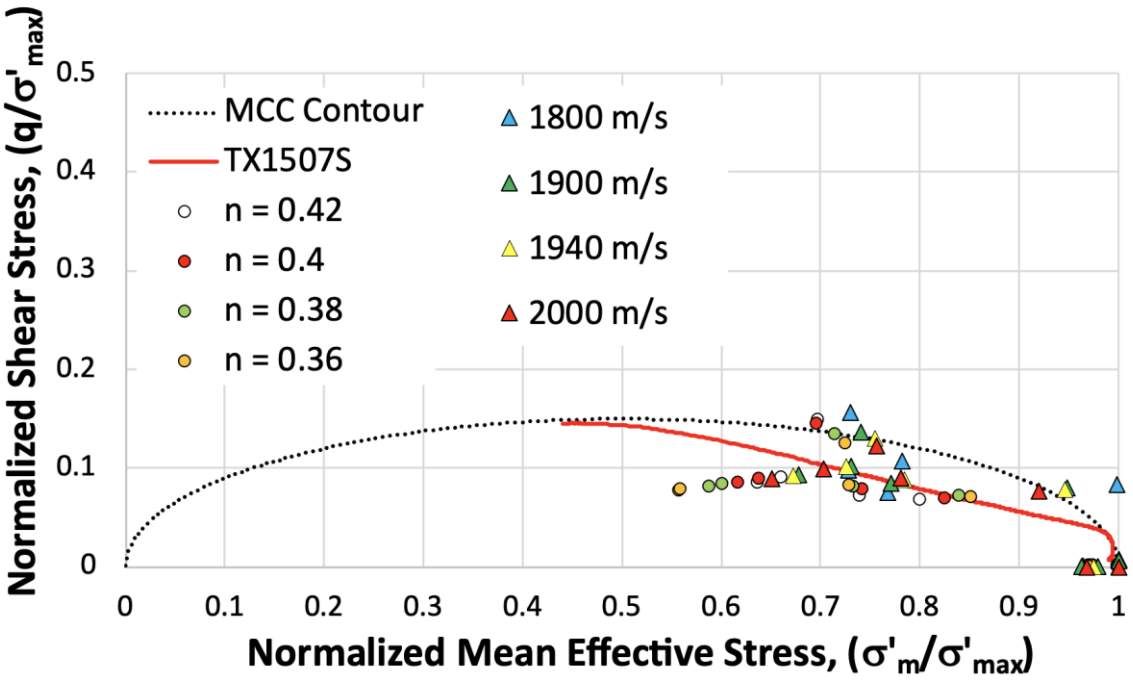

Figure 86. Combined normalized iso-porosity and iso-velocity plot.

7 Conclusions and Recommendations

7.1 Summary of Conducted Work

This research is divided into four parts. These parts are, 1) Explore how velocity anisotropy compares in intact versus resedimented Boston Blue Clay (BBC and RBBC), 2) Measure how velocity anisotropy evolves with different loading stress paths in RGoM-EI, 3) Experimentally investigate the relationship between shear stress, mean effective stress, and axial P-wave velocity during consolidation and undrained shear in RGoM-EI, and 4) Improve the wave pulse driver circuit technology to boost signal amplitude and eliminate sources of noise.

These goals were accomplished using an extensive experimental research program consisting of more than a dozen drained triaxial tests to collect the necessary data. These data were then analyzed and compared to previous in-house data from TAG Labs and MIT researchers. Additionally, the author measured the apparatus deformation response to applied axial load and chamber pressure, as this is a known source of error that hadn't been previously considered. This research measured and corrected the difference upon post-processing, thus improving the accuracy of velocity measurements.

Improvements were also made on the wave sending and receiving circuit itself. First, the receiving wave amplitude was boosted by a factor of 1.4 by giving the actuators enough time during the duty cycle to fully drain. Significant ground bounce noise was eliminated from the horizontal P-wave by isolating the sending and receiving ground pins. Improper actuator insulation, another source of noise and voltage offset, was eliminated as well by coating actuators in a layer of epoxy to keep wires from contacting pore fluid. Routing the wires through the base of the cell rather than through silicone caulking eliminated a persistent internal leak issue as well.

7.2 Summary of Results

The velocity anisotropy of intact versus resedimented BBC between 1 – 10 MPa show little difference overall, with both exhibiting weak anisotropy. The main difference between the two materials was a higher shear wave anisotropy in the intact BBC, thought to be due to the layer and grain orientation induced anisotropy from the natural sedimentation process. Velocity anisotropy tends to increase during stress path consolidation, which means the relative difference between the horizontal and vertical velocities grows as stress increases. This would make sense, as lithified shales exhibit the highest velocity anisotropy, and these specimens are on their way to the stresses required for lithification. The velocities themselves agree with previous work conducted by Marjanovic, 2016, and exhibit an increasing power law relationship between axial effective stress and velocity. The near vertical anisotropy, δ, decreases with axial effective, indicating a possible shift towards a more elliptical wavefront.

Velocity anisotropy along different stress paths from 1 – 10 MPa in RGoM-EI clay shows a similar trend to that of BBC, where anisotropy tends to increase but remains low (Thomsen parameters < 0.15). The stress path has a minor effect on the velocity anisotropy, where stress paths with more shear stress (lower lateral stress) appear to have only 0.02 higher P-wave anisotropy values. The impact of stress path on anisotropy is less clear for γ and δ, possibly due to a lack of measurement precision. The maximum value of the Thomsen parameters is 0.15, indicating weak velocity anisotropy is present, especially at lower stresses. As mean effective stress reaches 10 MPa, anisotropy increases, possibly due to increased particle/void reorientation. The shear wave signal arrivals were clearer for RGoM-EI, thus reducing the uncertainty of velocity results.

Although anisotropy values suffered from arrival signal interpretation issues, the axial P-wave arrivals were always clear. This gives more confidence in the results of

the third goal, which was to see how axial P-waves and porosity are affected by various degrees of shear stress during drained compression and undrained shearing. Results show that the axial P-wave velocity greatly increases for the same mean effective stress when shear stress is also present. The inverse is true for void ratio/porosity, where porosity decreases when shear stress is present for a given mean effective stress. These results imply that vertical and mean effective stress-based pressure prediction models are not sufficient to predict pressure in sedimentary basins, as porosity is a first order control of the compressional velocity behavior for normally consolidated clays.

This research also supports the use of the full effective stress tensor method proposed by Heidari et al., 2018, which relies on MCC to model iso-velocity/porosity curves. This method assumes elliptical iso-porosity/velocity surfaces, which had not been experimentally confirmed until this research. Velocities derived from the mean effective stress – velocity power relationship allowed for velocity to be calculated at every acquired data point, thus enabling any given velocity to be examined across all tests. In this manner, equivalent velocities and porosities across tests were derived and plotted in MIT σ'_m – q space. These equivalent velocities/porosities formed elliptical patterns from the different stress path tests, supporting the MCC iso-porosity theory. The P-wave velocities measured during undrained shear remained constant, and the undrained shear stress path agrees with iso-velocity curves from drained compression.

7.3 Future Work

Future work should focus on improving the signal amplitude of the received S-waves by expanding the voltage range of the driver circuit and selecting a specimen geometry that minimizes measurement errors. A shorter specimen would allow for a higher amplitude vertical shear wave signal to be received due to less attenuation during travel. Changing the geometry of the specimen to a cube would allow for more

accurate velocity measurements as well, as increased horizontal wave travel distance would reduce the effects of measurement errors. The inclined velocities would also benefit from a cubic geometry, as it is currently difficult to orient the actuators in perfect opposition. Specimens with a cubic geometry would allow for more accurate inclined distances, increased signal amplitude, and better constraints on cross-sectional area. The addition of resistivity measurements should be considered as well, as it is not known how resistivity evolves along with velocity and stress path in clays.

Another way to improve velocity accuracy would be to add a lateral strain measurement device. This could be used to measure the actual deformation undergone by the specimen during stress path consolidation, rather than relying on indirect measurement through volumetric strain. On tests with higher shear stress the specimen can bulge at the center, as the radial strain is not distributed evenly along the length of the specimen. The addition of the lateral strain measurements would allow for anisotropy measurements to be made during undrained shear, as well as confirming that specimens undergo true uniaxial compression.

Ultimately, more duplicate tests need to be performed to assess the reproducibility and reduce the uncertainty associated with each test.

8 References

1. Atkinson, J., *Non-linear soil stiffness in routine design.* Géotechnique, 2000. **50**(5): p. 487-508.
2. Karcher, J.C., *The reflection seismograph: Its invention and use in the discovery of oil and gas fields.* The Leading Edge, 1987. **6**(11): p. 10-19.
3. Zemanek, J., et al. *Continuous Acoustic Shear Wave Logging*. in *SPWLA 25th Annual Logging Symposium*. 1984.
4. Thomsen, L., *Weak elastic anisotropy.* Geophysics, 1986. **51**(10): p. 1954-1966.
5. Thomsen, L., *Understanding seismic anisotropy in exploration and exploitation*. 2014: Society of Exploration Geophysicists.
6. Fessenden, R.A., *Method and apparatus for locating ore-bodies*. 1917, Google Patents.
7. Iida, K., *Velocity of elastic waves in a granular substance.* Bull. Earth. Res. Int, 1939. **17**: p. 783-808.
8. Paterson, N.R., *Seismic wave propagation in porous granular media.* Geophysics, 1956. **21**(3): p. 691-714.
9. Lawrence Jr, F.V., *Ultrasonic shear wave velocities in sand and clay*. 1965, MASSACHUSETTS INST OF TECH CAMBRIDGE DEPT OF CIVIL ENGINEERING.
10. Kuwano, R. *The measurement of G., in a resonant column, bender element, torsional shear apparatus*. in *Pre-failure Deformation Characteristics of Geomaterials: Proceedings of the Second International Symposium on Pre-Failure Deformation Characteristics of Geomaterials: Torino 99: Torino, Italy 28-30 September, 1999*. 1999. CRC Press.
11. Ku, T. and P.W. Mayne, *Yield stress history evaluated from paired in-situ shear moduli of different modes.* Engineering geology, 2013. **152**(1): p. 122-132.
12. Johnson, S.S.M., *Modeling a bender element test using Abaqus Finite Element Program*. 2011, Massachusetts Institute of Technology.

13. Marjanovic, J., *The study of shear and longitudinal velocity measurements of sands and cohesive soils*. 2012, Massachusetts Institute of Technology.
14. Germaine, J.T. and C.C. Ladd, *Triaxial testing of saturated cohesive soils.* Advanced triaxial testing of soil and rock, ASTM STP, 1988. **977**: p. 421-459.
15. Wiggs, D.M., *A generalized model to estimate the elastic stiffness tensor of mudrocks based on the full strain tensor*. 2021.
16. McCollum, B. and F. Snell, *Asymmetry of sound velocity in stratified formations.* Physics, 1932. **2**(3): p. 174-185.
17. Postma, G., *Wave propagation in a stratified medium.* Geophysics, 1955. **20**(4): p. 780-806.
18. Laughton, A.S., *Sound propagation in compacted ocean sediments.* Geophysics, 1957. **22**(2): p. 233-260.
19. Ranjpour, D., *Stiffness and Anisotropy Characterization of Mechanically-Compressed Cohesive Soils Using Directional Wave Propagation*. 2020, Tufts University.
20. Byun, B.S., *Seismic parameters for transversely isotropic media.* Geophysics, 1984. **49**(11): p. 1908-1914.
21. Soil, A.C.D.-o. and Rock, *Standard Practice for Classification of Soils for Engineering Purposes (Unified Soil Classification System) 1*. 2017: ASTM international.
22. Lade, P. and R. De Boer, *The concept of effective stress for soil, concrete and rock.* Geotechnique, 1997. **47**(1): p. 61-78.
23. Casey, B.B.A., *The consolidation and strength behavior of mechanically compressed fine-grained sediments*. 2014, Massachusetts Institute of Technology.
24. Abdulhadi, N.O., *An experimental investigation into the stress-dependent mechanical behavior of cohesive soil with application to wellbore instability*. 2009, Massachusetts Institute of Technology.
25. Bishop, A.W., *Test requirements for measuring the coefficient of earth pressure at rest*. 1958: British Library Lending Division [supplier].

26. Nikolinakou, M.A., et al., *Initiation and growth of salt diapirs in tectonically stable settings: Upbuilding and megaflaps.* AAPG Bulletin, 2017. **101**(6): p. 887-905.
27. Ladd, C., *Stress-strain behavior of saturated clay and basic strength principles: Research in Earth*. 1964, Physics-Research Report R64-17, Massachusetts Institute of Technology.
28. Heidari, M., M.A. Nikolinakou, and P.B. Flemings, *Coupling geomechanical modeling with seismic pressure prediction.* Geophysics, 2018. **83**(5): p. B253-B267.
29. Nikolinakou, M., M. Heidari, and P. Flemings. *Pore-pressure prediction based on seismic velocities coupled with geomechanical modeling*. in *50th US Rock Mechanics/Geomechanics Symposium*. 2016. OnePetro.
30. Hauser, M.R., B.A. Couzens-Schultz, and A.W. Chan, *Estimating the influence of stress state on compaction behavior.* Geophysics, 2014. **79**(6): p. D389-D398.
31. DeGroot, D.J., M.E. Landon, and S.E. Poirier, *Geology and engineering properties of sensitive Boston Blue Clay at Newbury, Massachusetts.* AIMS Geosciences, 2019. **5**(3): p. 412-447.
32. Johnson, E.G., *Geotechnical characteristics of the Boston area.* Civ. Eng. Pract, 1989. **4**(1): p. 53-64.
33. Testing, A.S.f. and Materials. *Standard Test Methods for Liquid Limit, Plastic Limit, and Plasticity Index of Soils, ASTM D4318-17e1*. 2017. American Society for Testing and Materials United States of America.
34. Adams, A., *Permeability Anisotropy and Resistivity Anisotropy of Mudrocks*. 2014, Ph. D Thesis: Massachusetts Institute of Technology, Cambridge, MA.
35. Germaine, J.T. and A.V. Germaine, *Geotechnical laboratory measurements for engineers*. 2009: John Wiley & Sons.
36. Finnegan, J.M., *Comparison of Resedimented with Intact Mudrock Behavior*. 2020, Tufts University.
37. Bailey, W.A., *The effects of salt on the shear strength of Boston blue clay*. 1961, Massachusetts Institute of Technology.

38. Marjanovic, J., *Stiffness characterization of mechanically-compressed cohesive soils using wave propagation*. 2016, Massachusetts Institute of Technology.
39. Kabbani, A. and A.J. Al-Khalili, *Estimation of ground bounce effects on CMOS circuits.* IEEE Transactions on components and Packaging Technologies, 1999. **22**(2): p. 316-325.
40. Andersen, G.R., *Physical mechanisms controlling the strength and deformation behavior of frozen sand*. 1991, Massachusetts Institute of Technology.
41. Leroueil, S., et al., *Influence of filter paper and leakage on triaxial testing.* Advanced triaxial testing of soil and rock, ASTM STP, 1988. **977**: p. 189-215.
42. Sheahan, T.C., *An experimental study of the time-dependent undrained shear behavior of resedimented clay using automated stress path triaxial equipment*. 1991, Massachusetts Institute of Technology.
43. Khan, Q., S.-W. Moon, and T. Ku, *Idealized sine wave approach to determine arrival times of shear wave signals using bender elements.* Geotechnical Testing Journal, 2019. **43**(1): p. 171-193.
44. Airey, D. and A. Mohsin, *Evaluation of shear wave velocity from bender elements using cross-correlation.* Geotechnical Testing Journal, 2013. **36**(4): p. 506-514.
45. Horan, A.J., *The mechanical behavior of normally consolidated soils as a function of pore fluid salinity*. 2012, Massachusetts Institute of Technology.
46. Nordquist, T.J., *Permeability anisotropy of resedimented mudrocks*. 2015, Massachusetts Institute of Technology.
47. Parry, A.R., *The Effect of Temperature and Variation of Salinity during One Dimensional Compression*. 2018, PhD thesis, Tufts University.